

Molecular Dynamics Study of Polymorphs of Silica with First-Principles Interatomic Potentials

(第一原理的原子間力を用いた分子動力学法によるシリカ多形の研究)

by

Shinji Tsuneyuki

常 行 真 司



0065089237

9551

**Molecular Dynamics Study of Polymorphs of Silica
with First-Principles Interatomic Potentials**

**A Dissertation
Presented to
the Department of Physics
the Faculty of Science
the University of Tokyo**

**In Partial Fulfillment
of the Requirements for the Degree
Ph.D. in Physics**

by

Shinji Tsuneyuki

September 1989

Acknowledgments

The author is indebted to Professor Hideo Aoki for continual guidance, encouragement and supervising the present thesis patiently. He wishes to express his sincere gratitude to Professor Masaru Tsukada for helpful discussions and for guidance since his postgraduate school days. He is grateful to Professor Yoshito Matsui for illuminative discussions, suggestions, collaboration and encouragement throughout the course of the present study, and to Mrs Y. Matsui for her hospitality during his stays at the Institute for Study of the Earth's Interior at Misasa. He also wishes to thank Dr. S. Nosé and Dr. K. Kawamura for helpful discussions and providing the original MD programs, Dr. N. Kosugi for the Hartree-Fock self-consistent-field program package *GSCF3*, Professor M. Matsui, who helped him use the static-energy-minimization program *WMIN* and modify MD programs, and Professor T. Yagi and Mr. Y. Tsuchida for communicating their experimental results prior to publication.

The author is pleased to acknowledge fruitful discussions with Professor H. Kamimura, Dr. O. Sugino, Dr. N. Shima, Dr. R. Saito, and all the members of the research group under Professor H. Kamimura, Professor M. Tsukada and Professor H. Aoki. His thanks are extended to Professor D. Weaire, Professor T. Fujii, Dr. J. Habasaki, Dr. A. Oshiyama and Mr. Y. Miyamoto for stimulative discussions. He is also indebted to Dr. J. Maddox, who first introduced his work in public except for his own papers. Mr. H. Yashikida and the members of his group in Toshiba, who helped him produce computer-graphic animation films of the molecular dynamics simulations, are also acknowledged.

The numerical calculations were done on HITAC M682H and S820/80 computers at the Computer Centre, the University of Tokyo, and TOSBAC DS600/80 computer at the Institute for Study of the Earth's Interior, Okayama University.

Last but not least, the author wishes to thank his parents and old friends for many years of encouragements.

Biographical Note

The author was born in Matsuyama on the 16th of May, 1961. He graduated from the University of Tokyo in 1984 and received his M.Sc. degree in physics from the University of Tokyo in 1986. Among his publications related with the present thesis are

"First-principles interatomic potential of silica applied to molecular dynamics",
Phys. Rev. Lett. **61**, 869-872(1988).

"New pressure-induced structural transformations in silica obtained by computer simulation", *Nature* **339**, 209-211(1989).

"Molecular dynamics simulation of silica with a first-principles interatomic potential", in *Dynamical Processes of Material Transport and Transformation in the Earth's Interior*" (F. Marumo ed.) (Terra Scientific Publishing Co., Tokyo), in press.

Contents

I. Introduction	
1.1. Motivation	1
1.2. Historical survey of the simulation of silica and silicate	9
1.3. Polymorphs of silica	14
1.4. Organization of the present thesis	17
II. Interatomic Potentials of Silica	
2.1. Method of the cluster calculation	19
2.2. Potential energy surfaces and pairwise interatomic potentials	23
2.3. Effect of the environment potential	26
2.4. Larger clusters	30
2.5. Summary and discussion	35
III. Molecular Dynamics Simulation	
– Normal and High Pressure Condition	
3.1. Introduction: Molecular dynamics simulation	37
3.2. Simulated polymorphs of silica	42
3.3. Summary and discussion	52
IV. The α - β Structural Phase Transition of Quartz	
4.1. Introduction	54
4.2. Molecular dynamics simulation of heating of quartz	55
4.3. Summary and discussion	68

V. Pressure-Induced Structural Transformations	
5.1. Introduction	71
5.2. Interatomic potentials	72
5.3. Molecular dynamics simulation of high-pressure compression	75
5.4. Summary and discussion	85
VI. Application to Magnesium Silicates	87
VII. Concluding Remarks	
7.1. A conjecture respecting the anomalous diffusion property of silicate melt	96
7.2. Summary	100
Appendix	
A. Crystal data of polymorphs of silica	103
B. Pressure-induced structural transformations	108
C. Crystal data of polymorphs of magnesium silicate	114
References	116

Chapter I. Introduction

Section 1.1. Motivation

Solid state physics has a wide spectrum both in the systems considered and in methods employed. Versatile phenomena and models to explore fundamental physics have stimulated each other: discovery of physical phenomena often brings forth new methodology to tackle the new problem, and vice versa in many cases. Development of computational physics in recent years, which is complementary to both experimental and theoretical physics, is thus adding new pages to the long history of science.

The computational physics arises from the need to study the problems which are analytically impossible to solve without unfounded and empirical approximations. Instead of employing such approximations, we directly simulate physical (often many-body) systems with use of large computers. The method and difficulty in the practical computational process depends on whether the system is classical or quantum-mechanical, or whether the model is quantitatively realistic or simplified for qualitative discussion.

The computational physics is in some cases said to achieve more reliable results than experiments by the following reason. All the experimental techniques inherently have various uncertainty that we cannot control. Even though the physical phenomena may be reproducible under certain conditions in experiments, the interpretation of the experimental results can be ambiguous, partly because the experimental condition itself may sometimes deviate from, or contain something else from, what we have intended to impose. Moreover we cannot obtain all the physical properties we want from experiments especially under extreme conditions beyond present experimental techniques. Then we often turn to the natural phenomena themselves, e.g., cosmic rays, rocks, planets and the universe, or else we can perform computer simulations nowadays.

For meaningful computer simulations, first-principles approaches are especially desirable. Non-empirical approaches using computer simulations not

only provide sound basis for our conjecture but can also lead to conclusions beyond our intuition. Thus the computational physics can provide guiding principles complementing the theoretical and experimental physics.

Design and prediction of properties of materials is one of the most challenging problems in the computational physics. Given the crystal structure, recent developments in many-body calculations for condensed-matter physics give promise to the reliable description of electronic states of materials. The formalisms for calculation includes: the Hartree-Fock self-consistent-field (HF-SCF) method, in which the many-body problem of electrons in atoms and molecules is reduced to the one-body problem by the Hartree-Fock mean field approximation; the configuration interaction (CI) method to treat the electron correlation; the local-density-functional (LDF) method for systems including crystals, and the variational or diffusion Monte Carlo method developed very recently to take account of the electron correlation in more rigor. However, we can carry out these electronic-structure calculations only when we know the atomic configuration of materials.

Although the electronic structure and the atomic configuration is mutually related and have to be elucidated for complete understanding and prediction of the physical properties of materials, the atomic configuration has obviously the top priority since we have to start from the structure. In fact, a number of interesting phenomena in the field of solid state physics arise from peculiar and characteristic structures of materials. This is why so-called "material design" is becoming a subject of intense study in both solid state physics and industrial research in these days. The computational physic is thus expected to play an essential role in the research of material structures.

The first attempt to understand crystalline structures microscopically was made by Victor Moritz Goldschmidt and a little later by Linus Pauling before 1930's. They introduced a notion of the ionic radius (or crystal radius), which is

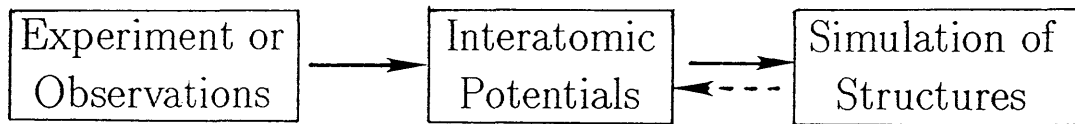
nowadays still very useful for understanding and roughly predicts the structure of ionic crystals. It is obvious, however, that only one parameter per one atom is insufficient to describe a variety of materials and their properties such as the elastic properties. Interatomic potentials were introduced from this viewpoint.

The idea that the structure of materials is determined by the interatomic potentials is still a highly simplified picture if compared with the full problem of solving the Schroedinger equations containing both nuclei and electrons. However, the interatomic potential is definitely an important starting point of microscopic treatment of material structures.

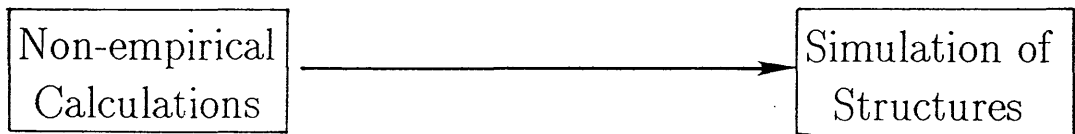
There are some levels of simplification for the interatomic potentials. The most simplified version is so-called pairwise potentials (or pair potentials), which are made to depend only on the interatomic distance between two atoms. Many simple ionic crystals are known to be simulated rather well with the pair potentials (Tosi, 1964). The parameters contained in the potential functions are usually determined empirically so that experimental results are reproduced (Fig.1-1(a)). An obvious extension is to employ three-body potentials which depend on the bond angles among three atoms. This type of interaction is needed to simulate covalent materials such as pure silicon (Stillinger and Weber, 1985; Biswas and Hamann, 1987). If we further want to reproduce the phonon dispersion very precisely, the shell-model potentials are known to be necessary, which take account of the distortion of electron distribution by floating ionic shells (Catlow, Dixon and Mackrodt, 1982). In this way, as the level of sophistication increases, the degree of freedom (the number of potential parameters) to specify the interatomic potentials is doomed to increase, so that we cannot expect from the interatomic potentials much ability to predict unknown properties of materials as far as we stick to empirical determination of potential parameters. Such inefficiency of interatomic potentials is partly due to the difficulty in deriving them from macroscopic information obtained by experiments.

That being the case, is it possible to study the structure of materials using

(a)



(b)



(c)

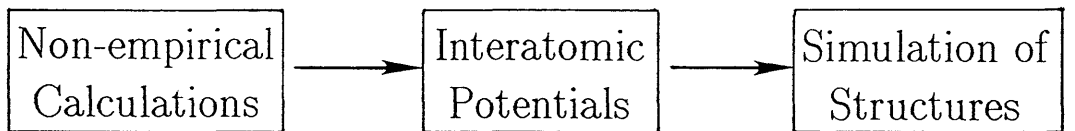


Fig.1-1 Three different procedures for the simulation of material structures.

non-empirical electronic structure calculations? (Fig.1-1(b)) There exist a well-known example of such an approach by M.L. Cohen and his colleagues (Yin and Cohen, 1980; Cohen, 1989 and see references therein). Using the LDF method, they successfully obtained the most stable structure of crystalline silicon. In these studies, a certain atomic configuration is first assumed, the electronic structure is calculated non-empirically, the forces working on each atom at the position are derived, and we then let the atoms move to obtain the optimum configuration. The simulated annealing method (the *ab initio* molecular dynamics method) developed very recently by Car and Parrinello (1985) would give a more efficient approach along this line.

Although such a non-empirical approach would in principle be more desirable, there are many difficulties left as future problems. The most serious one is the huge amount of computational time and memories required for the calculation, which limit the number of atoms and electrons in the unit cell of the crystal. Thermal effects are also difficult to include. Such limitations are serious even for the simulation of such a common material as silica (SiO_2) which we are going to discuss in the present thesis.

We have mentioned two approaches to the simulation of atomic configurations; the simulation using empirical interatomic potentials and the simulation by non-empirical calculations of electronic structures. Although the latter has more predictability, so far it is not feasible in many cases. The former approach has also been favored in using several kinds of simulation techniques such as the lattice dynamics or the molecular dynamics where empirical potentials are fed. However, it is evidently more desirable to first derive the non-empirical potentials which are then fed into the molecular dynamics.

From this point of view, in the present thesis, we have combined these two approaches to investigate the structural properties of complex crystals, that is, we have derived interatomic potentials from the first-principles electronic-structure calculation and applied them to the molecular dynamics (MD)

simulation of crystals (Fig.1-1(c)). There have been some attempts of this kind to derive the intermolecular potentials of H_2O (Carravetta and Clementi, 1984; Yoon, Morokuma and Davidson, 1985) or alcohol (Nakanishi, Ikari, Okazaki and Touhara, 1984) from cluster calculations with the HF-SCF method, or those for ionic crystals by the modified-electron-gas (MEG) method (Gordon and Kim, 1972). However, in the former calculations, the molecules are treated as rigid bodies, which is not true, and the latter method is not applicable to materials with substantial covalency. Thus we have to develop a different method for wider applications.

The material we have chosen as a target of our structural simulation is silica (SiO_2), which has physical, geophysical and mineralogical significances as follows:

(1) Silica is a geophysically important material in the Earth. The cosmic abundance of nonvolatile elements is shown in Table 1-1 (Anders and Ebihara, 1982). If one assumes that the Earth accreted from a nebula of solar composition and takes the core composition to be roughly Fe_2O , one can estimate the composition of the terrestrial mantle from these cosmic abundances as shown in Table 1-2. Since MgO easily reacts with SiO_2 , dominant components of the crust of the Earth are magnesium silicate such as MgSiO_3 or Mg_2SiO_4 . However, considering that silica (SiO_2) is a basis for the silicates, we may say that silica is the most significant mineral of the Earth. Thus it becomes important for the simulation to predict the behavior of silica under extremely high pressure. In the present study, such a high-pressure regime is thus regarded as an important test-bed.

(2) Silica has, in spite of its simple chemical composition, various polymorphs and shows complicated phase transitions when temperature or pressure are changed (see section 1.3). Some of the polymorphs are known to exist stably at room temperature and normal pressure. These polymorphs show a variety of densities ($2.3 - 4.3 \text{ g/cm}^3$) and bulk moduli ($18 - 296 \text{ GPa}$). It is an interesting

Table 1-1 Cosmic abundance of nonvolatile elements (relative to 1000 atoms of Si) (Anders and Ebihara, 1982).

Mg	1075
Al	84.9
Si	1000
Ca	61.1
Ti	2.4
Fe	900

Table 1-2 Constitution of the model Earth (wt. %).

Mantle	
MgO	27.0 %
SiO ₂	37.5 %
Core	
FeO	35.5 %

problem to confirm whether these various polymorphs are reproduced with common interatomic potentials.

(3) The features in the structural properties of silica is attributed to the framework structure of the corner-linked SiO_4 tetrahedra. Silica, a prototype of framework materials, can also become glass easily.

(4) Silica has both covalency and ionicity. There have not been reported pairwise interatomic potentials that can well reproduce the structural properties of the polymorphs of silica. Nevertheless vitreous silica and silicate are shown to be simulated quite well by pairwise interatomic potentials (for the reasons given in Section 1.2). The validity of the pairwise potentials should be checked using more microscopic and non-empirical approaches.

In the structural study, we have used the MD method to fulfill the following requirements:

(1) We discuss the dynamical stability of the polymorphs, that is, the stability against thermal fluctuation of the system. We note that empirical total-energy calculations optimize the system by varying some parameter that preserves the symmetry of the crystal. This procedure, however, can be quite inadequate, since in some cases the crystal disintegrates upon removing symmetry restrictions. Any symmetry restriction for the crystal structures is absent in the MD, so that the dynamical stability is far more crucial a test.

(2) We simulate the thermally induced phase transitions, for which static simulations are inadequate.

(3) We treat the structural transformation accompanied by the rearrangement of the framework structure of silica. Atomic motions of a large scale such as diffusion process must be also discussed.

The present thesis addresses these points on the structural simulation of silica starting from the derivation of the interatomic potential to its application, aiming eventually material design.

Section 1.2. Historical survey of the simulation of silica and silicate

Interatomic potentials of silica applicable to MD simulations were derived and used for the first time by Woodcock, Angell and Cheeseman (1976). The functional form employed is

$$U_{ij}(r) = Q_i Q_j / r + (1 + Q_i / n_i + Q_j / n_j) b \exp [(a_i + a_j - r) / \rho] ,$$

where r is the interatomic distance between the i -th and the j -th atoms, Q_i is the ionic charge, n_i is the number of outer shell electrons, and b and ρ are constants. Using the empirical value of ρ for BeF_2 and formal charges $Q_{\text{Si}} = +4e$ and $Q_{\text{O}} = -2e$, they optimized b and a_i by trial and error so that the radial distribution function (RDF) of vitreous SiO_2 is reproduced by the constant-volume MD simulation. Though their potentials are pairwise, they can reproduce the four-fold Si-O coordinations and principal features of the RDF. This was surprising because it had been believed that many-body potentials with bond-angle force constants, such as the Keating potential (Bell and Dean, 1972; Gaskell and Tarrant, 1980), was needed for the simulation of the structure of SiO_2 , which was the obstacle to MD simulations by computers.

Since this pioneering and illuminative work was reported, many papers appeared concerning the MD simulation of vitreous or liquid SiO_2 -related materials with several kinds of empirical pair potentials (see, for example, Matsui and Kawamura, 1980, 1984, 1987; Soules and Busbey, 1981; Soules, 1982; Matsui, Kawamura and Syono, 1982). It is quite difficult, however, to evaluate the validity of the potentials only by comparing the simulated RDF or X-ray interference functions with experimental results. In fact, some of the empirical potentials of silicate cannot preserve crystalline structures without symmetry restriction in MD. There is a tendency to regard that the simulation, even if empirical, should be valuable for vitreous and liquid states, for which the real experiments with high temperatures are difficult. However, we have to be very

careful in evaluating the simulation, because the MD results are usually sensitive to slight differences of potentials.

The simulations of crystalline silicate are useful for deriving the interatomic potentials, for much more experimental data to be compared with the simulation are reported on the crystals of important minerals. The early simulations were done by static energy-minimization method (Catlow and Norgett, 1976): each atom is first put at ideal position of a crystal observed in the experiments, and then the structure is relaxed until the internal lattice energy of the crystal is minimized. Empirical interatomic potentials are tested and modified so as to reproduce the observed crystal structures. We can modify the procedure, in which the atoms are fixed at the ideal positions and potential parameters are optimized to minimize the lattice energy (Busing, 1981; Miyamoto and Takeda, 1980; Parker, 1982, 1983). The method was sophisticated by including the hydrostatic pressure or external strain field in the optimization process (Busing and Matsui, 1984; Matsui and Busing, 1984; Price and Parker, 1984; Matsui, Akaogi and Matsumoto, 1987). Since silicates usually have several metastable polymorphs, the empirical potentials obtained from some of the polymorphs can be checked if they can reproduce other polymorphs.

As far as magnesium silicates (MgSiO_3 , Mg_2SiO_4) are concerned, empirical pair potentials have been shown to reproduce the structure and the elastic constants of most of the polymorphs rather well. The success may be attributed to the fact that the structures of the silicates are very close to the close-packed rather than framework system. On the other hand, the polymorphs of pure SiO_2 , which are far from close-packed and show wide variation of densities and bulk moduli as seen in the previous section, should be much more difficult to simulate by pair potentials as unsuccessful attempts indicate (Parker, 1982; Catlow, Thomas, Parker and Jefferson, 1982; Erickson and Hostetler, 1987) except for the densest polymorph, stishovite (Matsui and Kawamura, 1987). It should be noticed here that the MD simulation of SiO_2 by Woodcock et al. (1976) apparently worked because they concentrated on vitreous states only. We have

tested their pair potentials for crystals, and the MD result shows that initial low-quartz and low-cristobalite structures transform, respectively, into higher-symmetry states, that the bulk modulus of quartz is significantly larger than the experimental values, and that the Si-O interatomic distance is not reproduced unless a constant-volume (unphysical) condition is used: Their potentials are much too simple for crystal simulation.

It is understandable, then, that more and more complicated interatomic potentials had to be introduced to empirically simulate SiO_2 . The most successful one is so-called shell model with a Keating-type bond-bending term (Catlow, Freeman and Royle, 1985). The shell model was first introduced to reproduce the phonon dispersions of ionic crystals (Cochran, 1961; Catlow, Dixon and Mackrodt, 1982). In the model, the charge of each ion is divided into two parts; the core charge and the shell charge. The shell charge, which is coupled to the ionic core with a harmonic potential, represents the distortion of the charge distribution against the atomic displacement. Interaction between the cores are described by the ordinary pair potentials and the bond-bending term for the O-Si-O bending is added. The potential parameters are determined empirically so that structural, elastic, dielectric and lattice dynamics properties are reproduced. The agreement between the theory and experiments on all the polymorphs of SiO_2 except for stishovite is good. It is very difficult, however, to apply the potential to the MD simulation, and high-pressure research is not reported yet because the potential parameters are unlikely to be applicable at high pressure. This potential cannot be applied to stishovite either because it has six-fold Si-O coordination instead of usual four-fold coordination. The potential of this type is also used for silicate (Wall and Price, 1988). Another many-body potential, which does not use the shell model but also empirical, is reported recently by Stixrude and Bukowinski (1988). The potential can reproduce the structures and the bulk moduli of low-quartz and coesite, and the enthalpy difference between them, although, again, the potential cannot be applied to stishovite.

There are several non-empirical approaches to the study of the interatomic

potentials of silica. Apart from the approaches by semi-empirical extended Hückel theory (EHT) and CNDO (complete neglect of differential overlap) theory, the first *ab initio* calculation was done on the geometry optimization of H_4SiO_4 and $\text{H}_6\text{Si}_2\text{O}_7$ clusters (Newton and Gibbs, 1980; Gibbs, 1982). They used the Hartree-Fock Self-Consistent-Field (HF-SCF) method and showed that the Si-O bond length and the bond angles in silicates are reproduced well by the cluster calculation despite the small size and excess hydrogens in the cluster. Lasaga and Gibbs (1987) derived interatomic potentials of such cluster calculations and applied them to the static simulation of crystalline silicates and silica. They found that, as far as they limit themselves to a narrow parameter range, pair potentials could not reproduce low-quartz and that three-body potentials were needed. They moved on to reproduce the structure and bulk modulus of low-quartz using covalent three-body potentials, although the calculated elasticity exhibits anisotropy opposite to the experimental results: C_{11} is much larger than C_{33} in the simulation.

Other first-principles approaches are based on bulk calculations. Since the unit cell of silica and silicates are usually very large, it is very hard to employ the *ab initio* Local Density Functional (LDF) method. In the early works, therefore, the Modified Electron Gas (MEG) method (Gordon and Kim, 1972) was used for the geometry optimization of silicates (Hemley, Dickson and Gordon, 1987; Wolf and Bukowinski, 1987) and silica (Jackson, 1986). This method is combined with lattice dynamics calculation. In the MEG method, charge distribution of the crystal is approximated by the sum of the charge distribution of isolated closed-shell atoms or ions. Therefore, it is difficult in principle to apply the method to any oxide because isolated O^{2-} ion is never stable. Quantitative agreement of the calculations with experiments is, in fact, not so good.

The LDF method can be used if the unit cell is small enough. It was employed in a calculation of SiO_2 with the fluorite structure, which has only one SiO_2 unit in a primitive cell and was once regarded as a candidate for a high-

pressure phase of silica, though they were shown to be unstable at pressure below 170 GPa (Carlsson, Ashcroft and Williams, 1984; Bukowinski and Wolf, 1986). Recently, the geometry optimization of low-cristobalite was done by Allan and Teter (1987) using the simulated annealing method by Car and Parrinello (1985). They optimized five structural parameters under the restriction of space-group symmetry and obtained quantitatively good agreement with the experiment at very low temperature and normal pressure. Very recently Park, Terakura and Matsui (1988) calculated the total energy of stishovite, fluorite-structure SiO_2 and SiO_2 with the $Pa\bar{3}$ structure (see section 3.2) as a function of molar volume by the Full-potential Linear Augmented Plane Wave (FLAPW) method, which is reliable even at high pressure. $Pa\bar{3}$ silica is suggested to be a possible high-density phase of silica by a previous MD study (Matsui and Matsui, 1988). Park et al. have predicted that $Pa\bar{3}$ silica phase is stabler than stishovite at pressure above 60 GPa.

As we have mentioned above, many empirical approaches have been reported as regards the structural simulations of silica and silicates. They might be powerful means of understanding experimentally observed properties of the minerals. Such empirical approaches are nevertheless insufficient to predict unknown structures and their properties: we should note there is a large gap between predicting structural properties of materials and simulating well-known structures with use of the knowledge of the structure itself. For design and prediction of structures of materials, non-empirical approaches are desirable, although those reported so far have only succeeded in obtaining restricted geometries after huge calculations of electronic structures of bulk crystals.

From this point of view, in the present thesis, we show for the first time that we can derive *interatomic potentials for silica* from *non-empirical and tractable cluster calculations*. Once the interatomic potentials are obtained, they can be fed into dynamical simulations of complicated bulk structures using the MD method. It is also reported for the first time that a *pairwise* interatomic potential can

reproduce most of structural properties of crystalline silica with framework structures.

Section 1.3. Polymorphs of silica

In this section, we briefly introduce the known polymorphs of silica. The densities, bulk moduli, number of SiO_2 units in a unit cell and the space group of the polymorphs are summarized in Table 1-3 together with the phase diagram in Fig.1-2 (Hemley et al., 1988). All the polymorphs except for stishovite have framework structures of corner-linked SiO_4 tetrahedra. High-quartz, high-cristobalite and high-tridymite are the high-temperature phases of low-quartz, low-cristobalite and low-tridymite, respectively, and have the same connectivity of the SiO_4 tetrahedra as those in the low-temperature phases. The high-temperature phases are distinguished from the corresponding low-temperature phases by their higher symmetry and larger Si-O-Si angles.

The most stable phase at room temperature and normal pressure is low-quartz (or α -quartz), whose stereoscopic view is shown in Fig.1-3(a). It is characterized by three-fold screw axes, and coexisting four-membered and six-membered (-Si-O-) rings in the network structure. It is well known that low-quartz transforms into high-quartz (β -quartz) with six-fold screw axes above 846K, though recently an incommensurate phase was observed within a narrow temperature range ($\sim 2\text{K}$) between the α and β phases (Gouhara, Li and Kato, 1983; Dolino, 1988).

High-cristobalite (β -cristobalite) is obtained by heating low-quartz and is quenched to low-cristobalite (α -cristobalite) (Fig.1-3(b)) below 491K. The framework of the Si-O-Si bonds in cristobalite has the diamond structure and contains only six-membered rings. High-tridymite is similar to high-cristobalite but in this case the framework assumes the hexagonal diamond structure. Low-tridymite is not fully established as a pure polymorph of silica (Holmquist,

Table 1-3 Polymorphs of silica.

	Density (g/cm ³)	Bulk modulus (GPa)	SiO ₂ (unit/cell)	Space group
low-quartz	2.65	38	3	$P3_121(P3_221)$
high-quartz	2.35		3	$P6_222(P6_422)$
low-cristobalite	2.34	18	4	$P4_12_12(P4_32_12)$
high-cristobalite	2.17		8	$Fd\bar{3}m$
coesite	2.92	96	16	$C2/c$
low-tridymite				
high-tridymite	2.22		4	$P6_3/mmc$
stishovite	4.29	296	2	$P4_2/mnm$

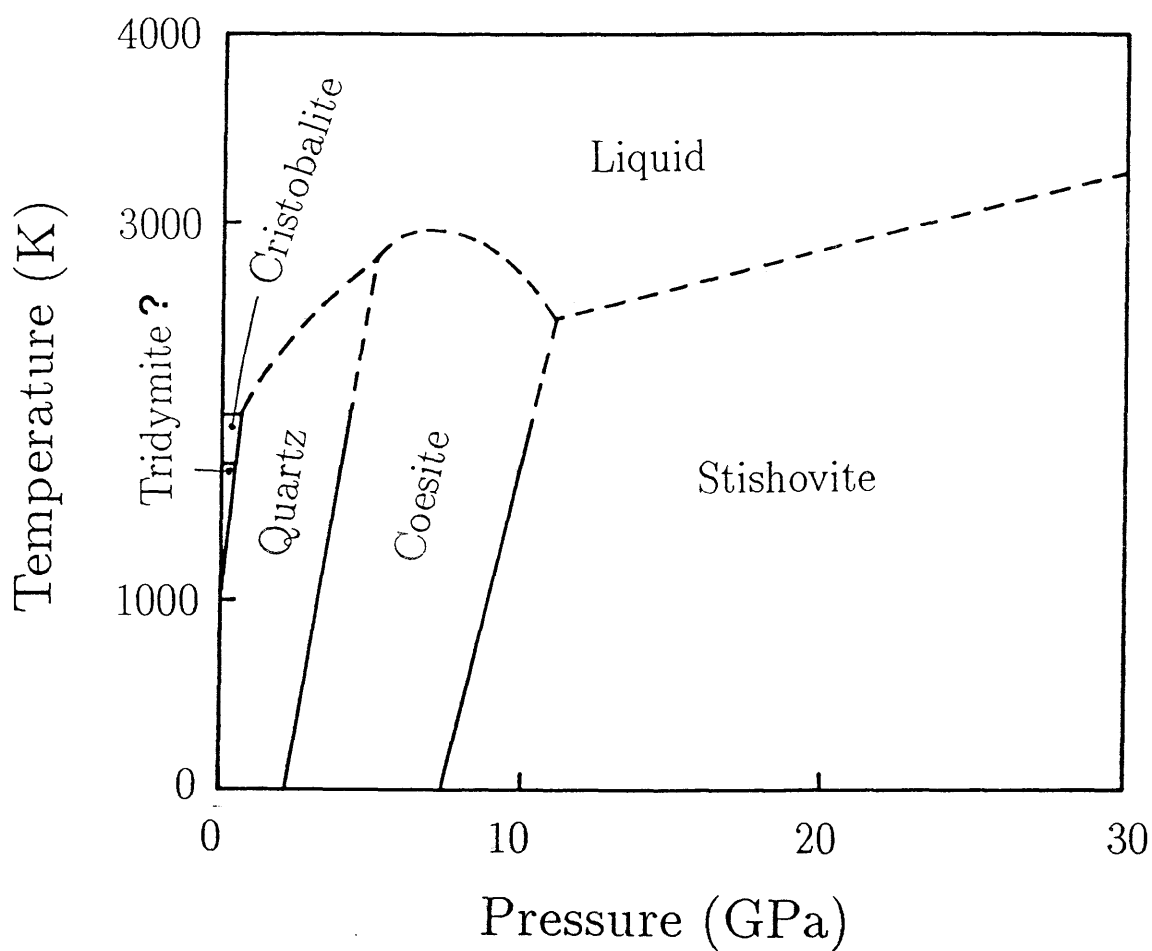


Fig.1-2 Phase diagram of silica (Hemley et al., 1988).

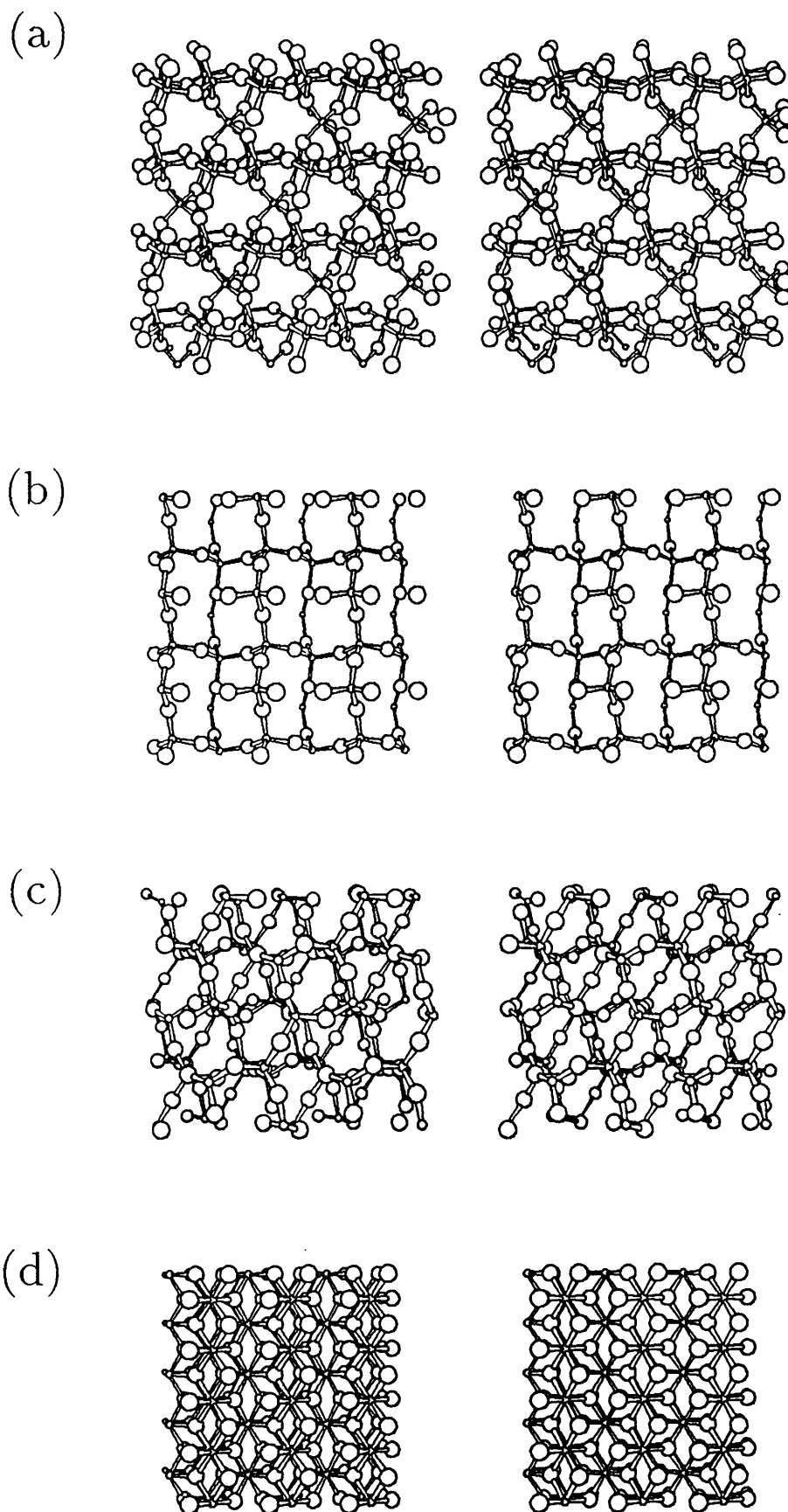


Fig.1-3 Stereoscopic views of polymorphs of silica: (a) low-quartz, (b) low-cristobalite, (c) coesite, and (d) stishovite. Small spheres represent silicon atoms and large spheres oxygen atoms.

1961), although several low-temperature phases are reported with extremely low-symmetry of space group *Cc* including large number of atoms.

Coesite has a monoclinic unit cell of rather low symmetry (Fig.1-3(c)). Four-membered rings and linear Si-O-Si configuration at some oxygen sites are characteristic of the structure.

Stishovite, the densest phase of silica ever known, is remarkable in that silicon atoms are located in the edge-shared octahedra of oxygen atoms (Fig.1-3(d)). The structure is the same as TiO_2 rutile and is almost close-packed. Experimental and theoretical researches for the denser phase of silica are still under way (Park, Terakura and Matsui, 1988; Tsuchida and Yagi, 1989).

These are the natural polymorphs of silica so far known. Vitreous silica is also known to have a network structure of corner-linked SiO_4 tetrahedra at least at low pressures.

Section 1.4. Organization of the present thesis

In Chapter II, an interatomic potential of silica is derived from the first-principles cluster calculations. The possibility and limit of the pairwise interatomic potentials are examined.

The formalism of the MD simulation is briefly depicted in Chapter III. The pairwise interatomic potential is then applied to the MD simulation of polymorphs of silica at normal and high pressure condition in this chapter. It is shown for the first time that the pairwise potential can reproduce the structural properties of virtually all the known polymorphs of silica.

Thermally induced structural phase transition of quartz, which is successfully reproduced by the MD, is described in Chapter IV. The dynamical character of the phase transition is elucidated there.

New pressure-induced structural transformations of crystalline silica at room temperature are reported in Chapter V. Two novel structures of silica are

obtained, which comprise silicon atoms of both four-fold and six-fold coordinations. The mechanism of compression, that is, diffusionless coordination changes under pressure is confirmed.

In Chapter VI, a preliminary application of our cluster approach to silicate is reported. Potential parameters for magnesium are derived from cluster calculations and are applied to four polymorphs of magnesium silicate.

Chapter VII is devoted to concluding remarks. A conjecture respecting an anomalous diffusion property of silicate melt is presented with a preliminary simulation of silica melt. A summary of the present thesis is given at the end of the chapter.

Chapter II. Interatomic Potentials of Silica

Section 2.1. Method of the cluster calculation

In this thesis, we start from a non-empirical cluster calculation method to obtain interatomic potentials in the SiO_2 system. The cluster method has advantage over the bulk method since computational time required is not gigantic in obtaining the total energy and the potential energy surfaces for deformations, provided that the cluster is not too large. The other advantage is that, since the potential energy surfaces of a small cluster do not contain long-range parts of interatomic potentials from distant atoms, we can separate the short-range parts, which relieves the difficulty in extracting each two-body or, if necessary, three-body interatomic potentials from the total energy of the system. The long-range part in SiO_2 , a good insulator, is considered as a Coulomb interaction between ionized atoms.

The cluster method has, of course, an intrinsic flaw originating from its non-periodicity: the electronic structure near the surface of the cluster may be somewhat different from that in the bulk. In the case of an insulator, however, the electrons are comparatively localized, so that the short-range interatomic potentials in a cluster are expected to be similar to those in a bulk. This is supported by the fact that the Si-O interatomic distance is almost the same both in the H_4SiO_4 cluster and in crystalline silica or silicate (Gibbs, 1982). We should note that, when we treat a metallic system, it is dangerous to use the information from a cluster calculation, since the interaction of ionic cores with confined electrons is quite different from that with free electrons. Even in this case, however, the short-range interaction between the ionic cores of each atoms may be derived from cluster calculations.

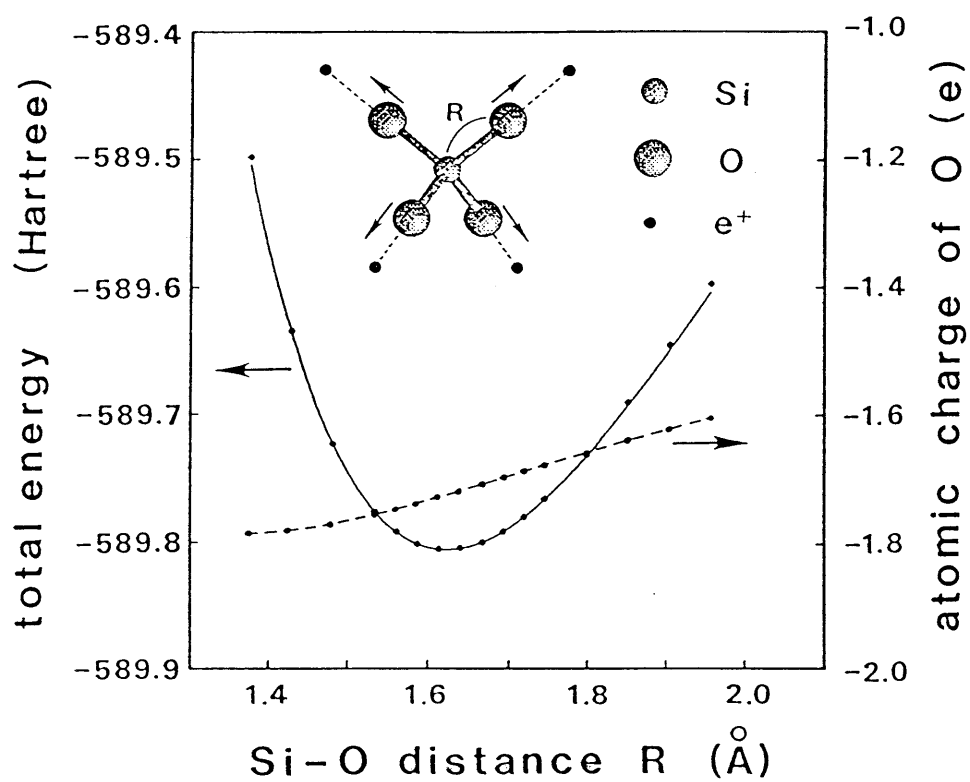
The most conspicuous feature of the structure of silica except for stishovite is, as mentioned in chapter I, the framework of corner-linked SiO_4 tetrahedra. If we want to reproduce the structures of all the polymorphs and the glass or melt with common interatomic potentials, the SiO_4 tetrahedra must be first preserved

in the simulation with the model potentials. Thus we start from the total energy calculation of a tetrahedral SiO_4 cluster deforming its shape and then best fit the parameters in the potential-functions so that the obtained potential-energy surfaces are reproduced by the summation of the interatomic potentials. The validity of pair-potential approximation could be checked by the reproducibility of the potential-energy surfaces.

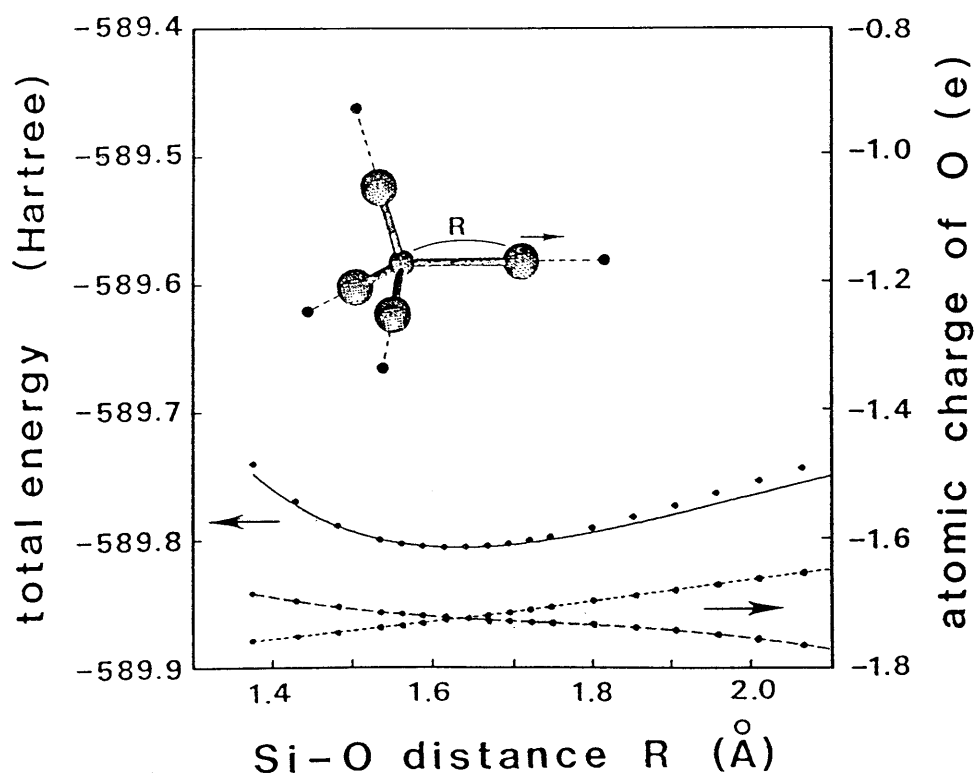
In the total-energy calculation, an SiO_4^{4-} ionic cluster rather than a neutral SiO_4 is used, because Si readily gives up electronic charge to oxygen atoms. We regard the cluster as embedded in a crystal, so that we add four point charges, e^+ , of unit charge as shown in the inset of Fig.2-1, which guarantee the charge neutrality and also mimic the Madelung potential arising from the rest of the crystal. The distance between an oxygen atom and the nearest point charge is set equal to usual Si-O distance in silicates (1.65\AA).

The total energy of the cluster is then calculated using the *ab initio* Hartree-Fock self-consistent-field (HF-SCF) method. Since the SiO_4^{4-} cluster has closed-shell electronic state as seen from the formal charge of Si^{4+} and O^{2-} , the cluster has no dangling bonds. This is convenient for the HF-SCF calculation. The gaussian basis functions employed are (12s8p)/ [5s3p] (McLean and Chandler, 1980) with two d functions (with the exponent, $\alpha=0.118, 0.424$) (Huzinaga et al., 1984) for silicon and (9s5p)/ [3s2p] with p functions (with $\alpha=0.059$) (Dunning and Hay, 1977) for negative ion state of oxygen. The importance of d-orbitals has already been noted by Newton and Gibbs (1980). We assume no electron orbitals around the point charges so that the charge-transfer to the point charges does not occur. Although an isolated SiO_4^{4-} cluster is unstable as known from the positive one-electron energies, it is stabilized by the ligand field of the positive charges. In the previous cluster calculations by Newton and Gibbs (1980), Gibbs (1982), and Lasaga and Gibbs (1987), hydrogen atoms are put around the cluster for charge neutrality. We do not prefer their method since it is difficult to evaluate the interaction between the hydrogen atoms and the other atoms.

(a)



(b)



(c)

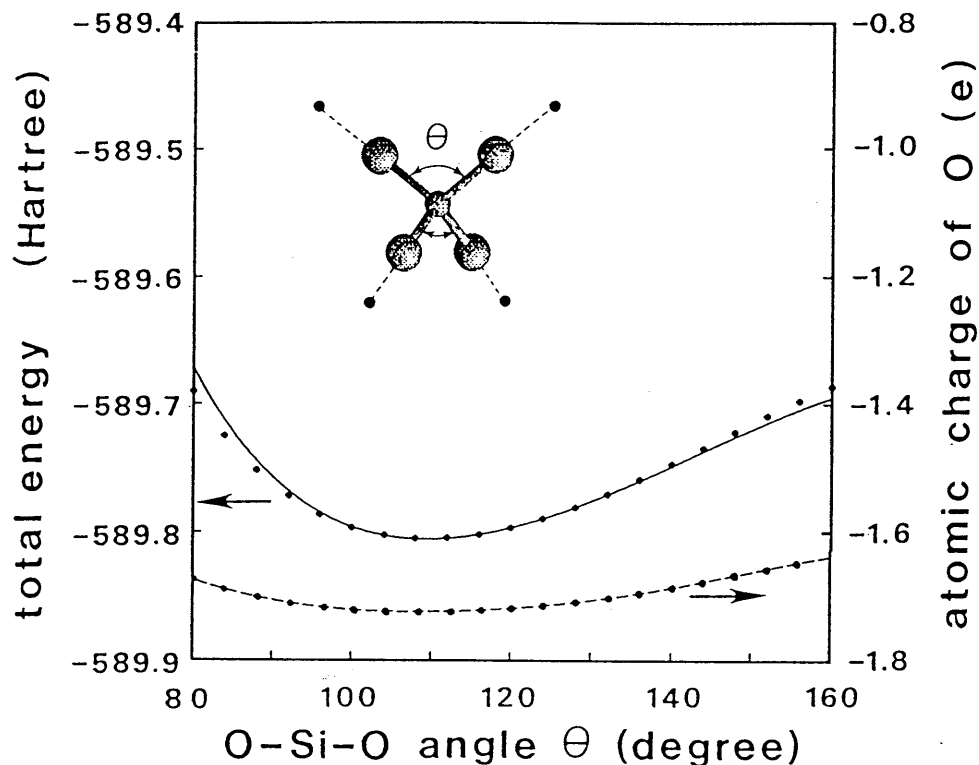


Fig.2-1 Total energy and the Mulliken charge on an oxygen atom for three deformation modes of a $\text{SiO}_4^{4-}\text{-}4\text{e}^+$ cluster shown in the insets: (a) T_d mode, (b) C_{3v} mode and (c) D_{2d} mode. The full circles are the cluster calculation, solid lines are the fitted potentials, and the broken curve is a guide to the eye. O- e^+ distances are set equal to 1.65Å. In (b), the Mulliken charge shown by the dashed curve is for the moved oxygen, while that shown by the dotted curve is for the fixed oxygens.

Table 2-1 Potential parameters obtained in this study (Set-ID: TNM).

	Q/e	a (Å)	b (Å)	c ($\text{kcal}^{1/2}\text{Å}^3\text{mol}^{-1/2}$)
O	-1.200	2.0474	0.17566	70.37
Si	+2.400	0.8688	0.03285	23.18

Section 2.2. Potential energy surfaces and pairwise interatomic potentials

The potential-energy surfaces (total energy of the cluster as a function of the atomic configuration) are obtained by changing the Si-O distances or O-Si-O angles with three different modes. One potential-energy surface is depicted in Fig.2-1(a), in which we stretch all the Si-O bonds keeping the T_d symmetry of the cluster. The result is shown with full circles. The distance between the point charges and the nearest oxygen atom is always kept constant. The equilibrium Si-O distance at the potential minimum is 1.61\AA , which is very close to the experimental value in the tetrahedrally coordinated silica ($1.60\text{--}1.61\text{\AA}$). If d-functions for polarization are not included in the basis set of the HF-SCF calculation, the equilibrium Si-O distance is elongated to 1.64\AA . As we shall see (Section 3.2), even this difference of 0.03\AA is substantial enough to destroy the tetrahedral coordination in some polymorph.

We have also obtained the results for C_{3v} mode (Fig.2-1(b)), in which only one Si-O distance is changed, and D_{2d} mode (Fig.2-1(c)), in which O-Si-O angle is varied with constant Si-O distance (1.635\AA). In the D_{2d} mode, the point charges are put on the extended line of Si-O bonds at each angle, where $\theta=180^\circ$ and $\theta=0^\circ$ correspond to planar and linear configurations, respectively, and the equilibrium angle of $\theta=109.5^\circ$ is close to the tetrahedral angle.

In spite of the covalent character of the bonds, it turned out that all of these three potential energy surfaces can be fitted well by a sum of pairwise interatomic potentials. We have employed the functional form,

$$U_{ij}(r) = U_{ij}^{\text{Coulomb}}(r) + f_0(b_i+b_j)\exp\left(-\frac{a_i+a_j-r}{b_i+b_j}\right) - \frac{c_i c_j}{r^6}, \quad (2.1)$$

which consists of Coulomb interaction with some corrections discussed below, Born-Mayer-type repulsion and an additional, power-law interaction. Here r is

the distance between atoms and a_i (b_i) is the effective radius (softness parameter) of the i -th atom with the standard force $f_0 = 1\text{kcal}\text{\AA}^{-1}\text{mol}^{-1}$. We also include Coulomb interactions with the point charges. Although the third term has a $1/r^6$ form, this does not stand for the van der Waals interaction due to a virtual deformation of the wavefunctions (which is not included in the HF-SCF method) but represents a correction to the core-repulsion term. Thus it is possible to employ the other functional form. The inclusion of the correction term has turned out to be quite efficient for reproducing the potential-energy surfaces.

A caution must be made in evaluating Coulomb interaction in the cluster, because the effective charge in the bulk, Q_i , is different from that in a SiO_4^{4-} cluster, \tilde{Q}_i : in terms of the fractional charge, Δn , transferred from a Si atom to an O atom per Si-O bond, we have $Q_{\text{O}} = -2\Delta n e$ and $Q_{\text{Si}} = 4\Delta n e$ in the bulk, while we have $\tilde{Q}_{\text{O}} = -(1+\Delta n)e$ and $\tilde{Q}_{\text{Si}} = 4\Delta n e$ in the cluster. Here e is the elementary charge. We express the Coulomb interaction in the cluster as a sum of long-range and short-range parts as

$$\begin{aligned} U_{ij}^{\text{Coulomb}} &= \tilde{Q}_i \tilde{Q}_j [1 - g_{ij}(r)] / r + Q_i Q_j g_{ij}(r) / r, \\ g_{\text{SiO}}(r) &= (1 + \zeta r) \exp(-2\zeta r), \\ g_{\text{OO}}(r) &= [1 + 11(\zeta r)/8 + 3(\zeta r)^2/4 + (\zeta r)^3/6] \exp(-2\zeta r). \end{aligned} \quad (2.2)$$

The correction, $g_{ij}(r)$, in the long-range part (the first term) involving \tilde{Q} reflects the distribution of the excess charge of oxygen, for which we assume a hydrogen-like orbital with a radius $1/\zeta$ here. The radius should be of the order of the ionic radius of O, so that we employ $1/\zeta = 1.4\text{\AA}$ following Pauling (1960). Since the remaining short-range part is expected to be insensitive to the environment, we use the bulk Q_i there. Once the parameters a_i , b_i , c_i are optimized from the cluster calculation, we switch \tilde{Q} back into Q (i.e., $U_{ij}^{\text{Coulomb}} = Q_i Q_j / r$) in the bulk simulation. Thus the final pair potential, eq.(2.1), has the same functional form as suggested by Gilbert (1968) and Ida (1976).

From the cluster calculation, the charge obtained by the Mulliken analysis, which is $\tilde{Q}_O \sim -1.7e$ (i.e., $\Delta n \sim 0.7$) for the equilibrium bond length, is shown to be a function of the Si-O distance (broken lines in Fig.2-1). The feature that the atomic charge varies with the bond length clearly indicates a many-body character of interatomic forces in systems with nonzero covalency. The physical mechanism will be discussed in more detail in Section 2.3. To concentrate on the pair-potential approach, however, we have used constant Q_i (\tilde{Q}_i) as a first step. Since small cluster results are insufficient to determine the long-range Coulomb interaction, and because the absolute value of Mulliken charge itself depends on the choice of the basis functions, we have not included Δn in the fitting procedure. Instead we tried several fixed values of Δn around the Mulliken charge. Among the trial values studied here, the fitted parameters with $\Delta n = 0.6$ reproduce the best crystal parameters.

Since the fitting procedure for a_i , b_i , c_i is nonlinear, more than one set of parameters are obtained. We have chosen the one (Table 2-1) which optimizes the structure (density) and compressibility of low-quartz (Levien, Prewitt and Weidner, 1980) in a static simulation by the program WMIN (Busing, 1981; Busing and Matsui, 1984). The potential-energy surfaces best fitted by the pair potentials are shown with solid lines in Fig.2-1. It should be mentioned that the best-fit potential reproduces the potential surface in a wide range of Si-O or O-O distances, which correspond to large deformations. In particular, this guarantees the reliability of the pair potentials even at high pressure, in which small interatomic distances occur.

Although both covalent and ionic characters should be present in silica, one would consider that tetrahedral units indicate dominant covalent bonding. The present result shows that, at least in the minimal local unit, the potential-energy surfaces can nevertheless be reproduced by summation of pairwise potentials. The validity of the pairwise interatomic potentials are further tested in the MD simulation of the polymorphs in the next chapter.

Section 2.3. Effect of the environment potential

Before turning to the MD study, we examine in this section the effect of the environment potential, that is, the role of the positive charges put around the cluster.

In the previous section, the distance between an oxygen atom and the point charge, which we write $d(\text{O-e}^+)$ hereafter, is fixed at 1.65\AA , for which the equilibrium Si-O distance (1.61\AA) is very close to that in crystalline silica ($1.60\text{--}1.61\text{\AA}$). If we set $d(\text{O-e}^+)$ 3.3\AA , however, the equilibrium distance for Td deformation is elongated to 1.66\AA as shown in Fig.2-2.

By subtracting the interaction between the point charges and the rest of the cluster, we can obtain the net potential-energy surface of the SiO_4^{4-} cluster. Since we have assigned no electron orbitals around the positive point charges, they do not accompany electron clouds, so that the interaction with the rest of the cluster can be evaluated as pure Coulomb interaction. If we use effective charge \tilde{Q}_i for Si and O described in Section 2.2, it is written as

$$U_e(Q) = \sum_{\langle \mu \nu \rangle} e^2 / r_{\mu \nu} + \sum_{i, \mu} \tilde{Q}_i e / r_{i \mu} \quad (2.3)$$

where $r_{\mu \nu}$ is the distance between the μ -th and ν -th positive charges, and $r_{i \mu}$ is that between the μ -th positive charge and the i -th ion. In calculating the nearest O-e⁺ interactions, we neglect the effect of the electron distribution of oxygen ion or its deformation due to the positive charge. However, the distance is fixed in each of the potential-energy surfaces, so that the inclusion of the electron distribution or the bonding effect causes a constant shift of U_e . The effect of the environmental change can be clarified by comparing the net potential-energy surfaces with $d(\text{O-e}^+) = 1.65\text{\AA}$ and $d(\text{O-e}^+) = 3.3\text{\AA}$ shown in Fig.2-3(a). In estimating U_e , we set $\tilde{Q}_{\text{Si}} = 2.8e$ and $\tilde{Q}_{\text{O}} = -1.7e$, though the result is insensitive to the choice of the effective atomic charge around these values. In addition to a constant

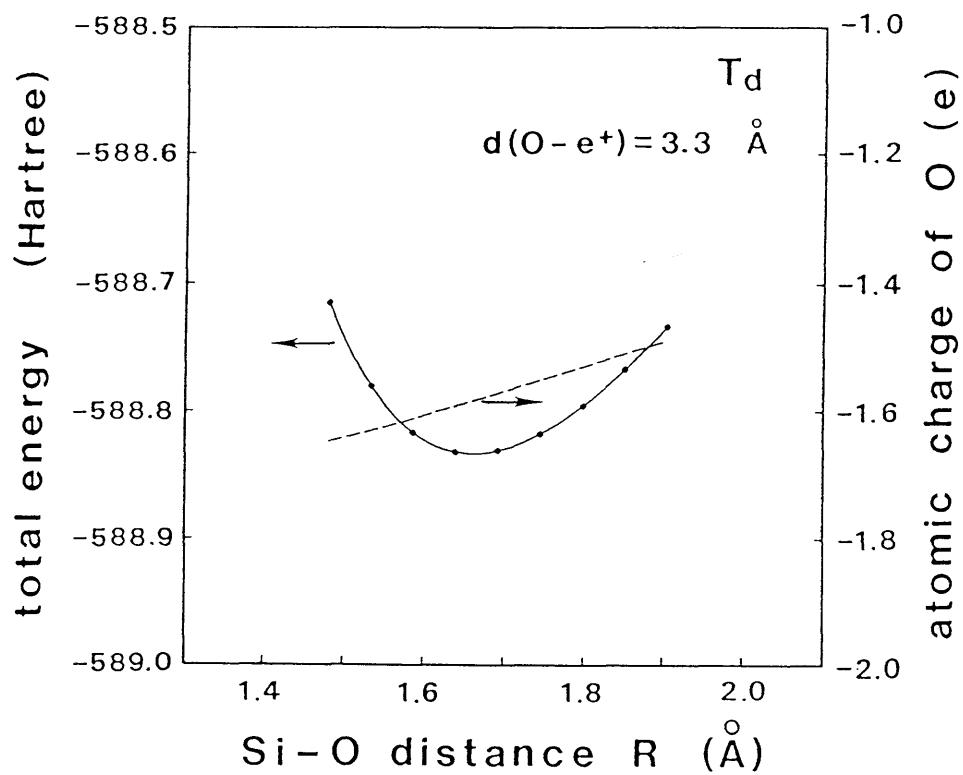


Fig.2-2 Total energy and the Mulliken charge on an oxygen atom for T_d deformation of a $\text{SiO}_4^{4-} - 4e^+$ cluster. The full circles are the cluster calculation, and the solid lines and the dashed lines are guides to the eye. $O - e^+$ distances are set equal to 3.30 \AA .

shift mentioned above, a quantitative difference is observed between the two net-potential-energy surfaces: for example, the Si-O distances of the potential minima are 0.03\AA larger in the case of $d(\text{O-e}^+)=3.3\text{\AA}$. However, for a doubled $d(\text{O-e}^+)$, which is an inconceivably large deformation in crystals, the difference of 0.03\AA is considered to be slight.

As shown in Fig.2-1, the atomic charges of silicon and oxygen atoms vary with the deformation of the cluster, which is not considered in the above analysis for U_e . To take account of the effect, we can evaluate the point-charge interaction as,

$$U_e(\rho)=\sum_{\langle\mu\nu\rangle} e^2/r_{\mu\nu} + \sum_{i,\mu} Z_i e^2/r_{i\mu} + \sum_{\mu} \int d\mathbf{r} e\rho(\mathbf{r})/|\mathbf{r}-\mathbf{r}_{\mu}|, \quad (2.4)$$

where Z_i is the atomic number or charge of nuclei, and $\rho(\mathbf{r})$ is the electron-density distribution obtained by the HF-SCF calculation for each configuration. The net potential-energy surfaces for Td deformation thus obtained by subtracting $U_e(\rho)$ from the total energy are shown in Fig.2-3(b) for the two values of $d(\text{O-e}^+)$ together with the energy difference between them. Remarkably, the energy difference is almost completely independent of the Si-O distance. The same result was obtained for C_{3v} deformation, and so it should be not accidental but an inherent characteristic of SiO_4^{4-} cluster.

The present result is very helpful for understanding the interatomic potential of SiO_2 . The potential consists of two parts: the short-range part which depends only on the local structure of the nearest-neighbor atoms and the Coulomb interaction extending beyond the nearest neighbor atoms. The former is insensitive to the environment, while the latter depends on the electron-distribution, which varies according to the deformation of the local SiO_4 structure. This is a many-body character of the interatomic potentials of SiO_2 , which cannot be handled even if we use bond-angle-dependent three-body potentials. To make matters complicated, the charge of an oxygen atom is determined not only by the Si-O distance but also by the configuration of the

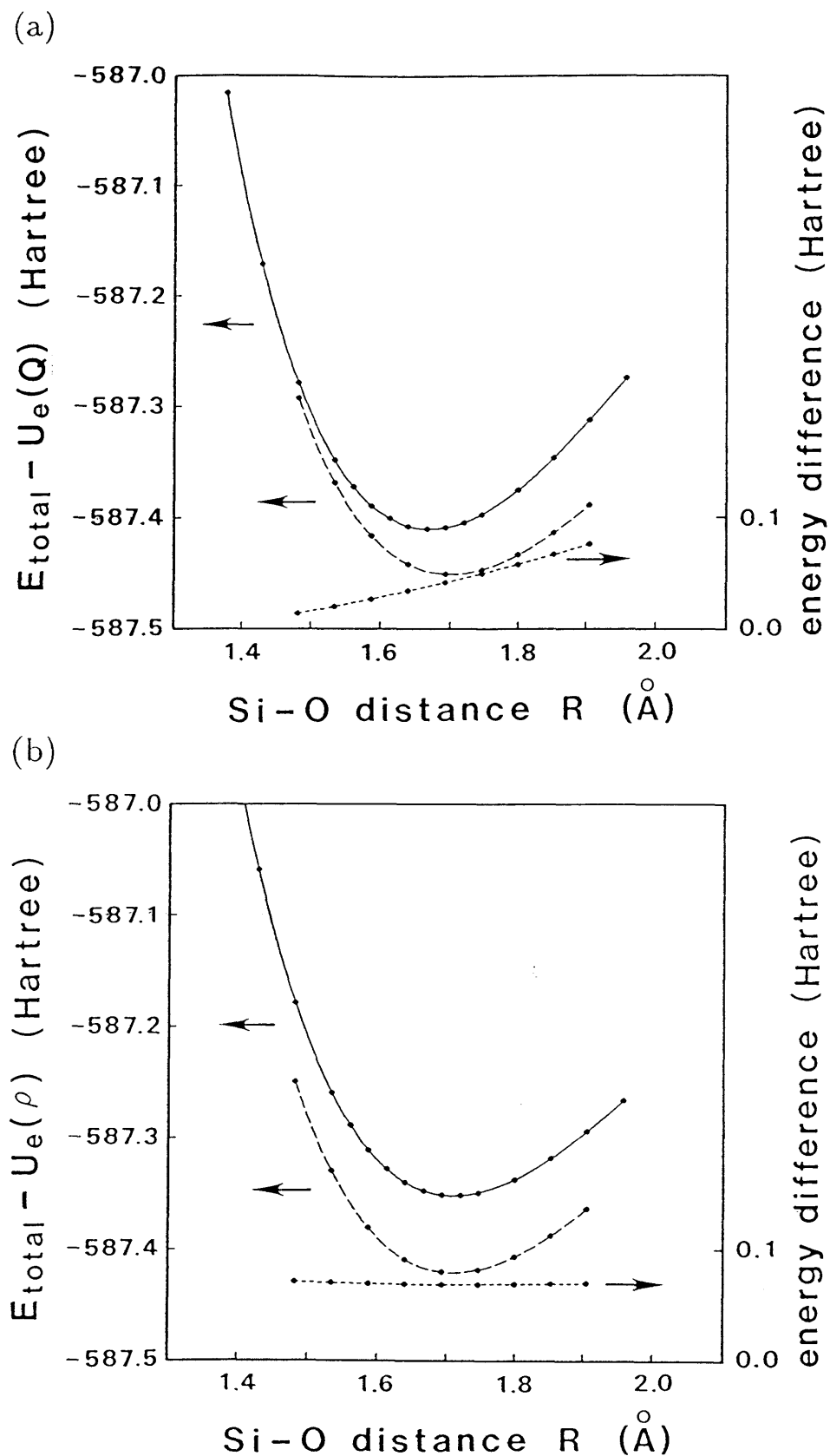


Fig.2-3 Net potential energy surfaces for T_d deformation of a $\text{SiO}_4^{4-}\text{-}4e^+$ cluster calculated using (a) fixed charges Q_i , and (b) electron-density distribution ρ . The full circles are the cluster calculation. The solid line is for the O-e^+ distances of 1.65\AA , and the dashed line is for 3.30\AA . The energy difference of these two net potential energy surfaces is shown with dotted lines.

other oxygen atoms. For example, the oxygen charge decreases as the Si-O bond is elongated in Td deformation (Fig.2-1(a)), whereas it increases in C_{3v} deformation (Fig.2-1(c)). Owing to the charge re-distribution, long-range Coulomb interaction changes, which may not be accommodated in the three-body potentials.

One way to take account of this many-body character is the shell model, which has already achieved a great deal of success in static simulation of silica (Catlow, Freeman and Royle, 1985) and silicate (Wall and Price, 1988) with empirical potential-parameters. In the shell model, the valence-electron-shell of an oxygen atom is bound to the ionic core with a harmonic potential, so that the charge re-distribution can be handled to some extent. It is quite understandable that such a flexible model is necessary in the reproduction of such properties as an accurate phonon dispersion. Completely non-empirical determination of the potential parameters are desired in future, although it would finally require bulk calculations.

Nevertheless, in this thesis, we employ a pairwise, rigid-ion potentials, which can more easily be applied to a variety of simulation techniques such as MD, since, as we have seen, the consequence of the above-mentioned many-body character is quantitatively not so large. The level of approximation should depend on how much accuracy we demand in the simulation. We can reproduce the structural properties of silica including phonon dispersions rather well within this pair-potential approximation as we shall see later.

Section 2.4. Larger clusters

If we do not demand the reproducibility for such extreme conditions as corresponding to doubled O-e⁺ distance, the interatomic potentials with the fixed effective charge (Q_i) should be quite adequate as evidenced by the deformation potential of the SiO₄ cluster reproduced by pairwise potentials (Section 2.2). Thus

the pairwise potential fulfills a necessary condition of reproducing crystal structures that the SiO_4 local units are maintained. It should be mentioned, however, that this is not the sufficient condition, for the detailed structure of the polymorphs of silica is characterized not only by the networking topology but also by the Si-O-Si bond-angles: low-temperature phases of quartz, cristobalite and tridymite are distinguished from the corresponding high-temperature phases by larger deviations of their Si-O-Si angle from 180° .

Since our interatomic potential is pairwise, the directional interaction by the p-orbitals of oxygen atoms, which causes the H-O-H bending in water molecules, is not included. However, the result of the MD simulation with the pairwise potentials shows that, in some polymorphs, Si-O-Si angles do deviate from 180° to $140^\circ - 150^\circ$ (Chapter III). This is achieved by the long-range interaction beyond the first-neighbor atoms. In this section we thus show the importance of the long-range interaction in the Si-O-Si bending first for the Si_2O_7 cluster.

As in the case of SiO_4^{4-} , $\text{Si}_2\text{O}_7^{6-}$ cluster with six positive charges is considered. All the Si-O distances and $d(\text{O-e}^+)$ are kept 1.635\AA and 1.65\AA respectively, and the total energy is calculated changing the bridging Si-O-Si angle, θ . The potential-energy-surface is shown in Fig.2-4(a) with full circles. No potential minima appear at $\theta \sim 143^\circ$ (or $\theta \sim 360^\circ - 143^\circ = 217^\circ$), which is the mean Si-O-Si angle in low-quartz. According to Gibbs (1982), the potential-energy-surface of $\text{H}_6\text{Si}_2\text{O}_7$ cluster, too, has only a shallow (<0.01 Hartree) potential minimum at $\theta = 142^\circ$, in which the depth depends on the Si-O distance. Here we have not optimized either the Si-O distances nor the position of the positive charges, which may explain the absence of a shallow potential minimum.

The result that the potential for the bending of the Si-O-Si angle (θ) is flat over a wide range of θ is physically very important. If we separate the Coulomb interactions to look at the short-range interaction part, $E_{\text{total}} - U_e(\rho)$, for the same deformation in Fig.2-4(b), the potential surface has a broad minimum at $\theta = 180^\circ$ in a sharp contrast. This implies that, although $\text{Si}_2\text{O}_7^{7-}$, a negatively

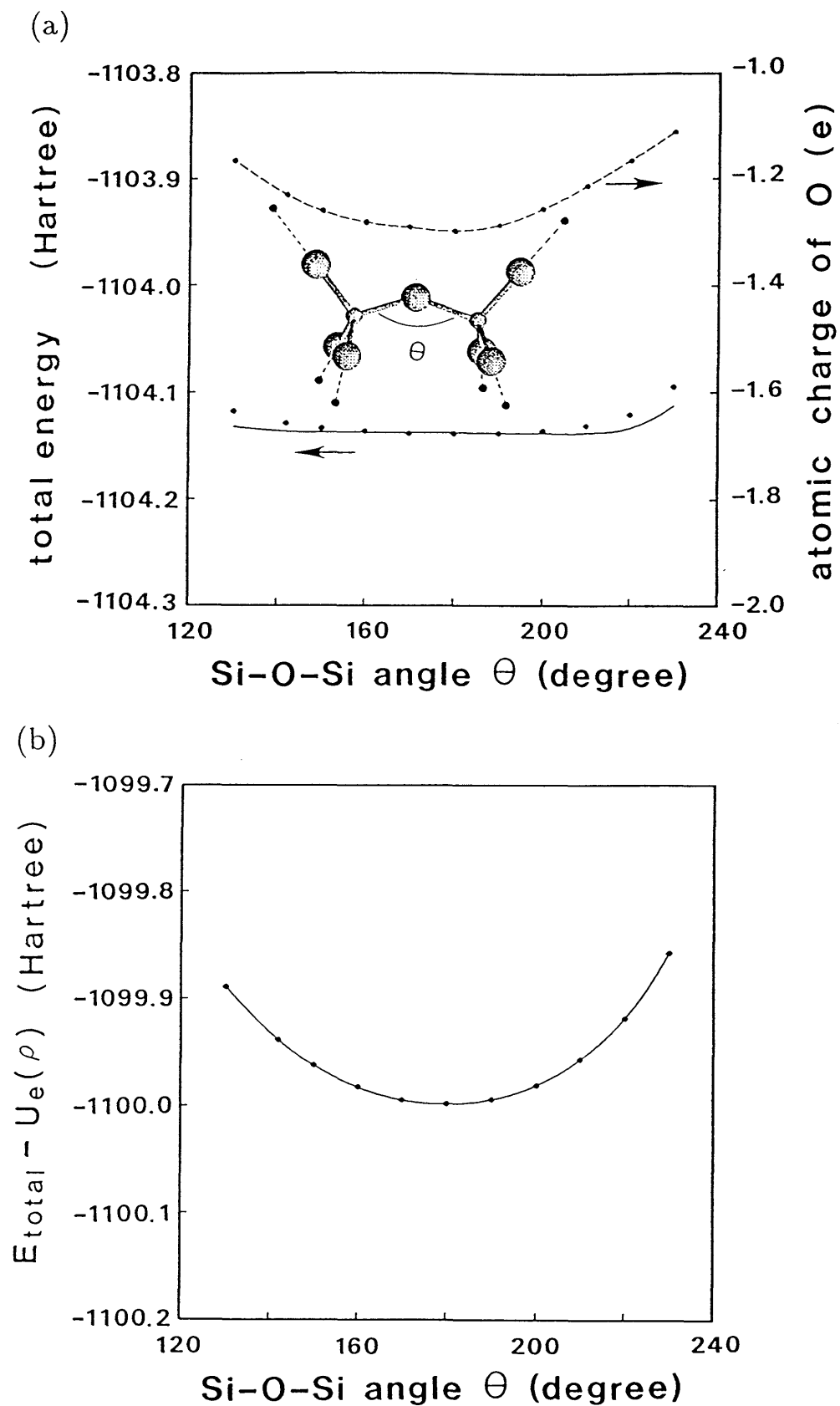


Fig.2-4 (a) Total energy and the Mulliken charge on the bridging oxygen atom for Si-O-Si bending of a $\text{Si}_2\text{O}_7^{6-}6e^+$ cluster. The full circles are the cluster calculation, the solid line is a fitted potential, and the dashed line is a guide to the eye. (b) The net potential energy surface calculated using electron-density distribution ρ .

charged cluster, tends to stretch ($\theta \sim 180^\circ$), the neutral cluster, which should mimic the real situation in the bulk, has almost θ -independent energy for a wide range of θ , because interactions among original and neutralizing charges tend to cancel. This is why the angle of adjacent SiO_4 tetrahedra can deviate from collinear with subtle energy differences in various polymorphs as we see in the following chapters. Since $d(\text{O-e}^+)$ and the Si-O distance are fixed here, this means the interaction between the positive charges and the third-neighbor oxygen atoms are very important for the Si-O-Si bending potential energy surface. Thus the potential energy surface by the present best-fit pairwise interatomic potentials (the solid line in Fig.2-4(a)) are also very flat even though the agreement with the HF-SCF data is not so good as in Fig.2-1, and this is why they can reproduce the Si-O-Si angle in all the polymorphs with considerable accuracy as shown later.

Finally, we investigate an octahedral SiO_6 cluster to check the applicability of our pairwise potential to stishovite, the densest known polymorph of silica, with six-fold Si-O coordination. In the total-energy-calculation, six point charges of $(8/6)e$ are put around the regular octahedron of SiO_6^{8-} with $d(\text{O-e}^+)=1.65\text{\AA}$. The potential-energy-surface of a_1 -deformation keeping O_h symmetry is shown in Fig.2-5 (full circles) as compared with the best-fit pairwise potential result (a solid line) where $\tilde{Q}_{\text{Si}}=2.4e$ ($Q_{\text{Si}}=2.4e$) and $\tilde{Q}_{\text{O}}=-(\tilde{Q}_{\text{Si}}+8e)/6$ ($Q_{\text{O}}=-1.2e$) are used to ensure charge neutrality. Although the equilibrium Si-O distance in the best-fit potential is about 0.06\AA larger than that in the cluster calculation, the curvature is very similar in these two results. In fact, if we set $\tilde{Q}_{\text{Si}}=3.2e$ in the long-range term in eq.(2.2), the best-fit potential energy surface (a dotted line in Fig.2-5) can well reproduce the calculated one. Thus our pairwise potential, which is determined for the four-fold coordination, is shown to reproduce the six-fold coordination surprisingly well. As we shall see, the potential indeed reproduces the structure and bulk modulus of six-fold coordinated stishovite.

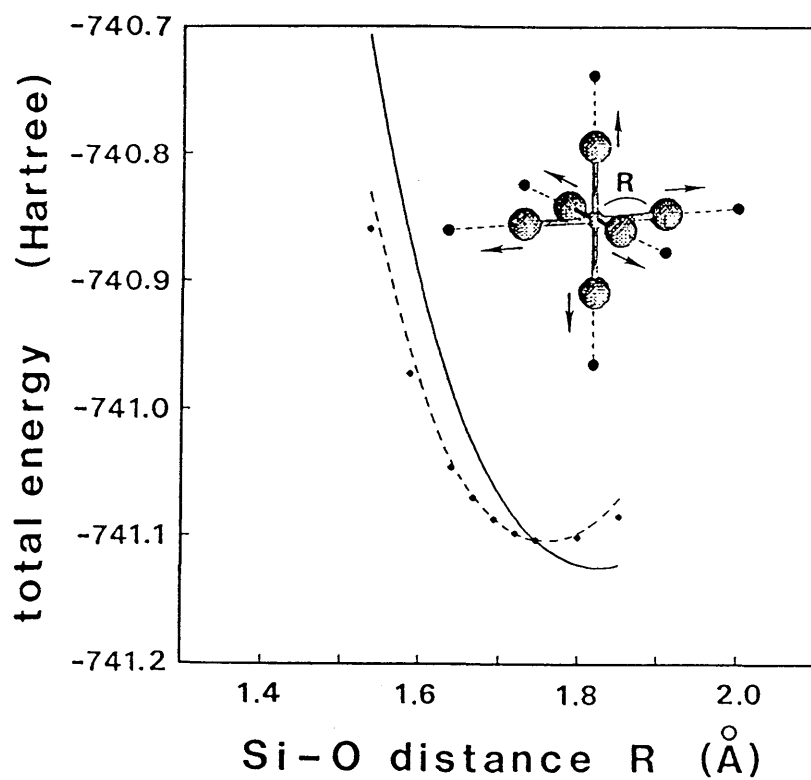


Fig.2-5 Total energy for O_h deformation of a SiO_6^{8-} cluster. The full circles are the cluster calculation, the solid line is a potential fitted for SiO_4 cluster, and the dashed line is obtained using $\Delta n=0.8$ (see text).

Section 2.5. Summary and discussion

We have shown that the potential-energy-surfaces for three deformation modes of the cluster, including the O-Si-O bond-angle deformation, can be reproduced using only pairwise interatomic potentials. Although this does not imply that silica is a fully ionic material without covalent character, it is expected that the structural properties of silica can also be reproduced by the pairwise potentials.

Since the cluster method is a finite-size calculation, there are naturally several empirical factors in the approach. The most obvious one is the employment of the SiO_4 cluster with neutralizing charges. It is an empirical fact that the SiO_4 tetrahedron is a basic unit in silica, and the position of additional charges has also some ambiguity. We could have also employed other functional form for the potential than the Gilbert-Ida form (eq.(2.1)). In this form, a $1/r$ term appears, which could be replaced with, say, a screened Coulomb form, or deleted altogether in place of some three-body interaction. There are also some technical details of the many-body calculation. Rigorously speaking, for instance, the potential energy surface changes for different choice of gaussian basis functions. As for the best-fit procedure, the non-linear least-square method gives several candidates for the best-fit parameters. As mentioned, we have selected the one which reproduces the low-quartz in the static simulation, which is also an empirical factor.

Aside from these factors, however, the present method is basically non-empirical. What we want to stress here is that we have proposed a new algorithm for obtaining, or predicting, the structure of materials: pair potentials are derived from small-cluster calculations to be fed into the MD calculation.

We have not included the potential energy surface of Si_2O_7 in the potential-parameter optimization because this would make the determination process too complicated. The smallest possible cluster, SiO_4 , will turn out to be good enough in the case of silica in the next chapter.

Finally it must be mentioned that, as the determination of the potential concentrates on the curvature of the potential-energy-surfaces, the cohesive energy of each polymorph is not necessarily reproduced accurately. This is a flaw of the cluster method and is a bottleneck in applying the potential to the simulation of melt system or structural transformation. This problem will be discussed in Chapter IV.

Chapter III. Molecular Dynamics Simulation

– Normal and High Pressure Condition

Section 3.1. Introduction: molecular dynamic simulation

In the last chapter, we extracted interatomic potentials of silica from the first-principles cluster calculation. In this chapter, we turn to the MD study of polymorphs of silica at room temperature using these interatomic potentials. The ability of these potentials to reproduce the dynamical stability of polymorphs is tested by the MD simulation. The simulated polymorphs are, mainly, low-quartz, low-cristobalite, coesite and stishovite, that is, virtually all the natural polymorphs of silica so far known (see Section 1.3 as for tridymite): these polymorphs correspond to different pressure-temperature regimes but can also exist at normal pressure and temperature as metastable states. Our aim is to answer the questions: (1)whether the interatomic potential derived from the cluster calculation is applicable to the bulk crystals, (2)whether various physical properties of the polymorphs are reproduced by the same interatomic potentials, and (3)whether pair-potential approximation is valid for silica, which has some degree of covalency. The test will also serve to check some empirical factors involved in the determined potential (Section 2.5).

Before reporting the MD results, we will briefly introduce the MD method in this section.

In its most primitive version, the MD method is simply a numerical integration of Newton's equations of motion in $3N$ dimension, where N is the number of particles in the system. The equations of motion are derived from the classical Hamiltonian,

$$H = \sum_i (1/2m_i) \mathbf{p}_i^2 + \Phi(\mathbf{r}_1, \dots, \mathbf{r}_N), \quad (3.1)$$

where \mathbf{r}_i (\mathbf{p}_i) is the position (momentum) of the i -th particle and Φ is the

potential energy of the system which is expressed by the summation of interatomic potentials between all the particle-pairs as $\Phi = \sum_{\text{pair}} \phi_{ij}$ within pair-potential approximation. Periodic boundary condition is usually imposed on the finite system (basic cell) in the simulation of bulk system. The temperature of the system is determined by the averaged kinetic energy of the particles by the relation $\langle \mathbf{p}_i^2 \rangle / (2m_i) = 3kT/2$, where k is the Boltzmann constant. The pressure is given by the virial theorem as

$$\begin{aligned} P &= NkT/V - (1/3V) \sum_i \mathbf{r}_i \cdot (\partial \Phi / \partial \mathbf{r}_i) \\ &= NkT/V - (1/3V) \sum_{\text{pair}} \mathbf{r}_{ij} \cdot (\partial \phi_{ij} / \partial \mathbf{r}_{ij}), \end{aligned} \quad (3.2)$$

where V is the volume of the system, $\mathbf{r}_{ij} = \mathbf{r}_i - \mathbf{r}_j$, and the second expression in the right-hand-side is for pairwise interatomic potentials. The first expression is written for a system with boundaries: this is seen from the fact that the second term in the right-hand side vanishes in the equilibrium in the interior of the system, while the interactions with walls give a nonzero value.

Each particle is then moved in Newtonian dynamics, starting from random velocities and initial (random or crystalline) positions, until equilibrium is achieved. The pressure and temperature can be kept equal to the specified values by scaling the size of the basic cell and the kinetic energy, respectively. This corresponds to the micro-canonical ensemble when the scaling is not performed.

Since the pressure as defined above in a crystalline system can be highly anisotropic, it is inappropriate to use only the hydrostatic pressure defined by eq.(3.2) in a simulation of a crystal. In this case, the basic cell has to be anisotropically scaled so as to make $P_x = P_y = P_z$, where P_μ is the μ -th diagonal component of the stress. Here

$$P_x = NkT_x/V - (1/V) \sum_{\text{pair}} r_{ij,x} (\partial \phi_{ij} / \partial r_{ij,x}), \quad (3.3)$$

where T_x stands for the the x-component of temperature (temperature obtained from x-component of particle velocities), and $r_{ij,x}$ means the x-component of \mathbf{r}_{ij} . This scaling corresponds to the transformation of the basic cell with the orthorhombic symmetry preserved (Matsui and Kawamura, 1987).

The orthorhombic symmetry may often be too strong a restriction. The constant-pressure algorithm due to Parrinello and Rahman (1981) allows the unit cell angles to change, so that not only monoclinic or triclinic crystals can be treated but also structural phase transitions can be simulated in this method. The equations of motion in this approach are derived from the following Hamiltonian:

$$\begin{aligned}
H &= \sum_i (1/2m_i) {}^t\mathbf{p}_i \mathbf{G}^{-1} \mathbf{p}_i + \Phi(\mathbf{h}\mathbf{q}) \\
&\quad + (1/2M) \text{Tr}({}^t\mathbf{p}_h \mathbf{p}_h) + P_{\text{ex}} |\mathbf{h}|, \\
\mathbf{q}'_i &= \mathbf{h}\mathbf{q}_i, \\
\mathbf{p}'_i &= {}^t\mathbf{h}^{-1} \mathbf{p}_i, \\
\mathbf{G} &= {}^t\mathbf{h} \mathbf{h}, \\
|\mathbf{h}| &= \det(\mathbf{h}) = V,
\end{aligned} \tag{3.4}$$

where \mathbf{h} is a matrix whose columns are, in order, the component of basic cell vector \mathbf{a} , \mathbf{b} and \mathbf{c} that span the edges of the basic cell, \mathbf{p}_h is a momentum conjugate to \mathbf{h} , P_{ex} is the external hydrostatic pressure, and \mathbf{q}_i and \mathbf{p}_i are related with real positional and momentum column-vectors $(\mathbf{q}'_i, \mathbf{p}'_i)$ through the scaling matrix \mathbf{h} . The basic-cell volume V is explicitly included as a dynamical variable and the corresponding kinetic energy is introduced with a fictitious mass M . In equilibrium at temperature T , $9kT/2$ is contributed by these degrees of freedom and $3NkT/2$ by the original kinetic terms. Therefore the constant of motion H is nothing but the enthalpy to an accuracy of $3/N$. The canonical variables are \mathbf{q}_i , \mathbf{p}_i , \mathbf{h} , and \mathbf{p}_h , which satisfy the canonical equations derived from the Hamiltonian. As the final equations of motion for \mathbf{q}_i and \mathbf{h} , we get

$$\begin{aligned}
\ddot{\mathbf{q}}_i &= - (1/m_i) \sum_j (1/r_{ij}) (\partial \phi_{ij} / \partial \mathbf{r}_{ij}) (\mathbf{q}_i - \mathbf{q}_j) - \mathbf{G}^{-1} \dot{\mathbf{G}} \dot{\mathbf{q}}_i, \\
M \ddot{\mathbf{h}} &= (\pi - P_{\text{ex}}) \mathbf{h}^{-1} \mathbf{V} \\
V \pi &= \sum_i m_i (\mathbf{h} \dot{\mathbf{q}}_i) (\mathbf{h} \dot{\mathbf{q}}_i) - \sum_{\text{pair}} (1/r_{ij}) (\partial \phi_{ij} / \partial \mathbf{r}_{ij}) (\mathbf{h} \mathbf{q}_{ij}) (\mathbf{h} \mathbf{q}_{ij}).
\end{aligned} \tag{3.5}$$

As seen from the second and the third equations, the shape of the basic cell changes so that the internal stress balances with the external pressure. The ensemble obtained with this algorithm is called (P,H,N) ensemble, which stands for the constant P_{ex} , H (enthalpy) and particle number.

The constant temperature algorithm to obtain canonical ensemble was derived by Hoover et al. (1982), Evans (1983), and later refined by Nosé (1984). Nosé's method, or the revised version by Hoover (1985), introduces some fictitious variable to scale the time and is called the extended system method. The Hamiltonian is postulated to have the form

$$\begin{aligned}
H &= \sum_i (1/2m_i) \mathbf{p}_i^2 / s^2 + \Phi(\mathbf{q}) \\
&\quad + p_s^2 / (2Q) + gkT \log s,
\end{aligned} \tag{3.6a}$$

where Q is another fictitious mass for the kinetic energy of the time-scaling variable s . Canonical variables, \mathbf{q}_i , \mathbf{p}_i , s , p_s and t are related with the real variables (primed variables) as

$$\begin{aligned}
\mathbf{q}_i &= \mathbf{q}_i', \quad \mathbf{p}_i / s = \mathbf{p}_i', \\
s &= s', \quad p_s / s = p_s', \\
\int^t dt / s &= t'.
\end{aligned} \tag{3.6b}$$

The equations of motion for real variables obtained from the Hamiltonian are

$$\begin{aligned}
\ddot{\mathbf{q}}_i' &= - (1/m_i) \partial \Phi / \partial \mathbf{q}_i' - \zeta \dot{\mathbf{q}}_i', \\
\dot{\zeta} &= (1/Q) [\sum_i m_i \dot{\mathbf{q}}_i'^2 - gkT],
\end{aligned} \tag{3.7}$$

where ζ introduced by Hoover (1985) is related with s as

$$\dot{s}'/s' = \zeta. \quad (3.8)$$

If g (the factor appearing with $kT \log s$ in eq.(3.6a)) is set equal to $3N$, it can be easily shown that \mathbf{p}_i' and \mathbf{q}_i' follows the canonical ensemble (Nosé, 1984; Hoover, 1985).

In the present study, we have used Parrinello and Rahmann's constant pressure algorithm combined with the constant temperature algorithm by Nosé. Numerical integration was performed using Verlet's algorithm (Verlet, 1967) with the time step of 2fsec. The mass (M) for the volume term in eq.(3.5) is set equal to 50 g/mol and that for the temperature term in eq.(3.7) (Q) to $2\text{kJ/mol} \cdot (\text{psec})^2$. The Ewald sum method is used for evaluating the long-range Coulomb interactions. The $1/r^6$ term is calculated by direct summation within a certain cut-off length ($\sim 7\text{\AA}$), while the interaction beyond the cutoff length was integrated by continuum approximation.

As we want to check the dynamical stability of crystal structures, all the atoms are given random velocities starting from the ideal positions of a crystal structure determined by experiments: the crystallization to each polymorph from random atomic positions cannot be expected within a short time period of the simulation. If the interatomic potentials employed are inappropriate, the initial crystal configuration disintegrates immediately or after retaining the structure with thermal fluctuations for some period in some cases. We have tried several sizes of basic cells, in which the largest number of atoms in the basic cell of each polymorphs is 576 (containing 64 unit cells), 576(48), 768(16) and 576(96) for low-quartz, low-cristobalite, coesite and stishovite, respectively.

Section 3.2. Simulated polymorphs of silica

In this section we report the MD results for the polymorphs of silica at room temperature and normal (ambient) pressure. The MD results for high-pressure compression of each polymorphs are also shown and compared with experiments.

First of all, the MD results with the pairwise interatomic potentials obtained in Chapter II show that the four polymorphs (low-quartz, low-cristobalite, coesite, stishovite) are dynamically stable despite the fact that these polymorphs have large differences in their topology and density: the result shows that the time-averaged configuration of each polymorphs preserves its space group symmetry and that the obtained density agrees with the experimental result within 10%. The structural parameters are summarized in Table 3-1 together with the atomic configuration in Fig.3-1. More detailed information on the positional parameters of each phase is listed in Appendix A.

We have also performed MD calculations under high pressure. The volume of each polymorph normalized by the zero-pressure volume V_0 is shown in Fig.3-2 as a function of pressure, which agrees with experimental results very well up to the highest pressure studied in the experiments. As is done in experimental analysis, we estimate the bulk modulus K_0 by fitting the pressure-volume results to a Birch-Murnaghan equation of state (see Ida and Mizutani, 1978):

$$\begin{aligned} P &= (3/2)K_0(y^{-7/3} - y^{-5/3}) [1 - (3/4)(4-K_0')(y^{-2/3}-1) + (\eta/2)(y^{-2/3}-1)^2] , \\ y &= V/V_0, \\ \eta &= (3/4)(K_0K_0''+K_0'^2-7K_0'+143/9). \end{aligned} \tag{3.9}$$

The obtained bulk moduli (Table 3-1) are in good agreement with the experimental results even for stishovite with six-fold silicon atoms as well as for other polymorphs. It should be noted that our MD simulation (Tsuneyuki, Tsukada, Aoki and Matsui, 1988) on the bulk modulus of low-cristobalite

Table 3-1 Structural parameters obtained here by MD simulations as compared with experimental results (or results by the FLAPW band calculation) for various polymorphs of silica. Estimated standard errors in observed (Obs.) data and thermal fluctuations in MD data are given in parentheses in units of the last decimal place stated.

	low-quartz		low-cristobalite		coesite	
	Obs. ^a	This work	Obs. ^b	This work	Obs. ^d	This work
Space Group	$P3_121$	$P3_121$	$P4_12_12$	$P4_12_12$	$C2/c$	$C2/c$
Z	3	3	4	4	16	16
a (Å)	4.916(1)	5.018(12)	4.979	4.991(17)	7.1356(3)	7.218(25)
b (Å)	4.916(1)	5.018(11)	4.979	4.991(17)	12.3692(8)	12.760(27)
c (Å)	5.4054(4)	5.549(11)	6.950	6.657(31)	7.1736(3)	7.417(25)
α	90°	90.0(2)°	90°	90.0(2)°	90°	90.0(2)°
β	90°	90.0(2)°	90°	90.0(1)°	120.34(2)°	120.6(5)°
γ	120°	120.0(2)°	90°	90.0(2)°	90°	90.0(2)°
Density (g/cm ³)	2.6458(7)	2.474(8)	2.316	2.406(22)	2.9213(3)	2.716(8)
K ₀ (GPa)	38(3)	33.7(1)	18 ^c	17.4(7)	96(3)	108(2)
K ₀ '	6.0(2)	5.05(3)	—	9.5(1.7)	8.4(1.9)	2.6(2.3)
Energy (kcal/mol)		-1235.1		-1231.1		-1239.7
Si-O (Å)	1.605(1)	1.627	1.605(2)	1.644	1.5945(4)	1.609
	1.614(1)	1.640	1.613(2)	1.625	— 1.619(1)	— 1.655
Si-O-Si	143.73(7)°	147.3°	146.4(1)°	142.7°	180.°	180.0°
					137.36(9)°	143.9°
					— 149.64(9)°	— 155.3°

^aLevien et al. (1980). ^bPeacor (1973).

^cTsuchida et al. (1989). ^dLevien et al. (1981).

	stishovite		$Pa\bar{3}$ silica	
	Obs. ^e	This work	FLAPW ^g	This work
Space Group	$P4_2/mnm$	$P4_2/mnm$	$Pa\bar{3}$	$Pa\bar{3}$
Z	2	2	4	4
a (Å)	4.1773(1)	4.271(6)	4.47	4.563(6)
b (Å)	4.1773(1)	4.271(5)	4.47	4.563(7)
c (Å)	2.6655(1)	2.753(4)	4.47	4.563(5)
α	90°	90.0(1)°	90°	90.0(1)°
β	90°	90.0(2)°	90°	90.0(1)°
γ	90°	90.0(1)°	90°	90.0(2)°
Density (g/cm ³)	4.2902	3.974(8)	4.46	4.201(6)
K ₀ (GPa)	296(5) ^f	312(2)	335	328.4(2)
K ₀ '	4.0(1.4)	5.4(5)	1.60	4.54(1)
Energy (kcal/mol)		-1234.0		-1206.9
Si-O (Å)	1.7572(1)	1.813	1.827	1.863
	1.8087(2)	1.840		
Si-O-Si	98.66(1)°	98.8°	119.8°	120.0°
	130.67(1)°	130.6°		

^eHill et al. (1983). ^fSato (1977). ^gTheoretical result by Park et al. (1988).

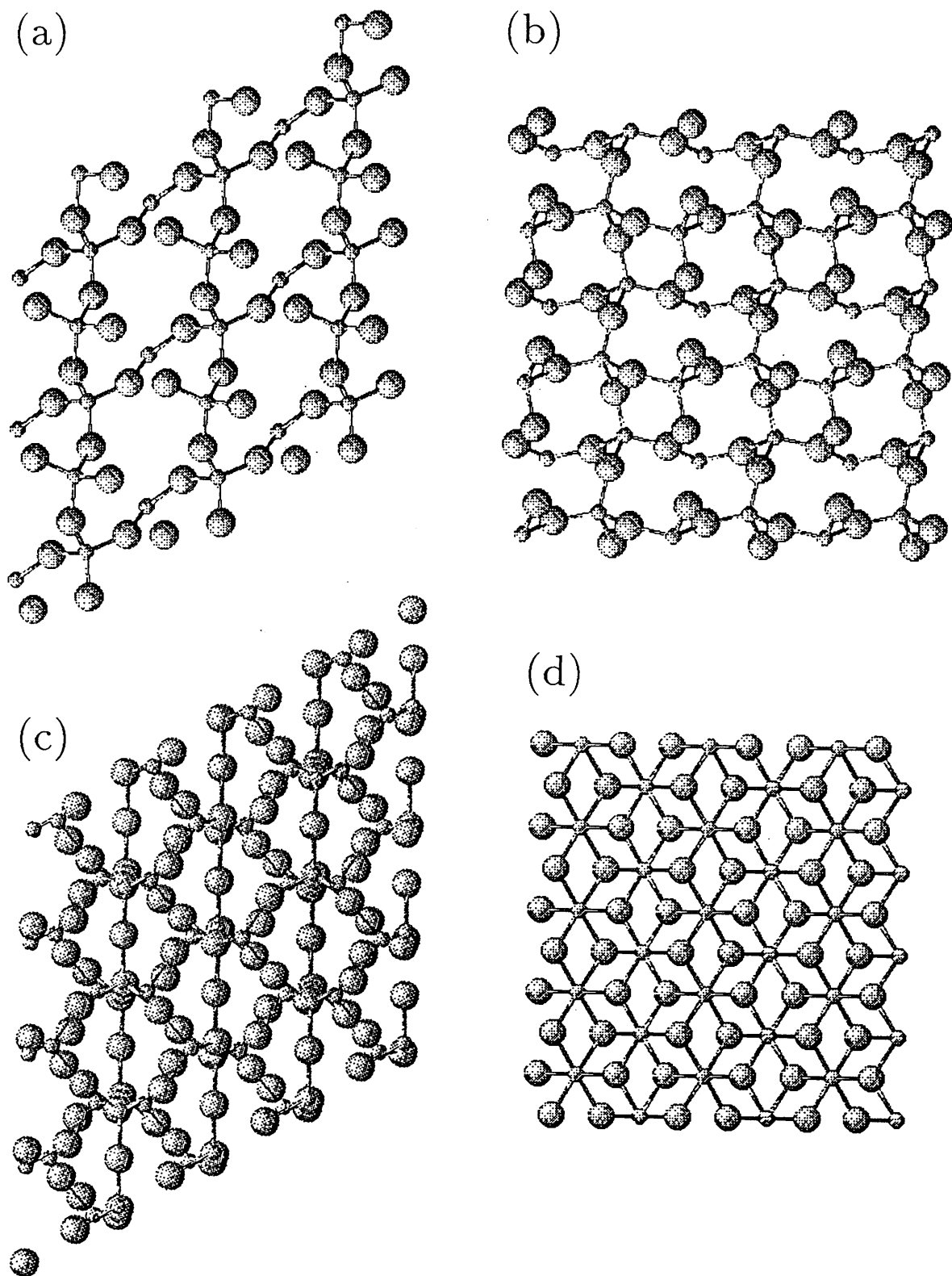


Fig.3-1 Atomic configurations (averaged over time steps) obtained in the MD study for (a) low-quartz, (b) low-cristobalite, (c) coesite, and (d) stishovite. Note the elementary (a) three-fold screw axes, (b) six-membered ring, (c) four-membered ring, and (d) SiO₆ coordination.

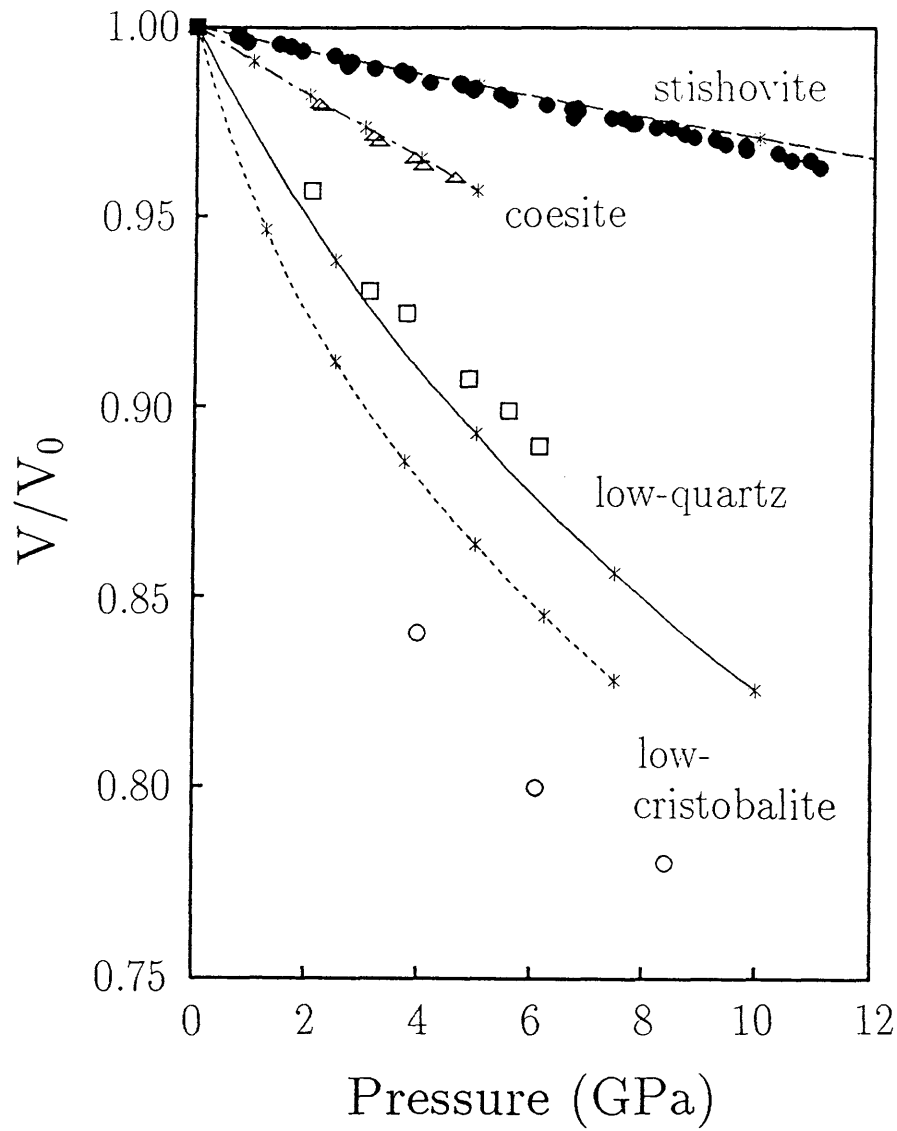


Fig.3-2 Pressure-volume relation for low quartz (—), low-cristobalite (-----), coesite (-.-.-.-), and stishovite (----) obtained by the MD simulation. Experimental data are shown with □ (Levien et al., 1980), ○ (Tsuchida et al., 1989), Δ (Levien et al., 1981), and ● (Sato, 1977), respectively.

preceded the experimental measurement. Tsuchida and Yagi measured the bulk modulus of low-cristobalite very recently (1989) and obtained quantitatively good agreement with our prediction (Table 3-1).

Anisotropic pressure-dependence of the unit cell dimension also agrees with the experimental result as shown in Fig.3-3(a)–(d). In contrast with the present results, the static simulation by Lasaga and Gibbs (1987) with use of the potential which is covalent (three-body) but extends only to the first-neighbor atoms results in reverse anisotropy for low-quartz (*i.e.*, the c-axis is softer than the a-axis). This provides another indication that longer-range interactions beyond the first-neighbor atoms are important. The dependence of the Si-O-Si bridging angle in low-quartz on pressure or molar volume is shown in Fig.3-4(a) and (b), respectively. The calculated result (full circles) agrees with experimental results (open circles), which supports the reliability of our interatomic potentials including the equilibrium Si-O-Si angle. More specifically, the pressure-dependence of positional parameters (Appendix A) also agree well with experimental results.

Using the pairwise interatomic potentials and the structural parameters obtained by the MD simulation at room temperature, we have calculated the dynamical matrix of low-quartz to obtain the phonon dispersion as shown in Fig.3-5(a). Although the pairwise potentials do not include the effect of electron polarization as we discussed in Section 2.3, the simulated phonon dispersion of low-quartz agrees rather well with that obtained by experiments (Fig.3-5(b)) (Dorner, Grimm, and Rzany, 1980). Thermal expansion of quartz and the softening of some phonon modes will be discussed in Chapter IV.

Besides these four polymorphs, which cover virtually all the natural polymorphs of silica so far known, we have tested the low-tridymite, which has not been fully established as a polymorph of pure silica (see, e.g., Holmquist, 1961). As a result, we obtained an equilibrium structure that preserves the exceptionally low symmetry of space group Cc , although the structure is different from that in the latest report (Kato and Nukui, 1976; Baur, 1977).

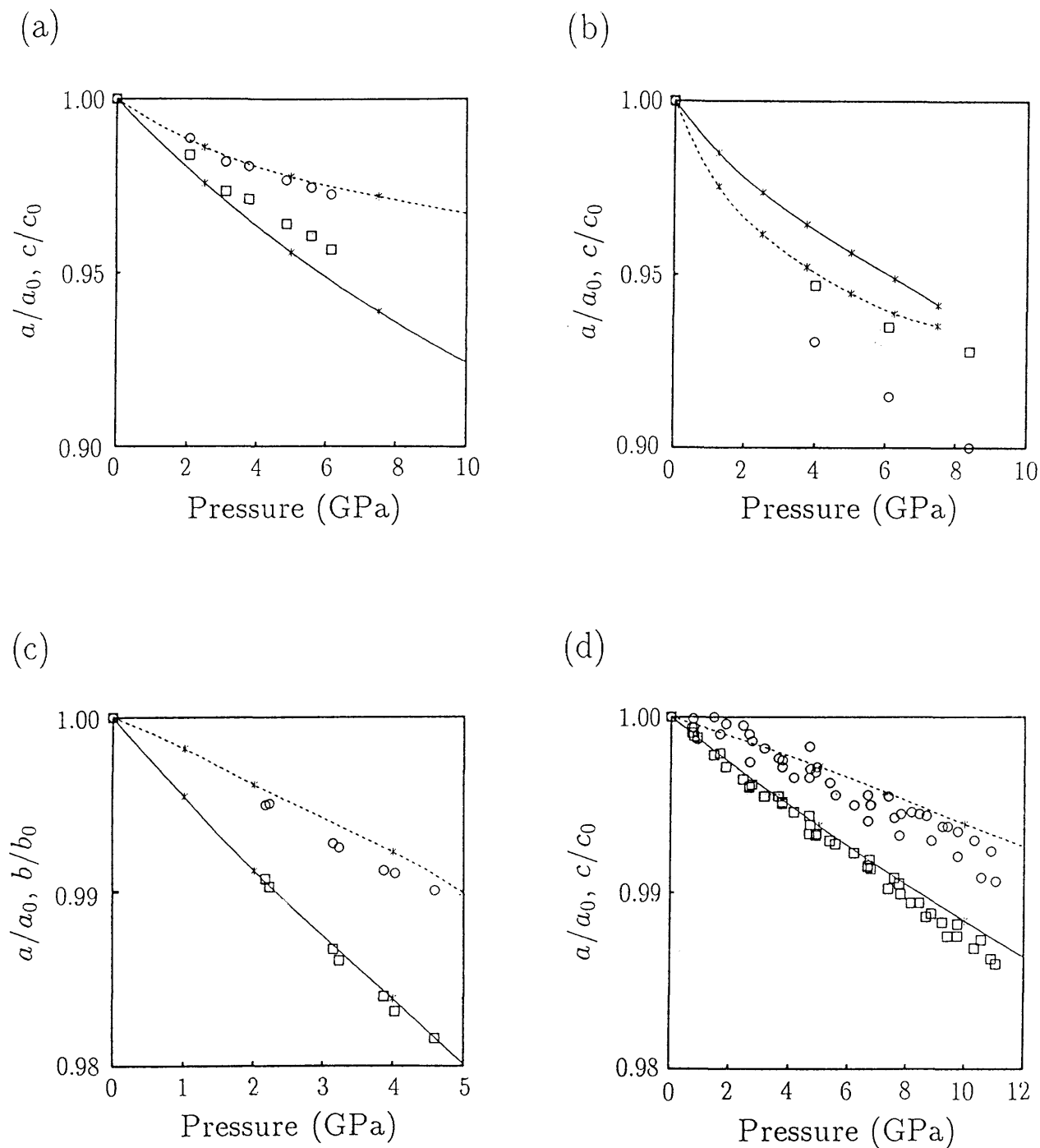


Fig.3-3 Pressure dependences of unit-cell axes of (a) low-quartz, (b) low-cristobalite, (c) coesite and (d) stishovite. MD result for the a-axis are shown with solid lines, and another axis (c or b) with dotted lines. Experimental data (see the caption of Fig.3-2) are also shown with open squares (a-axis) and open circles (c- or b-axis).

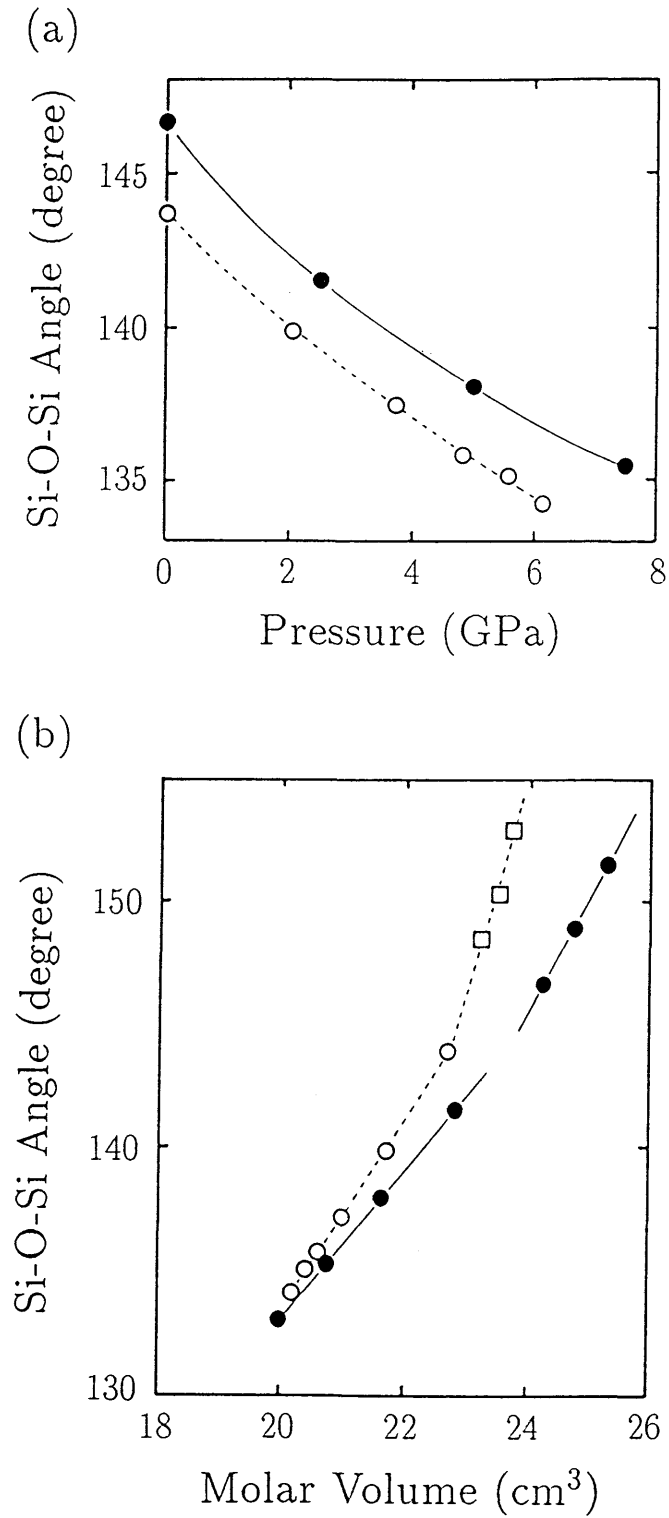


Fig.3-4 (a) Pressure dependence of the Si-O-Si bridging angle of quartz at room temperature. MD results are shown with full circles and the experimental data (Levien et al., 1980) are shown with open circles. (b) Molar volume dependence of the Si-O-Si bridging angle of quartz. MD results are shown with full circles and the experimental data are shown with open circles (compression at room temperature by Levien et al., 1980) and open squares (heating at ambient pressure by Young, 1962).

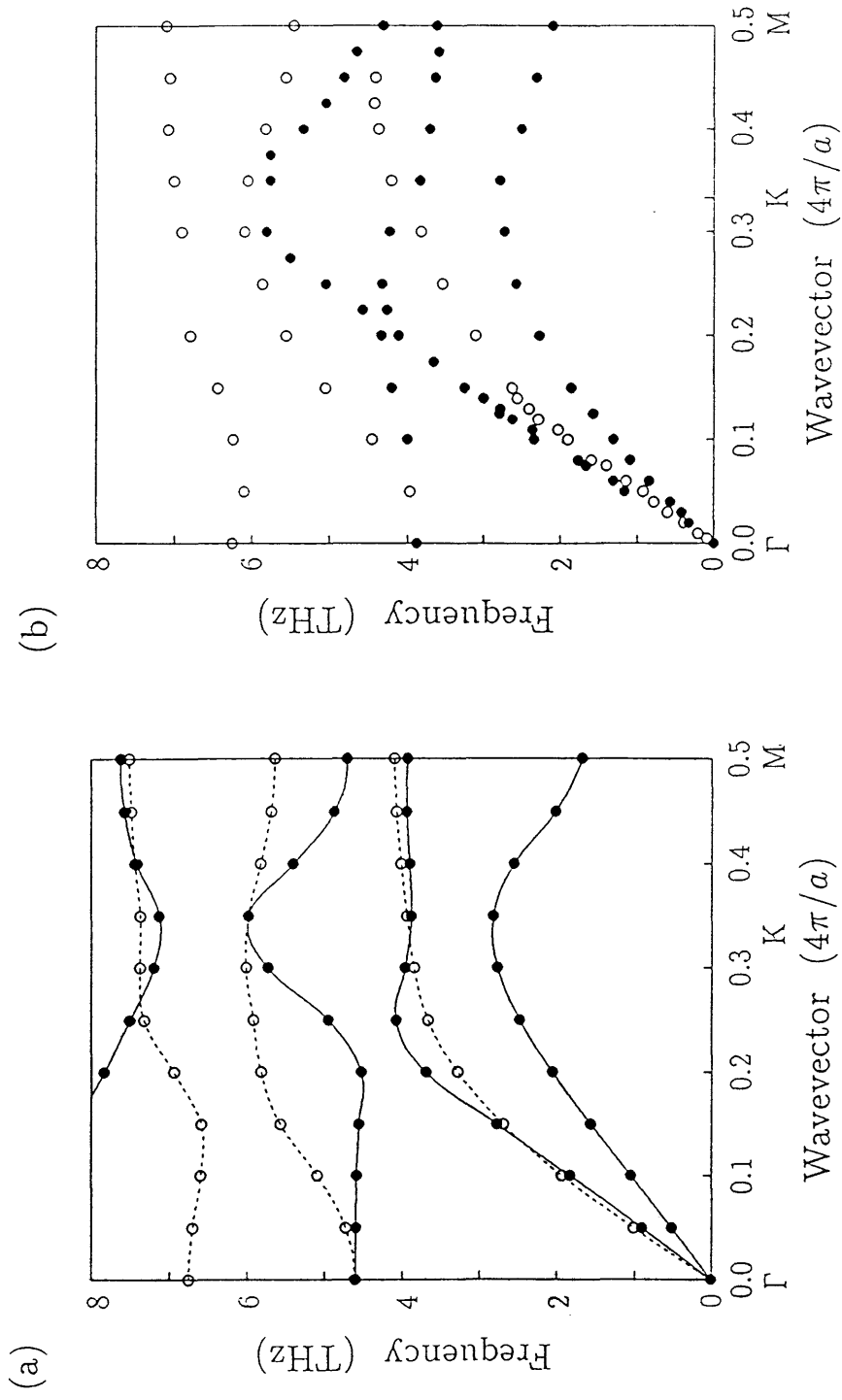


Fig.3-5 Phonon dispersions of quartz at room temperature: (a) calculated results with use of the present pair potentials and (b) experimental data by Dorner et al. (1980). Full (open) circles and full (dotted) lines represent antisymmetric (symmetric) modes.

Since the unit cell of low-tridymite is reported to be very large (48 SiO₂ units) and complicated, further investigation would be necessary for both MD and experiment.

We also performed the simulation of $Pa\bar{3}$ silica (Y. Matsui and M. Matsui, 1988), which is theoretically predicted to be ~6% denser than stishovite at ambient pressure and thermodynamically more stable above 60GPa (Park, Terakura and Matsui, 1988). This phase could have great geophysical implications, because MgSiO₃-perovskite, which is widely accepted as the major constituent within the Earth's deep interior, may be less stable than the assemblage of $Pa\bar{3}$ silica plus MgO at high pressures if the $Pa\bar{3}$ phase really exists. The simulated $Pa\bar{3}$ phase (Fig.3-6 and Table 3-1) is indeed stable at room temperature and normal pressure. It has a density 5.5% higher than that of simulated stishovite and the bulk modulus similar to that of simulated stishovite. These results agree very well with the prediction of a theoretical calculation with the full-potential linear augmented plane wave (FLAPW) method (Park, Terakura and Y. Matsui, 1988). As for the total-energy difference between $Pa\bar{3}$ and stishovite, $Pa\bar{3}$ silica is less stable than stishovite by 10kcal/mol at 0GPa according to the FLAPW calculation, while the energy difference is about 28kcal/mol with our interatomic potential.

As mentioned in Chapter II, the interatomic potential approach does not necessarily give accurate total energy differences. The molar energy of the polymorphs are listed in Table 3-1. The energy difference between low-quartz and stishovite is smaller than the experimental result by about 9kcal/mol (Holm, Kleppa and Westrum, 1967), and coesite is more stable than low-quartz in contrast with the experimental results that coesite is less stable by 0.45kcal/mol (Holm et al., 1967). Therefore the P-T phase diagram of silica is not reproduced with our interatomic potentials. Since we have concentrated on considering force constants (curvature of the deformation potential) but not the binding energy itself, the pair potential does not necessarily give the correct absolute value for the total energy. Thus we must be careful in simulating the phase transitions

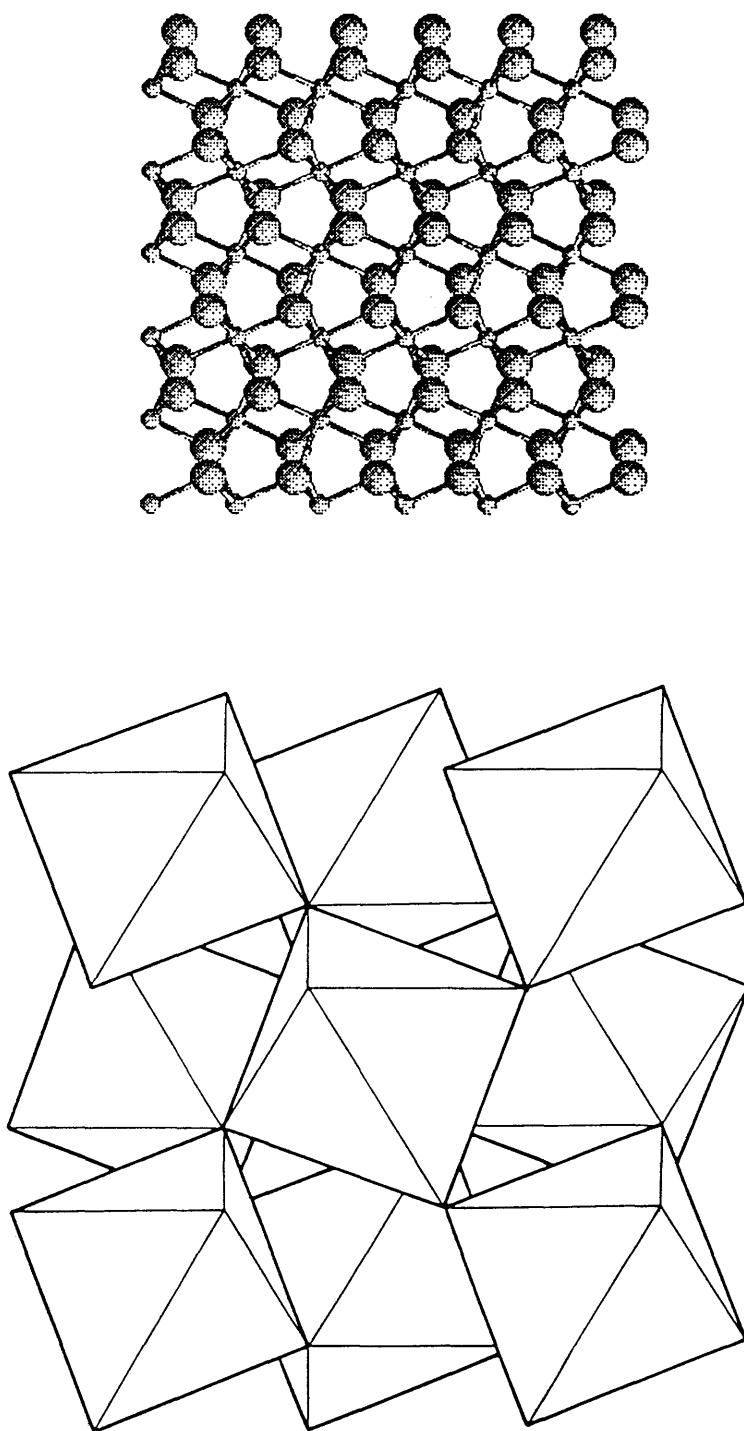


Fig.3-6 Atomic configurations (averaged over time steps) obtained in the MD study for $Pa\bar{3}$ -silica. The configuration of SiO_6 octahedra are illustrated in the lower panel.

between topologically different phases, which will be discussed again in chapter V in the context of pressure-induced phase transitions.

Section 3.3. Summary and discussion

We have performed MD simulations of silica with the pairwise interatomic potentials derived from the first-principles calculation. The MD results reproduce the structures and bulk moduli of virtually all the known polymorphs of silica.

Although both covalent and ionic characters should be present in silica, one would consider that tetrahedral units indicate dominant covalent bonding. The present result shows that dynamical stability of silica can nevertheless be reproduced by the pairwise potential which is extracted from a small cluster. Broadly speaking, the fact that different polymorphs are reproduced may be attributed to the strong bonds between silicon and the nearest oxygen atoms. The message here is that, once SiO_4 or SiO_6 local units are formed, the crystal structure and elastic property of the polymorphs of silica is determined by the space filling of the local units, or rather oxygen atoms. Namely, although silica assumes open framework structures, we can regard that the manner in which SiO_4 units are connected (Si-O-Si angles, etc.) is primarily determined by the packing of oxygen atoms (geometrical hindrance of nearby oxygens, etc.), as contrasted to some views like Lasaga et al. (1987) in which some directional three-body forces are regarded to be essential. Still it is quite remarkable that several polymorphs are reproduced with the same pairwise potentials, since the differences in the tilt angles between SiO_4 (or SiO_6) units are crucial in these polymorphs. This is precisely why an accurate determination of potentials is required.

Due to the intrinsic flaw of the cluster calculation, our interatomic potentials cannot reproduce the correct differences in the total energy of the phases. Thus the present method, which is quite adequate for the study of

structural stability, may be coupled to total-energy methods like band calculations to give a more accurate description of polymorphs including the thermodynamics of phase transitions.

Chapter IV. The α - β Structural Phase Transition of Quartz

Section 4.1. Introduction

Thermally induced structural phase transition of crystals is one of the best playing grounds for the molecular dynamics (MD) simulation, since large fluctuations in the atomic motion inherent in the critical phenomena can be treated as compared with the lattice dynamics method. The MD simulation has been applied by Schneider and Stoll (1974, 1976, 1978) to a simplified model to investigate order-disorder and displacive phase transitions. Kerr and Bishop (1986) also studied the dynamics of a phase transition in a two-dimensional model. In these studies, however, thermal expansion of the system is completely neglected, whereas the interatomic forces are in fact sensitive to the density of system. Recently MD simulation was used to determine the structures above and below the phase transition for Rb_2CaCl_4 with *ab initio* interatomic potentials by Billesbach et al. (1988), although the system-size (of 112 atoms) studied is rather small to obtain a clear picture of the transition, and no experimental results have been reported on this material either. A similar kind of simulation of RbCaF_3 is also reported by Nosé and Klein (1989).

In this chapter, we report an MD study of the structural transition of quartz using the first-principles interatomic potential obtained in chapter II. There is a long history of experimental study on the phase transition in quartz (Young, 1962; Scott, 1968; Axe and Shirane, 1970; Dolino, 1988). At room temperature, quartz assumes a low-temperature phase of space group $P3_121$, which is called low-quartz or α -quartz, while it transforms into a high-temperature phase of space group $P6_222$ (high-quartz or β -quartz) when it is heated above $T_C=846\text{K}$. The soft mode of the phase transition was first detected by Raman scattering below T_C (Scott, 1968) and by inelastic neutron scattering above T_C (Axe and Shirane, 1970). There has been a controversy as to the structure of β -quartz: the question is whether the atoms in the β -phase vibrate around the idealized β position (Young, 1962) or fluctuate between the α_1 and

α_2 phases (see below) (Tendeloo, Landuyt and Amelinckx, 1976; Wright and Lehmann, 1981). The transition is particularly suitable for the MD study, since (i) this is not a ferroelectric transition, so that we need not take account of the dielectric polarization of electrons in a first approximation, and (ii) the transition temperature is much higher than the Debye temperature (470K), so that the classical dynamics is applicable. To establish the high-temperature phase is also important for characterizing the incommensurate phase (Dolino, 1988), which is recently observed to occur in a narrow temperature range ($<2\text{K}$), although we do not discuss the incommensurate phase here, which would require a study with larger system-sizes.

We show that the phase transition is successfully reproduced at about 850K in the MD simulation. The transition is shown to have a peculiar dynamical character in that, although the probability distribution for atomic positions mimics displacive shift to the β -structure, and though the softening of phonon modes is confirmed by the lattice dynamics calculation, each unit cell in fact hops between the two equivalent α_1 and α_2 structures with a temperature-dependent correlation time. Thus the transition has characteristics of both displacive and order-disorder phase transitions.

Section 4.2. Molecular dynamics simulation of heating of quartz

The MD simulation is performed using the same formalism described in section 3-1. The number of atoms in the system mainly used is 432 (containing $4 \times 4 \times 3 = 48$ unit cells) while we also used 324 ($3 \times 4 \times 3$) or 576 ($4 \times 4 \times 4$) particle systems for comparison. Starting from the ideal crystal configuration of α -quartz and random velocities for atomic positions, we have obtained equilibrium configuration at 300K. Then the temperature of the system is gradually increased (by 200K at lower temperatures and by 10–50K near the critical temperature). Physical quantities are averaged over 12 psec (6000 MD steps)

after at least 4psec run for equilibration at each temperature.

Result for the equilibrium volume against temperature (open squares in Fig.4-1(a)) shows that, as the temperature is increased, the expansion coefficient abruptly changes at $T_C=850-900\text{K}$ and the thermal expansion remains almost zero above T_C . This is a clear-cut evidence for a phase transition and the behavior agrees with the experimental results (Clark Jr., 1966) also shown in the figure by a solid line, in which the expansion coefficient shows an abrupt change at $T_C = 846\text{K}$ when the system changes into β -quartz. The absolute value for the equilibrium density of the simulated α -quartz at 300K is 2.47g/cm^3 , which agrees within 7% with the experimental value (2.65g/cm^3). The anisotropy of the expansion coefficient is also reproduced as shown in Fig.4-1(b). The phase transition is experimentally shown to be first-order by the precise measurement of latent heat, although the volume expansion or heat capacity results are very similar to those of the second-order transition (Dolino, 1988). No appreciable hysteresis is observed either in the MD simulation around T_C .

The temperature dependence of the pair correlation function (PCF) for Si-Si, Si-O and O-O pairs is shown in Fig.4-2. The first peaks of the Si-O and O-O PCF's show thermal broadening, though their positions are almost independent of temperature. This means that the SiO_4 tetrahedra are quite rigid, which would provide some justification for the completely rigid model of Grimm and Dorner (1975). On the other hand, the other peaks shift to larger distances for $300\text{K} < T < T_C$ due to the stretching and/or rotation of the Si-O-Si bonds.

The character of the phase transition can be made clear if we look at the the order-parameter of the phase transition defined in the following way. The internal coordinates of atoms in α and β -quartz can be specified by the symmetry operation of the space group $P3_121$ on a representative position of silicon at $\mathbf{r}=(u, 0, 0)$ and an oxygen at $\mathbf{r}=(x, y, z)$ in the hexagonal unit cell with three silicon atoms and six oxygen atoms. Given u, x, y , and z , all the atomic positions are specified as

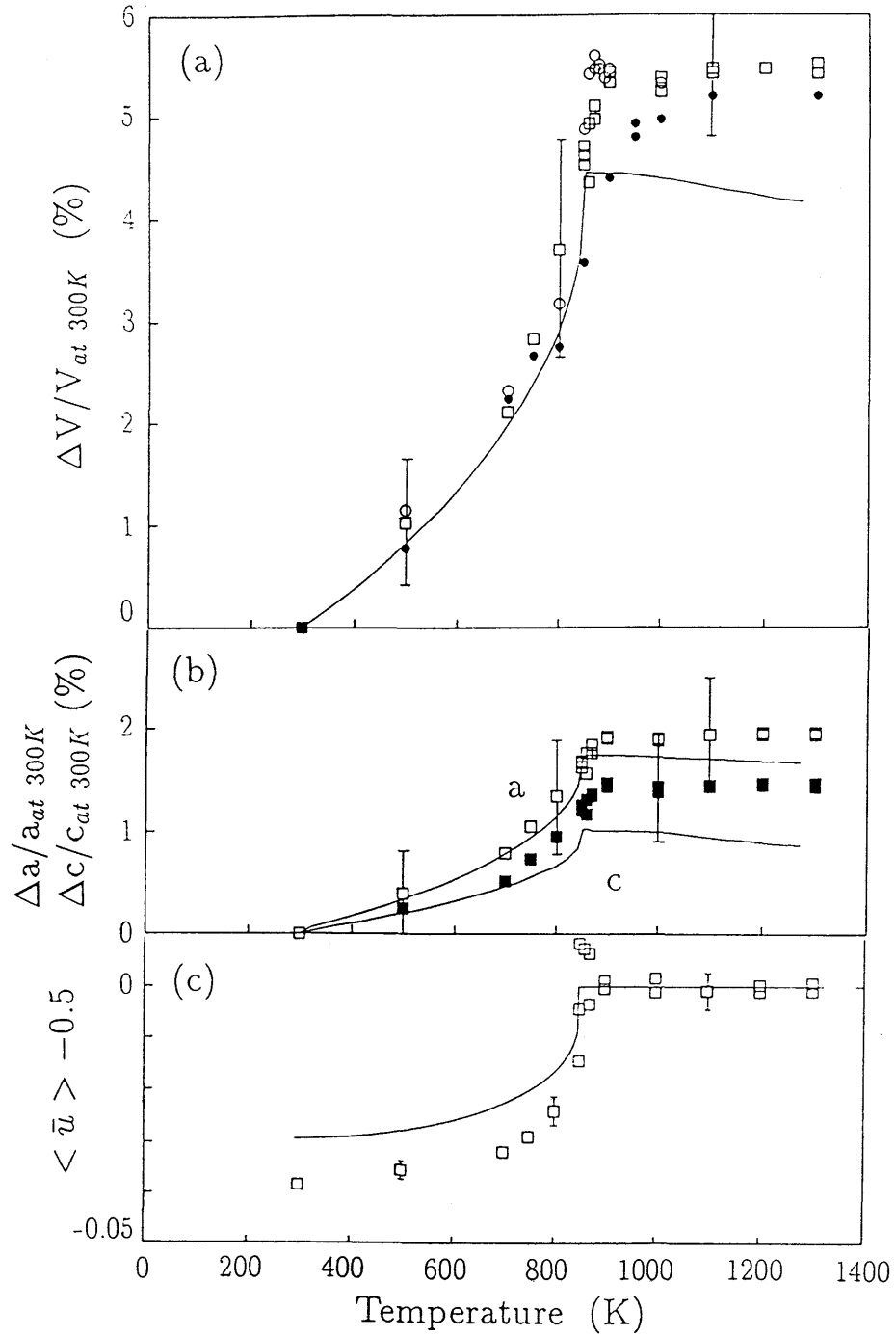


Fig.4-1 (a) The MD result for the thermal expansion of quartz. Open squares represent the 432-particle system with typical magnitude of the fluctuation in $\Delta V/V_{at\ 300K}$, while full circles the 324-particle system and open circles the 576-particle system. Experimental data (Clark et al., 1966) is also shown by a solid line. (b) The MD result of the 432-particle system for temperature dependence of the a-axis (open squares) and c-axis (full squares) of quartz. Experimental data are shown with solid lines. (c) The MD result (open squares) of the 432-particle system for the temperature dependence of the u parameter of silicon averaged over the unit cells and time (12 psec). The solid line is an experimental result (Young, 1962).

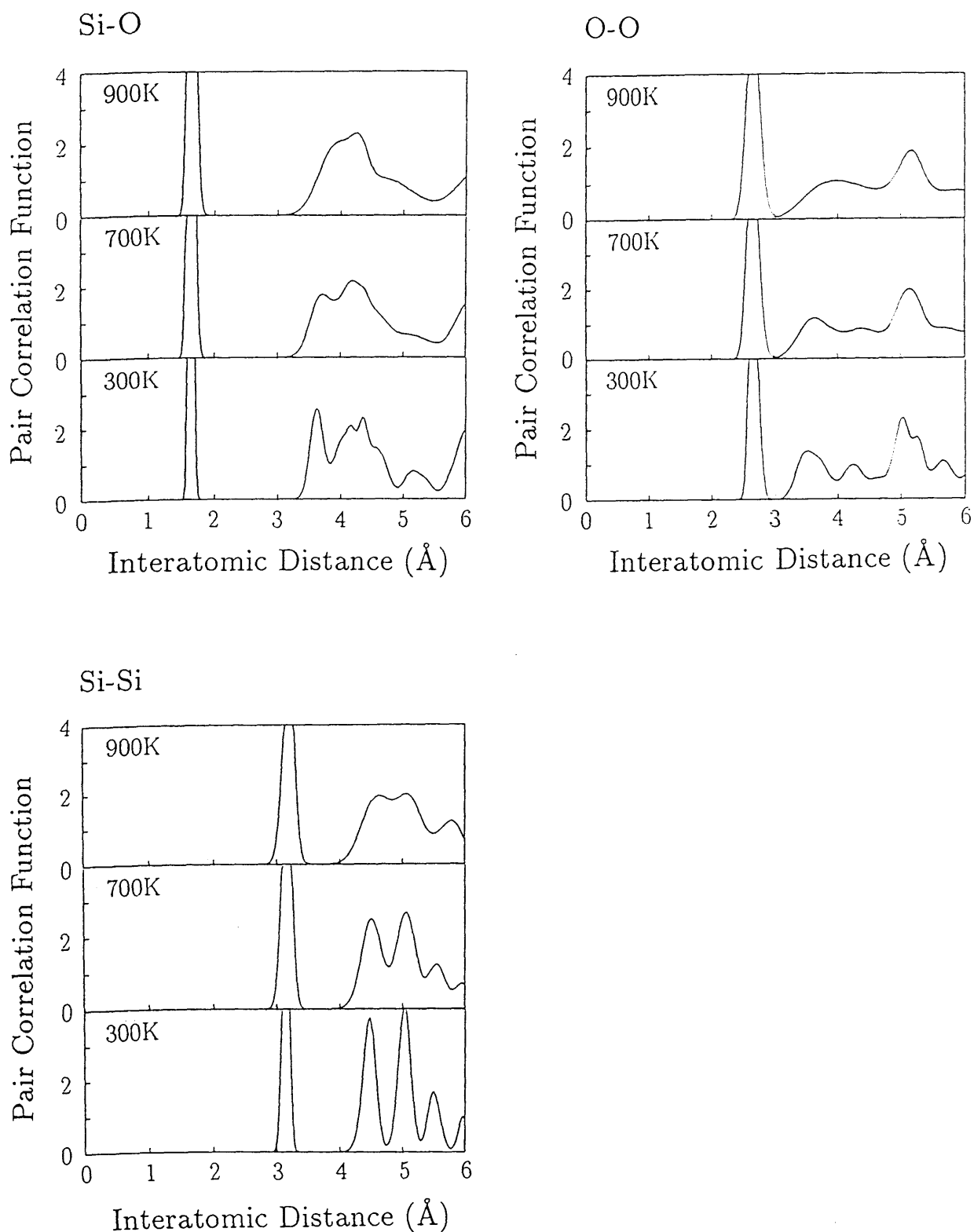


Fig.4-2 Pair correlation functions for Si-O, O-O and Si-Si pairs in quartz at 300K, 700K and 900K. The data were accumulated over 6000 MD steps.

$$\begin{aligned}
\text{Si: (3a)} & (-u, -u, 1/3) ; (u, 0, 0) ; (0, u, 2/3), \\
\text{O: (6c)} & (x, y, z) ; (y-x, -x, z+1/3) ; (-y, x-y, z+2/3); \\
& (x-y, -y, -z) ; (y, x, 2/3-z) ; (-x, y-x, 1/3-z).
\end{aligned}$$

In the low-temperature phase (α -quartz), there are two equivalent phases called α_1 and α_2 , respectively, which are rotated by 180° around the c-axis from each other. The values of the atomic positions at 300K determined experimentally are $u=0.4705(3)$ for α_1 and $u=1-0.4705=0.5295$ for α_2 . In the idealized β -quartz, on the other hand, we have exactly $u=1/2$, and also $y=x/2$ and $z=1/6$, from symmetry restrictions (Young, 1962). We can thus choose $u-1/2$ as an order-parameter of the phase transition, since the other positional parameters of oxygen are highly correlated with u to preserve SiO_4 tetrahedra as shown from the PCF.

In the MD simulation, we have monitored the u parameter averaged for the three silicon atoms in each unit cell at each time step. We denote the u parameter averaged over all the unit cells in the system by \bar{u} (which is a function of time), while the u parameter averaged over all the cells and all the time steps is denoted by $\langle \bar{u} \rangle$. The averaged order parameter, $\langle \bar{u} \rangle - 1/2$, is shown in Fig.4-1(c) against temperature. (Temperature dependences of the other parameters are shown in Appendix A.) Although the simulation starts from the α_1 phase at 300K, the α_2 phase also appears as the temperature is raised. Above T_G , which corresponds to the kink in the volume-temperature relation (Fig.4-1(a)), $\langle \bar{u} \rangle - 1/2$ indeed vanishes.

If we look at a short-time average of u , however, it fluctuates substantially even above this temperature. If we trace the MD history of the atomic configuration at 850K, the system alternates between the period of predominantly α_1 phase and period of α_2 phase. When these periods cross over, there appears a phase boundary between α_1 and α_2 in the system, when the density drops below that for the pure α phase and u averages $1/2$. As the temperature is increased the period (correlation time) during which the system is

in one of α_1 or α_2 becomes shorter. The domain size (correlation length) for α_1 and α_2 phases is also a function of temperature.

To characterize these atomic motions, we calculate the static pair-correlation function of u defined as

$$g(\mathbf{r}) = (1/N) \sum_{\mathbf{r}'} \langle u_{\mathbf{r}+\mathbf{r}'} u_{\mathbf{r}'} \rangle - \langle \bar{u} \rangle^2, \quad (4.1)$$

where \mathbf{r} and \mathbf{r}' denote the position of unit cells, $u_{\mathbf{r}}$ is the local u -parameter in the unit cell at \mathbf{r} , and N is the number of unit cells contained in the basic cell. From $g(\mathbf{r})$ we can estimate the distance over which the displacements tend to be in the same direction. $g(\mathbf{r})$ can be normalized by the thermal fluctuation of u as

$$\tilde{g}(\mathbf{r}) = g(\mathbf{r}) / \overline{\langle (u - \langle \bar{u} \rangle)^2 \rangle}. \quad (4.2)$$

Then $\tilde{g}(\mathbf{r})$ is close to unity if the atomic motions in different cells are strongly correlated, while $\tilde{g}(\mathbf{r}) \sim 0$ when motions are uncorrelated. We show in Fig.4-3 the temperature dependence of $\tilde{g}(\mathbf{r})$ for $\mathbf{r}=(1, 0, 0)$, which is seen to be singular at 850K. Since the correlation length and time vary continuously with T , the α_1/α_2 phase and β phase cannot be strictly discriminated although the critical fluctuation becomes small as T departs from T_C . Above 900K, the correlation length becomes smaller than the sample size studied in the simulation here. Then phase boundaries appear within the system, which expands the system volume as reflected in the flat (saturated) $\Delta V/V$ behavior in Fig.4-1(a). In this context we note that, in the case of a smaller, 324-particle system ($3 \times 4 \times 3 = 36$ unit cells), the whole system tends to stay in a single α phase even above 900K, so that the kink in the temperature-dependence of the volume is smeared around T_C as shown by full circles in Fig.4-1(a). This is the origin of the sharper kink in the volume-expansion relation in larger systems including 576 particles (open circles in Fig.4-1(a)).

We can further characterize the structure by the distribution function of u

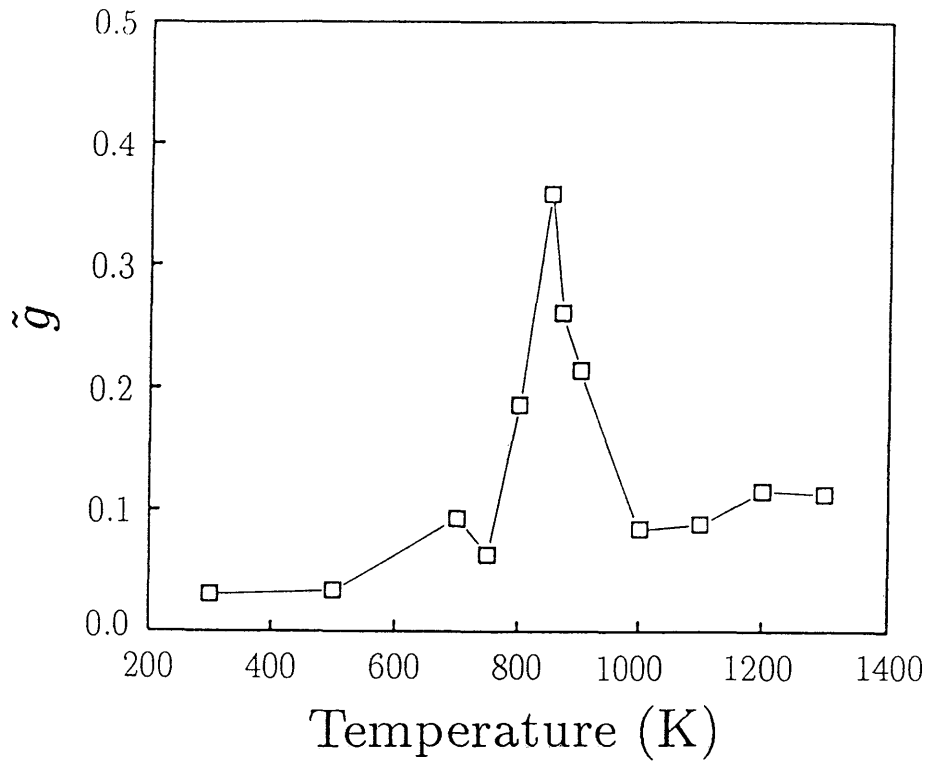


Fig.4-3 Temperature dependence of the normalized static correlation function, \tilde{g} (eq.(4.2) in the text).

accumulated for all the cells (Fig.4-4). At lower temperatures, the motion of each particle is nearly harmonic, so that the distribution function is gaussian. As the temperature increases, the distribution first becomes asymmetric, and then symmetric again above T_C with the peak shifted to $u=1/2$, although the distribution is no longer gaussian. Moreover the distribution is almost independent of temperature above T_C , which suggests that the thermal fluctuation of atoms in the β phase is quite different in nature from that in the α phase.

The anharmonic motion of atoms in this temperature region is explicitly shown in the MD by evaluating the non-gaussian parameter, which dominates the dynamical structure factor. In the three-dimensional isotropic system, the non-gaussian parameter is written as,

$$\alpha_2 = 3 \langle \overline{r^4} \rangle / 5 \langle \overline{r^2} \rangle^2 - 1, \quad (4.3)$$

where r is the displacement of particles from the equilibrium position and average is taken over time and particles (Rahman, 1964). In crystals, the potential energy surface felt by a particle is usually anisotropic, so that we define the one-dimensional non-gaussian parameter as

$$\alpha_{2,x} = \langle \overline{x^4} \rangle / 3 \langle \overline{x^2} \rangle^2 - 1. \quad (4.4)$$

It can easily be shown that $\alpha_{2,x}$ is zero if the distribution of x is gaussian, that is, when the atomic motion is harmonic, while it is negative for dumpier distribution and possibly positive for asymmetric distribution. The temperature dependence of the non-gaussian parameters for the positional parameters of silicon and oxygen is shown in Fig.4-5(a) and (b). (Note that x -coordinate of Si coincides with the u parameter.) The non-gaussian parameters become nonzero around and above T_C only for Si: x , y and O: y , z , which means quite anisotropic anharmonicity in the atomic motion. These coordinates are indeed those which

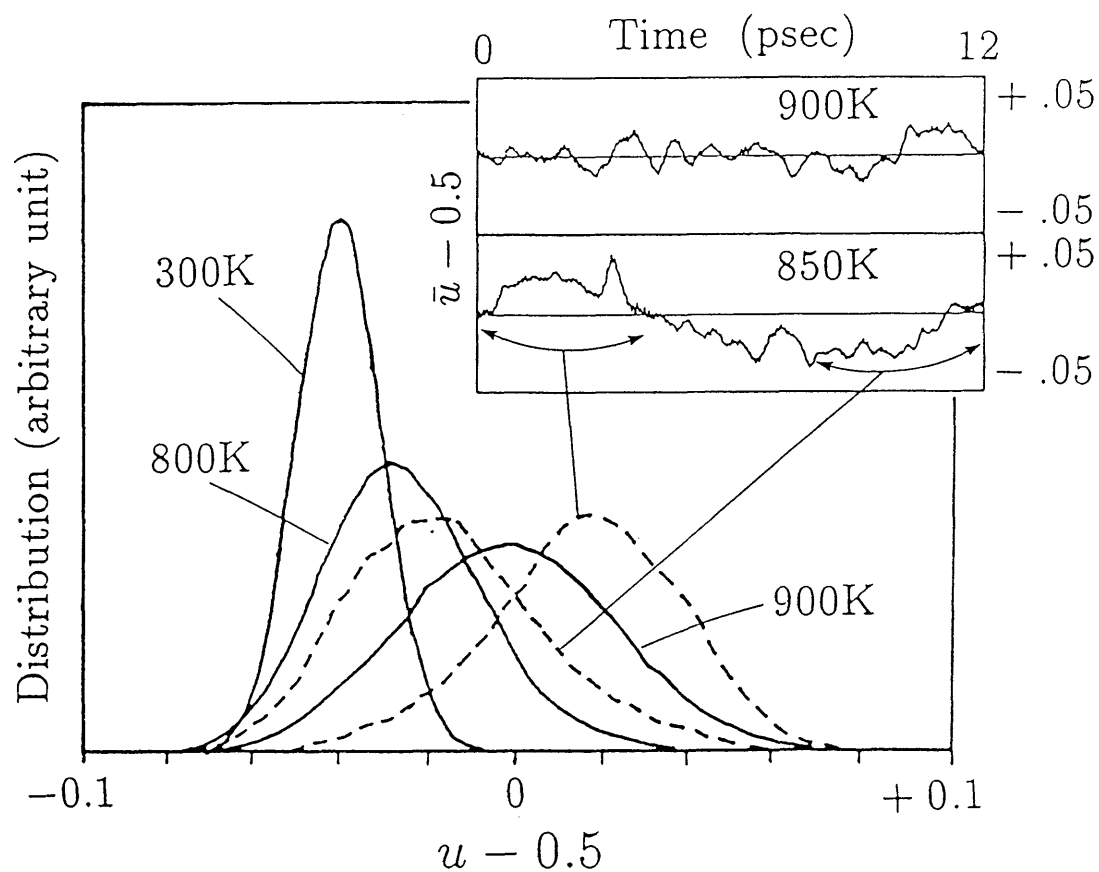


Fig.4-4 The distribution of the u parameter of silicon. The data were accumulated over 12 psec (full lines) or 4 psec (dashed lines) at different intervals at 850K. The inset shows a typical trace of the u parameter, averaged over all the cells, against MD step.

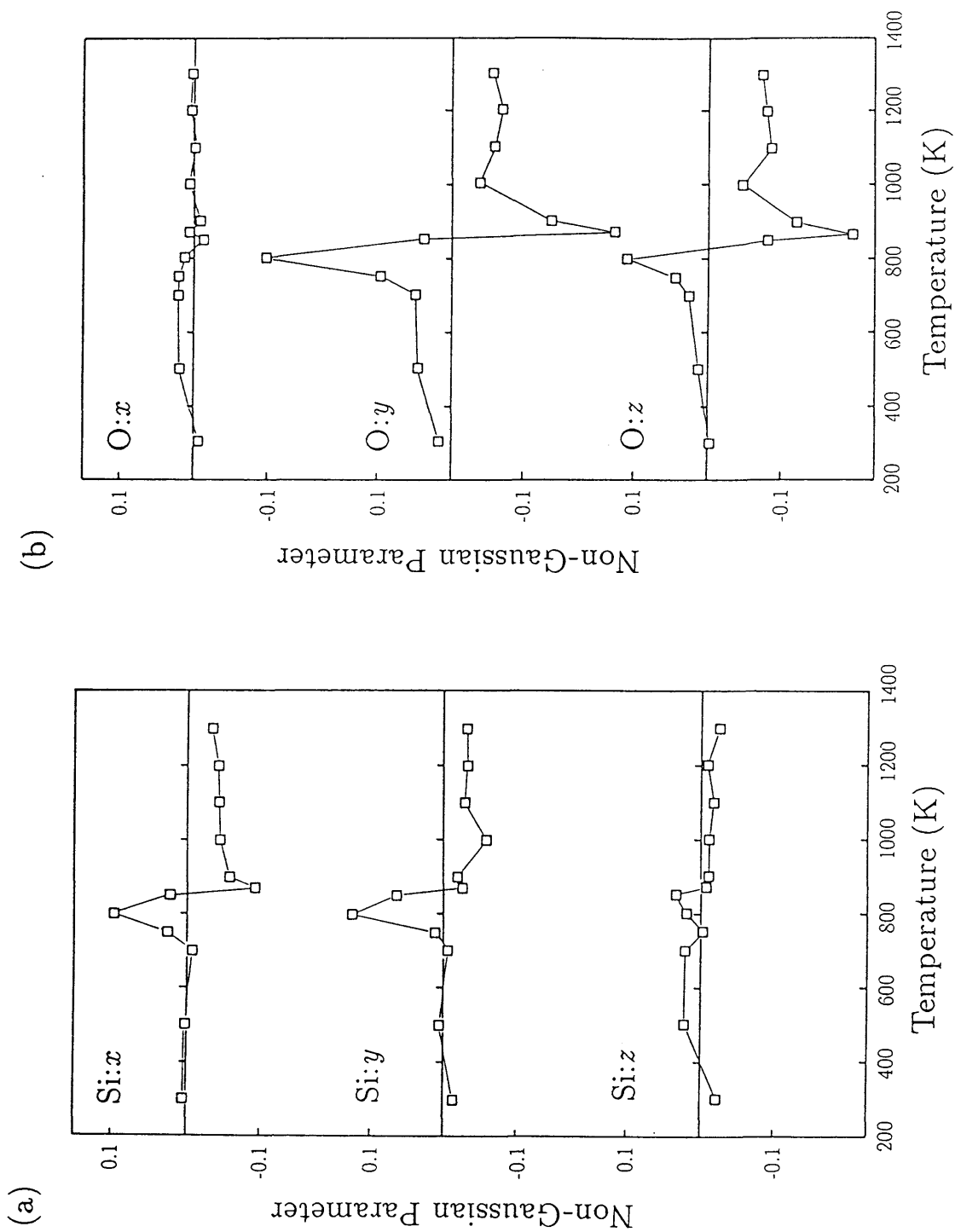


Fig.4-5 Temperature dependence of the one-dimensional non-gaussian parameter (eq.(4.4)) for the fractional coordinates of (a) silicon and (b) oxygen.

change drastically after the phase transition (see Appendix A).

On the other hand, the distribution function for u averaged over a period shorter than the correlation time, which is about 4psec at 850K in the simulation, is shown in Fig.4-4 by dashed lines. Depending on the interval at which the average is taken, the distribution exhibits either α_1 or α_2 behavior while, when averaged over a long time, the distribution function at 850K already exhibits a single peak like that at 900K. When seen locally, α_1 and α_2 phases switch to each other even at 900K (Fig.4-6), at which the system comprises α_1 and α_2 domains. Thus, although the atomic distribution averaged over long time mimics a displacive transition, the β -quartz structure is only realized as an average of the structure dynamically hopping between α_1 and α_2 with a T-dependent correlation length/time.

The β -quartz structure is actually shown to be statically unstable. We have calculated the dynamical matrix within a quasi-harmonic approximation for the time-averaged atomic configuration with thermal expansion obtained by the MD at various temperatures. We have found that, while the phonon dispersion at 300K shows good agreement with experimental results (see Section 3.2), the softening of some phonon modes sets in (Fig.4-7) when T is increased past 700K with the frequency eventually becoming imaginary above 750K. The softened modes include the one directly connecting α and β at Γ point. The phonon softening is thus consistent with experimental results (Barron, Huang and Pasternak, 1976). This implies that, although the distribution function is single-peaked, the fictitious β -quartz position is in fact an unstable point in the potential locally felt by atoms, which, despite the suppressed barrier due to thermal expansion, continues to be double well (corresponding to α_1 and α_2 configurations). Even though the softening of phonon modes is observed, the transition could be thus classified as an order-disorder regime according to the terminology by Schneider and Stoll (1974).

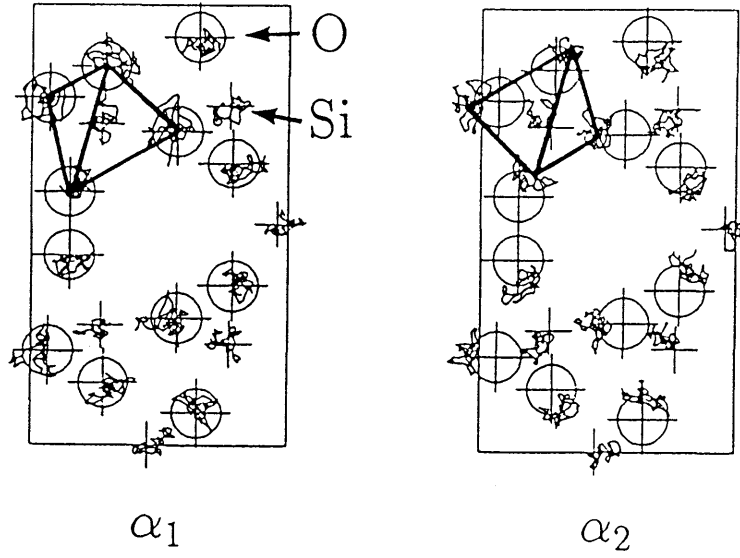


Fig.4-6 The trajectory (for every five MD steps over 1 psec) of atomic positions in a part of the system projected to x-y plane at $T=900\text{K}$. The two frames, taken at different time intervals in the same run, correspond to α_1 and α_2 phases, respectively. Typical SiO_4 tetrahedra are shown with thick lines and the ideal positions of α phase are indicated with crosses and circles.

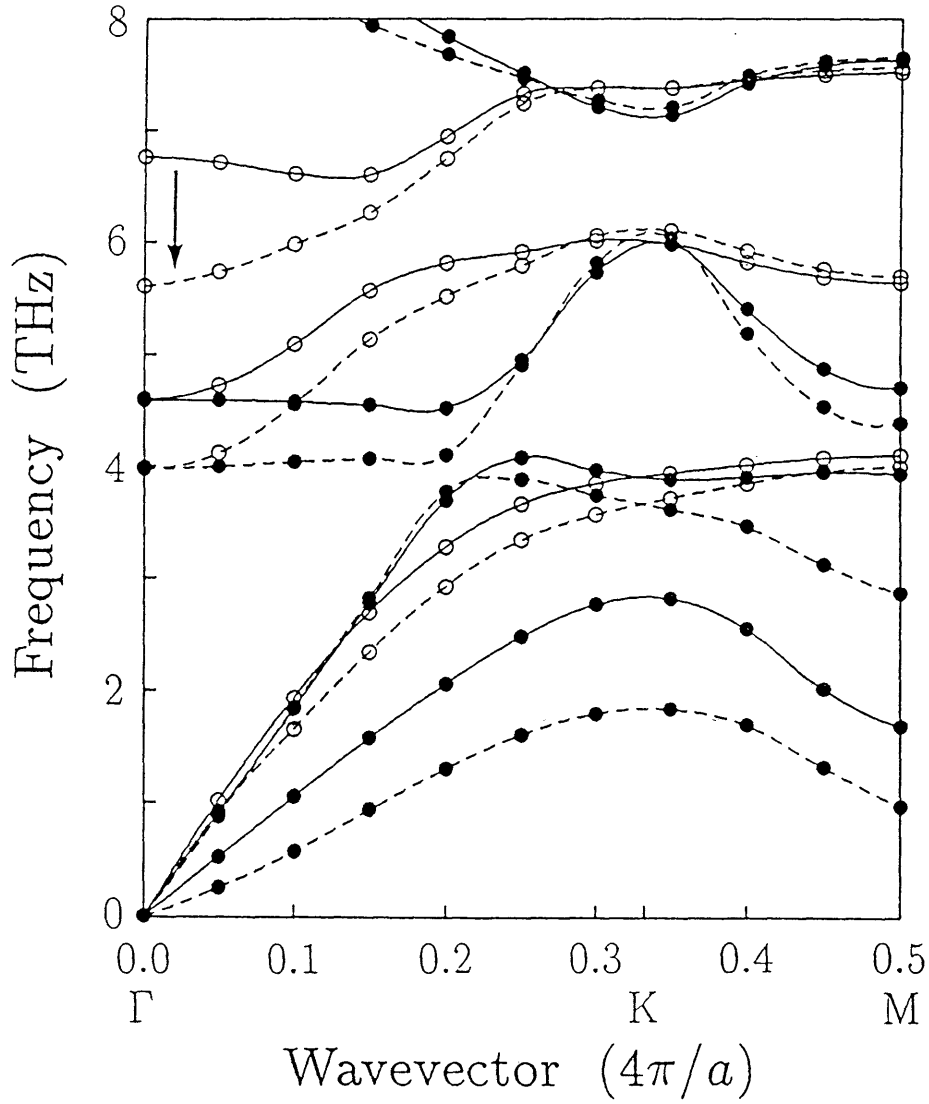


Fig.4-7 Phonon dispersion at $T=300\text{K}$ (full lines) and $T=700\text{K}$ (dashed lines) calculated within a quasi-harmonic approximation. Full (open) circles represent antisymmetric (symmetric) modes. The softening of a mode that directly connects α and β structure is indicated by an arrow.

Section 4.3. Summary and discussion

We have investigated the α - β phase transition of quartz by the MD simulation and shown that the phase transition is successfully reproduced at about 850K. The β -quartz structure is only realized as an spatio-temporal average of the local structure hopping between α_1 and α_2 structure.

Physically, the competing factors are the thermal energy and the potential barrier separating α_1 and α_2 structures in the configurational space. We show in Fig.4-8 two potential-energy surfaces against the u parameter of silicon: the solid line and the dashed line are calculated for the unit-cell dimension at 300K (α phase) and 900K (β phase), respectively. Here the positional parameters for oxygen atoms are optimized for each value of u . According as the positions of the potential minima shift inwards with the volume expansion, the curvature of the potential-energy surface changes resulting in the softening of some phonon modes (Fig.4-7). The height of the potential barrier also decreases, and finally the hopping of atoms between α_1 and α_2 structures commences when the local thermal energy surpasses the barrier. Once the phase boundaries of α_1 and α_2 structures begin to appear frequently, the volume expansion is enhanced so that the whole system realizes the density of β phase. This is why the consideration of the thermal expansion is essential in this problem. It is also seen that the potential barrier remains to exist even at the density of the β phase so that the β phase is not achieved as a stable structure. Suppose we consider the canonical distribution of u parameter in a certain unit cell within the mean-field approximation, putting the other cells at the ideal β positions. Then the distribution of u parameter is expected to be double-peaked in the β phase, and in fact local structure stays in the same α phase for some time (Fig.4-6). However, after the spatio-temporal average, the atomic distribution shows a single peak in the β phase (Fig.4-4) perhaps because of the thermal fluctuation with large anharmonicity which can be correlated over several unit cells. Naturally it is very difficult to discriminate such a dynamical phase transition

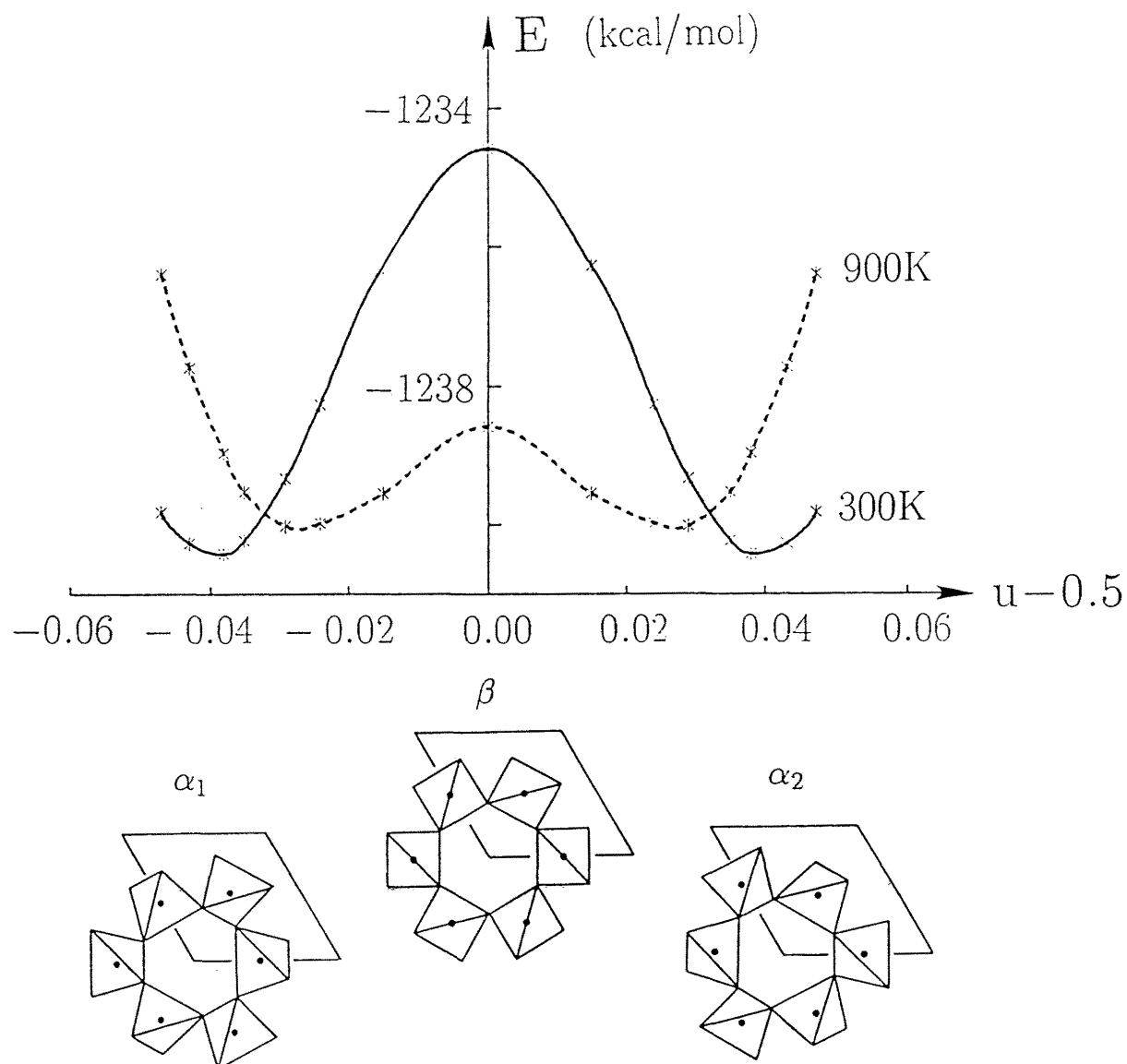


Fig.4-8 Configurational potential energy surfaces of quartz at $T=300\text{K}$ (a full line) and at $T=900\text{K}$ (a dashed line). Structures of the α_1 , α_2 and β phases are illustrated below with the SiO_4 tetrahedra as seen from the c -axis.

from a displacive one with use of X-ray diffraction (Young 1962), which may have resulted in a controversy as to the structure of the β -quartz.

In summary, the phase transition of quartz elucidated by the MD simulation has a peculiar dynamical character. The dynamical structure of the β phase elucidated here supports the experimental observation by Tendeloo et al. (1976) and Wright et al. (1981), who have suggested that the structure fluctuates between α_1 and α_2 from electron microscopy, electron diffraction and neutron diffraction.

Chapter V. Pressure-Induced Structural Transformations

Section 5.1. Introduction

To study the pressure-induced structural transformations of silica is interesting for the following reasons:

(1) The crystalline-to-amorphous transformation in the solid state is currently a subject of intense study. Since the amorphization of H_2O ice under pressure was discovered (Mishima, Calvert and Whalley, 1984), the possible occurrence of the pressure-induced amorphization in other systems and its mechanism have been widely investigated. Very recently the pressure-induced amorphization of crystalline silica at room temperature was confirmed by experiments using Raman spectroscopy (Hemley, 1987) and X-ray diffraction (Hemley, Jephcoat, Mao, Ming and Manghnani, 1988). Characterization of the resultant amorphous structure is required to elucidate the mechanism of the amorphization. Amorphization experimentally observed can be related to crystal-crystal transition for the reason stated later in this chapter.

(2) In pressure-induced transitions of silica, the amorphous phases are experimentally shown to be appreciably denser than the crystalline counterparts, presumably because of the framework structure just as in the case of water. Such a pressure-density relation of minerals is important because it is closely related to the convection of materials deep inside the earth.

(3) The application of high pressures at low (room) temperature may provide new reaction paths towards new polymorphs which could never be obtained by high pressures at high temperatures which tend to exclude the phases other than thermodynamically most stable.

As for the mechanism of compression, it is widely believed that the compression of amorphous silicate at low pressure occurs due to increased packing efficiency of corner-linked SiO_4 tetrahedra with decreased Si-O-Si bridging angles. At high pressures, on the other hand, it is reported that the fraction of octahedrally coordinated silicon atoms increases continuously and

reversibly with increasing pressure from infrared measurements (Williams and Jeanloz, 1988). Stolper and Ahrens (1987) have proposed a mechanism to explain such pressure-induced coordination changes in silicate melts and glasses: according to their model, continuous displacements of silicon atoms in the distorted SiO_4 chain result in a closely packed arrangement of oxygen octahedra (Fig.5-1). We have to check whether such structural transformation could occur in crystalline silica.

From these points of view, we report in this chapter an MD study for pressure-induced structural transformations at room temperature for various polymorphs of silica. We predict novel structural transitions for low-quartz, low-cristobalite and coesite, where some of the new phases, appearing without diffusion processes, comprise mixed array of four-fold and six-fold Si-O coordinations. Stishovite, the densest polymorph of silica ever known, is shown to hold its identity up to 250GPa with deformation to the CaCl_2 structure.

Section 5.2. Interatomic potentials

Before turning to the MD study, we first examine the pairwise interatomic potential of silica in applying to the phase transition accompanied by coordination changes. The pairwise interatomic potential obtained in Chapter II has the virtue that they can reproduce both tetrahedrally (four-fold) coordinated systems (low-quartz, low-cristobalite and coesite) and octahedrally (six-fold) coordinated systems (stishovite) in contrast to covalent potentials (see, for example, Lasaga and Gibbs, 1987) which are applicable only to tetrahedrally coordinated systems. However, as mentioned in Chapter III, a flaw in the cluster approach for obtaining pairwise potentials is that, since the approach concentrates on the curvature of potential surfaces, it does not necessarily reproduce the exact enthalpy difference of each phase. For example, the observed enthalpy of formation of six-fold coordinated stishovite (Holm, Kleppa

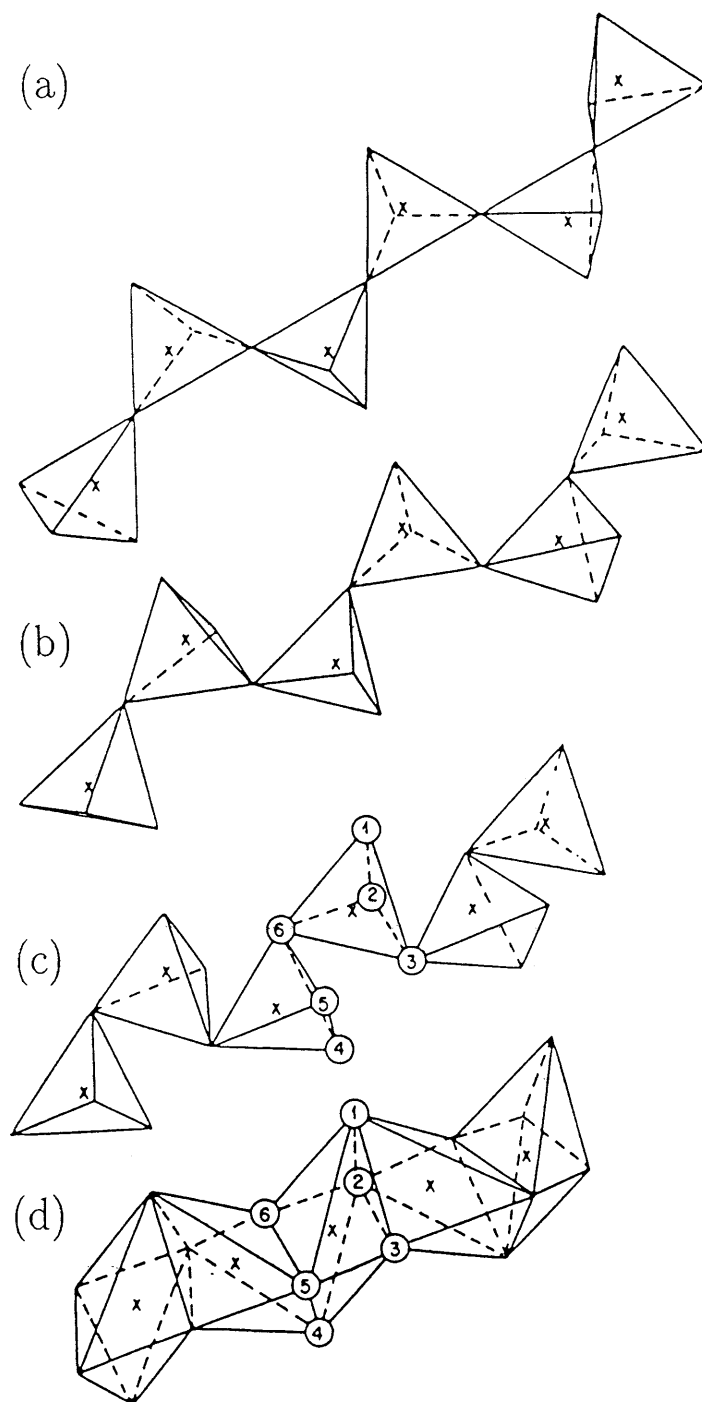


Fig.5-1 Stolper and Ahrens' model for the continuous transformation of tetrahedral SiO_4 to octahedral SiO_6 . (a)-(c), The reduction of the Si-O-Si bridging angle from 180° to 140° to 100° . (d), The new octahedral coordination with the oxygen ions located in the same position as in (c). Oxygen atoms are at the vertices (numbers show equivalent ions); crosses, silicon atoms. (From Stolper and Ahrens, 1987).

and Westrum, 1967) is about 10 kcal/mol higher than that (-217.8kcal/mol) of four-fold coordinated low-quartz (Wise et al., 1962) as compared with the difference of about 1 kcal/mol as calculated from the potential described in previous sections. Since we are interested in pressure-induced structural transformations, which involve change of the Si-O coordination number, we slightly modify the potential parameters from those obtained in Chapter II to reproduce the enthalpy difference of stishovite and low-quartz. Only a reduction of the atomic radius a_{Si} by 1% (0.01\AA) is sufficient to accomplish this. The final potential parameters used here are $Q_{\text{O}}=-1.2$ and $Q_{\text{Si}}=+2.4$ in units of elementary charge, $a_{\text{O}}=2.05$, $a_{\text{Si}}=0.86$, $b_{\text{O}}=0.176$, and $b_{\text{Si}}=0.033$ in \AA , and $c_{\text{O}}=70.4$ and $c_{\text{Si}}=23.2$ in $\text{kcal}\text{\AA}^6\text{mol}^{-1}$ and $1/r^6$ term between two silicon atoms is neglected. Structural parameters, bulk moduli and cohesive energies of each polymorph are listed in Table 5-1. The structural features of all the polymorphs are reproduced again, even better than the result in Chapter III especially for low-quartz. It would be desirable if we could incorporate the accuracy of the total enthalpy in the best-fit procedure for optimizing the pair potential. Such a procedure would require the first-principles bulk calculations as well as the cluster calculations.

We should note here that the total energy (or cohesive energy) of each phase is very sensitive to the potential parameters. Especially regarding the energy difference between four-fold and six-fold Si-O coordination, the ratio $a_{\text{Si}}/a_{\text{O}}$ is very important, which is consistent with the classical principle on the coordination number of anions around cations by Pauling (1929): smaller $a_{\text{Si}}/a_{\text{O}}$ ratio makes four-fold systems more stable. Since the relative stability within the tetrahedrally coordinated polymorphs is insensitive to the $a_{\text{Si}}/a_{\text{O}}$ ratio, the simulated coesite with the new parameters is still too stable compared with experimental results (Holm et al., 1967) by about 5kcal/mol .

It should also be noted that the relative stability of the phases is also sensitive to the functional form of the interatomic potentials even within the pair-potential approximation. For instance, we have tried the traditional Morse

Table 5-1 Physical properties of silica at room temperature and ambient pressure obtained by MD simulations using the potential parameters in this chapter. See Table 3-1 for the references of the observed data (Obs.).

	low-quartz		low-cristobalite		coesite		stishovite	
	Obs.	MD	Obs.	MD	Obs.	MD	Obs.	MD
Density (g/cm ³)	2.65	2.50	2.32	2.38	2.92	2.80	4.29	4.03
K ₀ (GPa)	38(3)	38.1(2)	18	15.3(2)	96(3)	98.8(3.3)	296(5)	296(1)
K ₀ '	6.0(2)	4.7(1)	—	12.7(4)	8.4(1.9)	5.8(1.2)	4.0(1.4)	6.0(4)
Energy (kcal/mol)		-1249.6		-1245.3		-1254.0		-1238.4

potentials between Si and O in the fitting procedure only to find that the octahedrally coordinated stishovite is much more stable than the other polymorphs. When applied to the MD simulation of vitreous or liquid silica, such potentials give rise to collapsed six-fold glasses.

Section 5.3. Molecular dynamics simulation of high-pressure compression

We apply a hydrostatic pressure to each polymorph of silica in the MD study with the constant-pressure and constant-temperature algorithm described in Chapter III. The number of atoms in the system is 576 (containing 48 unit cells), 576(64), 768(16) and 576(96) for low-cristobalite, low-quartz, coesite, and stishovite, respectively, with periodic boundary conditions. The pressure is increased slowly (by 1 – 5GPa each time the equilibrium is attained).

The obtained equations of state for SiO₂ in various polymorphs at room temperature are shown in Fig.5-2 along with the equations of state by *real* experiments in the inset (Hemley, Jephcoat, Mao and Manghnani, 1988). The results for low-quartz, coesite and stishovite, before they undergo structural transitions, are in good agreement with the experimental results.

The most interesting point is the stability of each polymorph. Low-

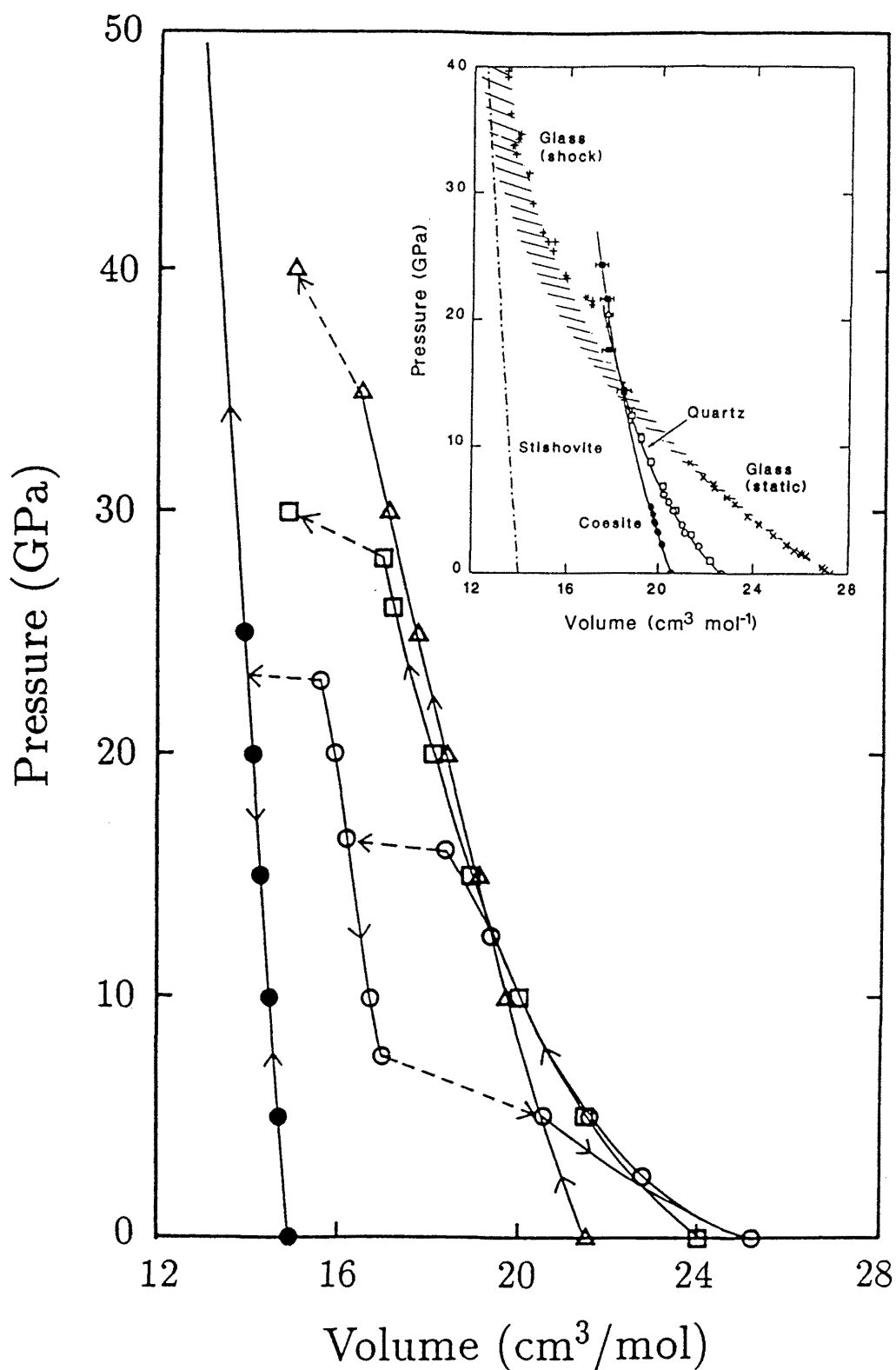


Fig.5-2 Pressure-volume relation for low-quartz (\square), coesite (Δ), stishovite (\bullet) and low-cristobalite (\circ) obtained by MD. Solid lines represent continuous change and broken lines discontinuous change of volume due to pressure-induced structural transition. Hysteresis is indicated by arrows. Pressure-volume relation obtained by experiments are shown in the inset. (After Hemley et al, 1988).

cristobalite shows a structural transition with discontinuous volume-reduction into a novel polymorph at 16.5GPa, which is reported here for the first time. The new phase (Fig.5-3 and Table 5-2) has a space group *Cmcm*. The space group of low-cristobalite, $P4_12_12$, has an orthorhombic subgroup $C222_1$, of which *Cmcm* is another supergroup. The *Cmcm* phase is stable until the second phase transition into stishovite sets in at 23GPa. The space group of stishovite, $P4_2/mnm$, is in turn a supergroup of *Cmcm* and $P4_12_12$. The atomic configuration along the reaction path is illustrated in Fig.5-4 and in Appendix B. Remarkably, this *Cmcm* structure includes equal numbers of four- and six-coordinated silicon atoms. Note that these structural phase transitions occur continuously without diffusion processes, that is, no isolated atoms nor disordered states appear at the transition point. With decreasing pressure the *Cmcm* phase becomes unstable at about 7GPa resulting in an amorphous phase (Fig.5-5), whose structure and density are similar to those of low-cristobalite, while once stishovite is formed above 23GPa, it remains stable against decompression. The reversible transformation between four-fold and six-fold Si-O coordination is consistent with the mechanism suggested by Stolper and Ahrens (1987) (Fig.5-1).

Low-quartz also exhibits a novel structural transition at 28–30GPa. One of the pressure-induced phases is shown in Fig.5-6(a). This is basically the α - PbO_2 structure with only six-fold Si-O coordinations, which is slightly denser than stishovite and has been proposed, but not established, as a high-pressure form of SiO_2 (Matsui and Kawamura, 1987) (see Fig.5-6(b) for comparison with stishovite). The time-development of the transformation is shown in Appendix B.

Interestingly, another pressure-induced phase has been obtained, depending on the MD run, as shown in Fig.5-7(a) and (b), which is also crystalline but frustrated in the following sense. The phase contains both four- and six-coordinated Si atoms as in the *Cmcm* phase, while the average coordination number is not $(4+6)/2$ but 5.3 in this case. The three-fold screw axes of the

Table 5-2 Crystallographic data of the *Cmcm* phase of silica at 15GPa, 300K.

Orthorhombic cell			
$a = 5.20\text{\AA}, b = 7.44\text{\AA}, c = 5.58\text{\AA}$			
$\rho = 3.70\text{g/cm}^3$			
Si(4a)	x=0	y=0	z=0
Si(4c)	x=0	y=0.357	z=0.25
O(8f)	x=0	y=0.223	z=0.029
O(8g)	x=0.260	y=0.481	z=0.25

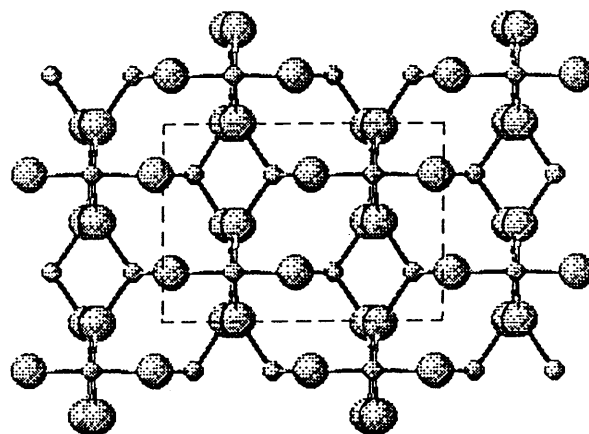


Fig.5-3 The new *Cmcm* phase involving both four- and six-fold coordinations predicted by this study as seen from the a-axis, which corresponds to the c-axis of low-cristobalite and stishovite. Small spheres represent silicon atoms and large spheres oxygen atoms. The unit cell is shown by dashed lines.

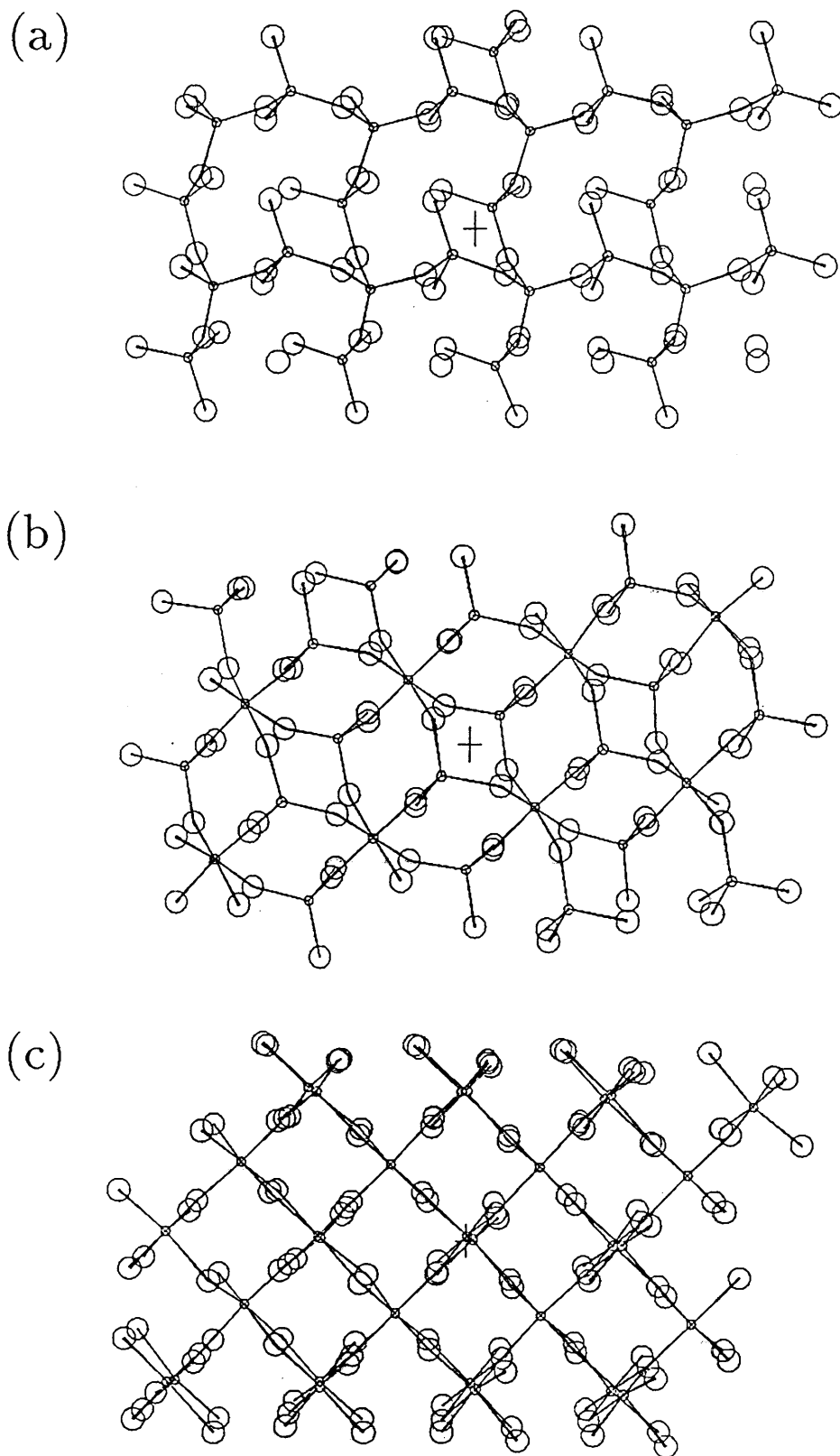


Fig.5-4 Continual structural transformations induced by compression from (a) low-cristobalite (at 15GPa) to (b) the *Cmcm* phase (at 17GPa) to (c) stishovite (at 25GPa). Small spheres represent silicon atoms and large spheres oxygen atoms.

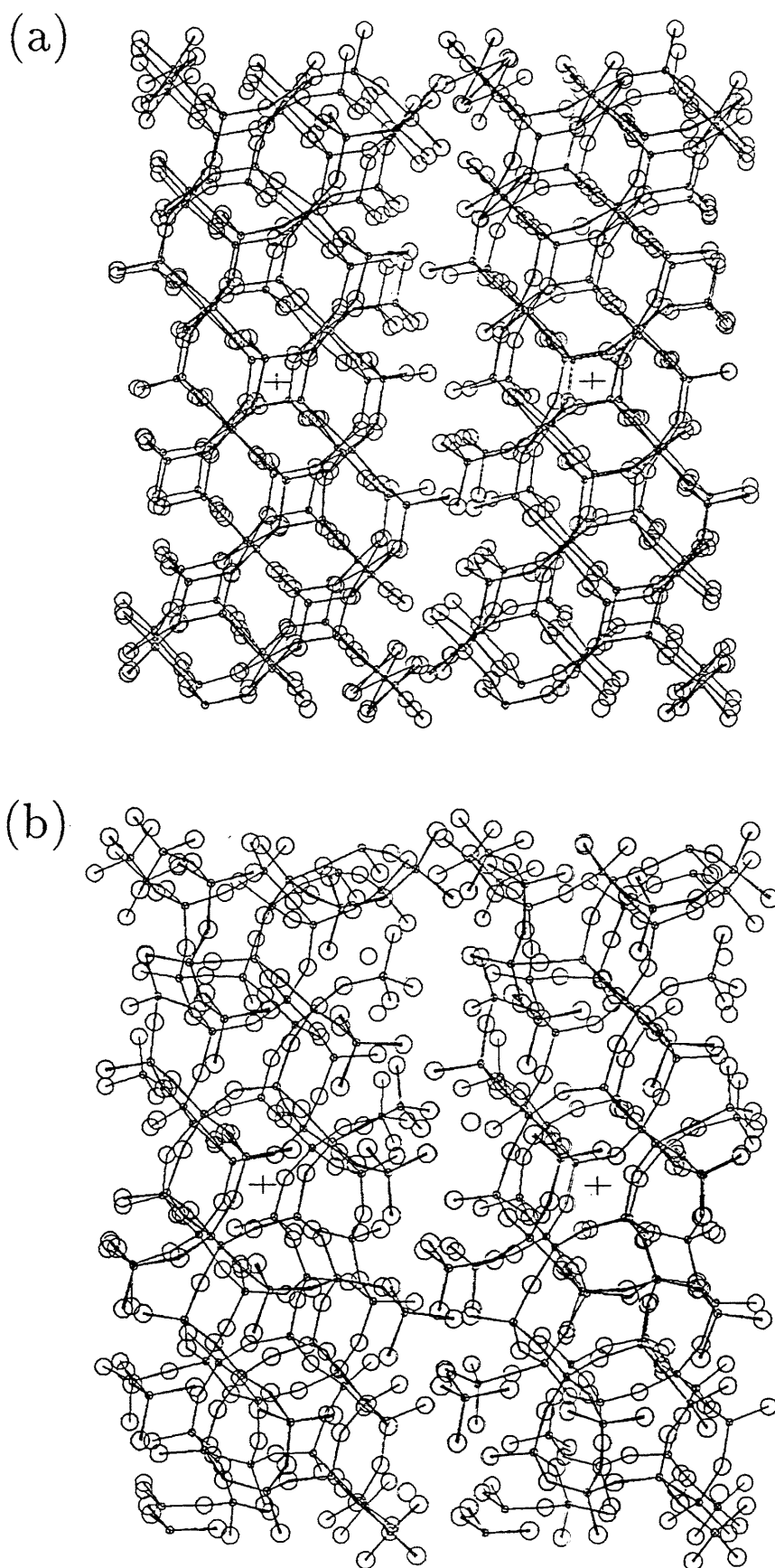


Fig.5-5 Structural transformation induced by decompression from (a) the *Cmcm* phase to (b) the amorphous phase which contains only tetrahedrally coordinated silicon atoms (stereoscopic view).

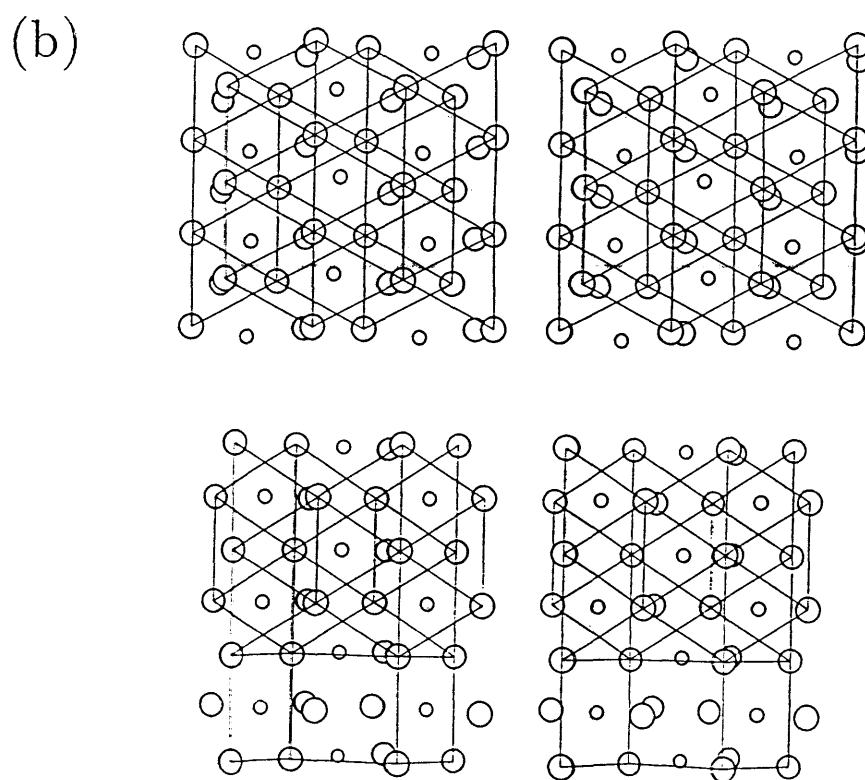
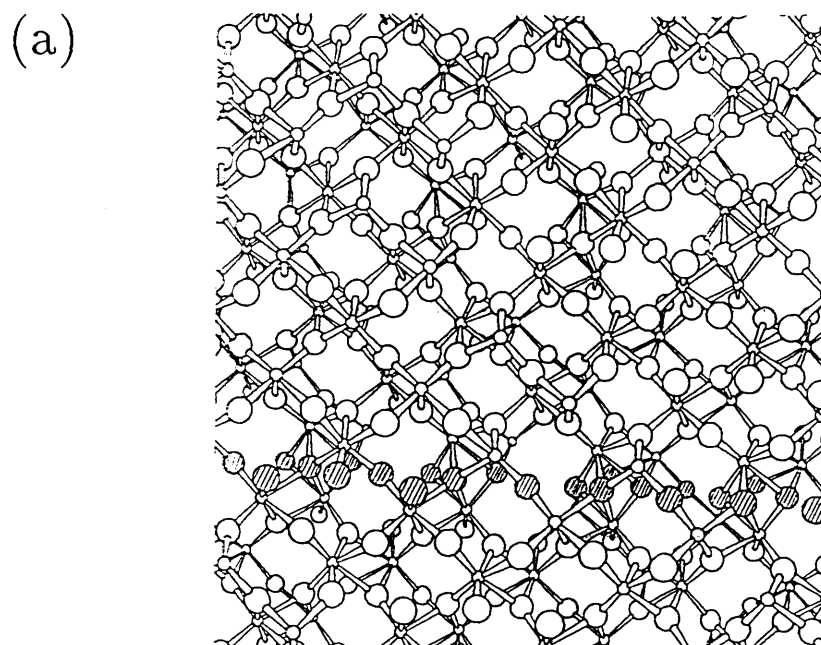


Fig.5-6 (a) The α -PbO₂ phase with some defects obtained by compression of low-quartz up to 30 GPa at room temperature. Small spheres represent silicon atoms and large spheres oxygen atoms. A plane of close-packed oxygen atoms is shown by hatching. (b) Stereoscopic view of the α -PbO₂ structure (the upper panel) and stishovite (the lower panel) (From Matsui, 1979).

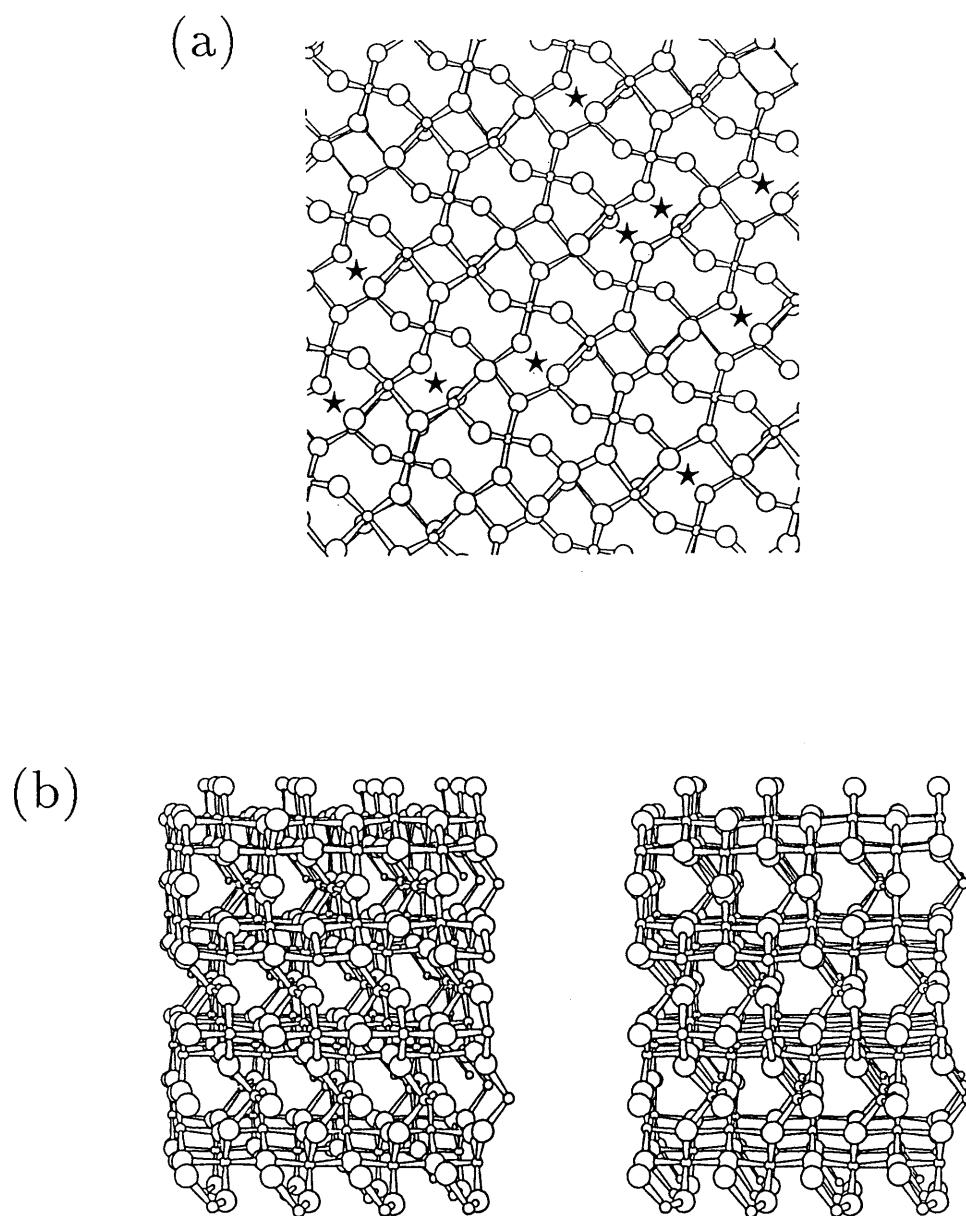


Fig.5-7 A frustrated crystal phase obtained by compression of low-quartz up to 30 GPa at room temperature: (a) A projection to the plane normal to the a-axis and (b) a stereoscopic view seen from the c-axis of starting low-quartz. Small spheres represent silicon atoms and large spheres oxygen atoms. The missing bonds of the frustrated crystal phase are marked with ★ in (a).

starting low-quartz is destroyed. Conspicuous feature, however, is that, despite their ordered array, the unusual configuration of the four- and six-fold sites demands considerable distortion of bond lengths and angles. This appears as a random distribution of missing bonds of a finite density where we regard Si and O bonded when they are separated less than 2.16\AA , a chemically acceptable bound. Frustrated aspect also appears in the corrugated SiO_2 sheet (SiO bond angles $\neq 90^\circ$) in Fig.5-7(b). Peaks in the radial distribution function are also shown to be broadened like in a glass. The configuration of these missing bonds fluctuates in time (of which Fig.5-7 is a snapshot), and the missing bonds are shown to disappear when the pressure is increased to 50GPa. Reflecting the equivalent three directions in the quartz, the direction of the crystal assumes one of the three, depending on the MD run. It is thus conceivable that compression of a macroscopic sample produces domains of these $\alpha\text{-PbO}_2$ or frustrated crystal phases, which may require a careful experimental study to distinguish from conventional amorphous phase. The mixed coordinations predicted here could be identified by the infrared measurement. The critical pressures for structural transitions obtained here are consistent with the recent experimental results by Hemley et al. (1987) on the amorphization of low-quartz at about 25–30GPa.

These structural transformations of low-quartz are again diffusionless, and the six-fold Si-O coordinations almost completely return to four-fold after decompression to normal pressure. This is consistent with the infrared-spectrum result that the coordination number of amorphous SiO_2 changes reversibly with pressure even at room temperature (Williams and Jeanloz, 1988).

Some technical details need to be addressed: although the constant-temperature algorithm was used here, the heat of reaction produced during the structural transition is rapidly removed in the present MD, so that metastable phases are more favoured. Also, if we employ $3\times 3\times 3$ unit cells instead of $4\times 4\times 3=48$ for the basic cell of the periodic boundary condition, the *Cmcm* phase, which is made of two unit cells of low-cristobalite, is by-passed and low-cristobalite changes directly into stishovite above 20GPa. Thus the detail of the

new polymorph may have to be determined for larger system sizes. Yet we expect that the same kind of transition involving the mixed coordination numbers will occur in real systems.

The experimental study on the compression of low-cristobalite at room temperature was carried out by Tsuchida and Yagi very recently (1989) and a novel crystal-to-crystal transformation was discovered at about 10GPa. The resultant crystal, however, seems to be different from the *Cmcm* structure, although the characterization is not finished yet.

As for the coesite, the basic cell is shown to slightly change from monoclinic to triclinic at 15–20GPa, which may be associated with the observed change of Raman spectrum at 22–25GPa (Hemley, 1987). Coesite, too, undergoes a structural transition into a six-fold rich phase at 35–40GPa, which is consistent with the experimentally reported amorphization at 30–34GPa (Hemley et al., 1988).

Finally, stishovite exhibits no drastic structural change up to 250GPa, the highest pressure studied here, except that the structure eventually becomes orthorhombic (with the CaCl_2 structure). This result suggests that the recently proposed $Pa\bar{3}$ phase (Park, Terakura and Matsui, 1988), which is predicted to be denser and thermodynamically more stable than stishovite above 60GPa, is difficult to attain dynamically by simple compression at room temperature (Tsuchida et al., 1989). This does not necessarily imply, however, that the $Pa\bar{3}$ phase is unstable. Even if the $Pa\bar{3}$ phase is more stable than stishovite, it is possible that the potential barrier in the atomic configuration space separating the two phases would be higher than $k_B T$ at room temperature so that a diffusion process at high temperatures would be necessary for the transition. This problem could also be tackled by the MD method, which is also applicable to transitions involving diffusion processes.

Section 5.4. Summary and discussion

We have performed the MD simulation of pressure-induced structural transformations of crystalline silica. The simulated equations of state agree very well with those observed in the real experiments. Pressure-induced structural transitions of the polymorphs have also been found.

The mechanism of the pressure-induced structural transformation of tetrahedrally coordinated silica at room temperature is shown to be primarily the increase of the Si-O coordination number, which occurs locally without diffusion process. As the pressure increases, the network structure of tetrahedrally coordinated Si collectively collapses to more close-packed structures with richer octahedrally coordinated Si, which results in a discontinuous reduction of volume. In some cases, four-fold silicon atoms partly remain after the transition, resulting in mixed coordination numbers. The application of high pressure at room temperature thus provides intriguing reaction paths towards new polymorphs.

In this chapter, we have focused on the structural transformation of crystals, though the compression mechanism of silica elucidated here will be applicable to the vitreous or liquid silica. In disordered phases, different configurations are realized for different sites in the system, so that a coordination change (like four-fold cristobalite into four- and six-fold *Cmcm* phase) may not occur collectively as in a crystal, but different sites can undergo the change at different pressures. This will lead to the continuous reduction of volume. The reversibility of the process is confirmed by the MD result that the α -PbO₂ phase with defects, which is obtained by the compression of quartz, returns almost completely to four-fold structure after decompression to normal pressure.

Finally we would like to comment on the atomic diffusion. We have repeatedly mentioned that the structural phase transitions obtained here are diffusionless. However, this is in a specified meaning of the word, in which a

diffusive transition is defined as the one accompanied by an appearance of an amorphous phase or isolated atoms. The diffusionless transition modes in fact contribute to the mechanism of diffusion in the following sense. If we look at Figs.5-4 and 5-5, it is seen that, when cristobalite is compressed into the *Cmcm* phase followed by a decompression to the normal pressure, the system becomes an amorphous phase, in which the oxygen coordinations are topologically deformed from those in the starting cristobalite, although no isolated oxygens appear in the process. Thus, if we envisage a process in which the compressions and decompressions are repeated, this could result in a diffusion of atoms in the disordered phase. Since the local pressure is thought to fluctuate in a silica melt, we can expect such a diffusion in the liquid phase. Note that the diffusion considered here does not accompany isolated atoms but is regarded as local changes of Si-O coordination numbers, which will require much less energy than that needed for stripping an oxygen atom from a four-fold coordinated silicon atom. We shall elaborate this problem in the last chapter.

Chapter VI. Application to Magnesium Silicates

In this chapter, we shall describe our preliminary study on the application of our approach to magnesium silicates (MgSiO_3 , Mg_2SiO_4), the most abundant rock-forming material in the earth. Since the structure of magnesium silicates is close-packed as compared with the framework-structured silica, their structural stability is much less subtle. Thus there have been several empirical attempts for the interatomic potentials which can reproduce the structures or elasticity of the polymorphs precisely (Price and Parker, 1984; Matsui and Busing, 1984; Matsui, Akaogi and Matsumoto, 1987; Wall and Price, 1988). In this problem, non-empirical approaches so far exhibit rather poor accuracy in reproducing the structures if the approximations involved are crude. For instance, the modified electron gas approach, in which the electron density distribution in the crystal is approximately expressed by the sum of those in isolated ions, fails to reproduce the density by 20%, presumably because of the difficulty in treating oxygen ions in the theory (Wolf and Bukowinski, 1987). Here we derive the interatomic potentials for magnesium silicate from cluster calculations.

In going from SiO_2 to magnesium silicate, we have first to introduce the interatomic potential involving magnesium. For this purpose we have considered a linear $(\text{O-Mg-O})^{2-}$ cluster with two positive point charges for charge neutrality. $d(\text{O-e}^+)$ is again set equal to 1.65\AA . The potential energy surface for the symmetric stretching mode is shown in Fig.6-1 with full circles. The functional form as that described in Chapter II is employed for the interatomic potential.

The potential parameters for Si, O and Mg should be determined using the potential energy surfaces of both SiO_4^{4-} and MgO_2^{2-} clusters at the same time. This has to be done for MgSiO_3 and Mg_2SiO_4 , respectively, for the effective charge of each atom depends on the stoichiometry. As for the charge neutrality, we assume, as a first approximation, that the SiO_2 chemical unit is neutral. This implies that the charge on a magnesium atom is given as $Q_{\text{Mg}} = -Q_{\text{O}}$ for both

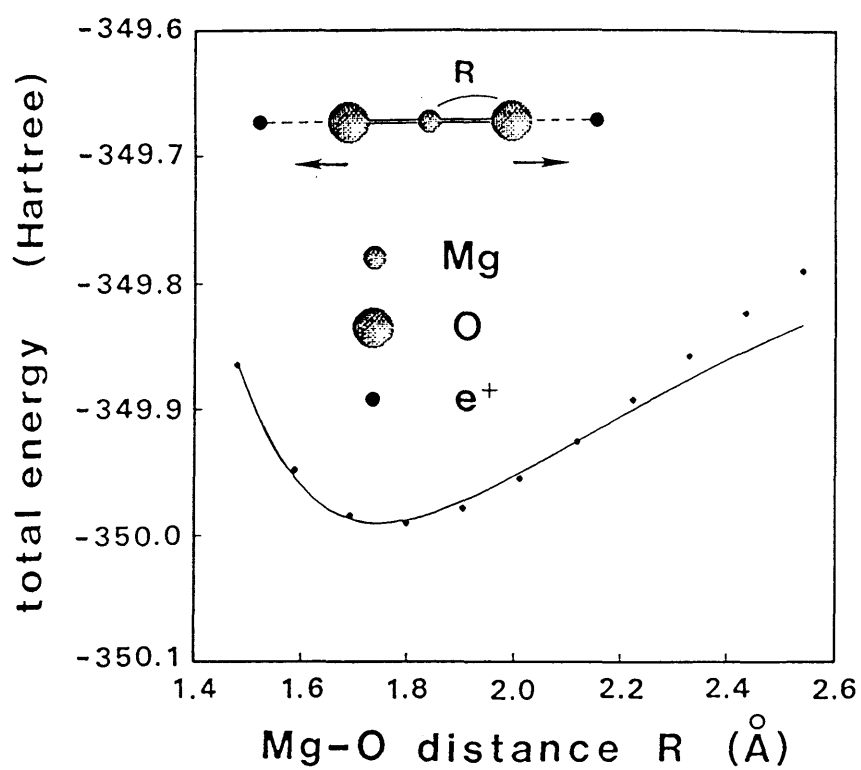


Fig.6-1 Total energy for the symmetrical-stretching deformation of a linear MgO_2^{2-} cluster shown in the insets. The full circles are the cluster calculation and the solid line is the fitted potential.

MgSiO_3 and Mg_2SiO_4 . Following the previous chapters, we assume $-Q_{\text{O}}=1.2e$.

We fit the potential surface, and, among several sets of parameters by non-linear least square fitting procedure, we have chosen the one which best agrees with the experimentally obtained density of orthoenstatite, a polymorph of MgSiO_3 . The parameters thus determined for Mg are, $Q_{\text{Mg}}=1.2e$, $a_{\text{Mg}}=0.7281\text{\AA}$, $b=0.01593\text{\AA}$, and $c_{\text{Mg}}=11.14\text{kcal}^{1/2}\text{\AA}^3\text{mol}^{-1/2}$. Here we employ, as a first approximation, the same potential parameters for Si and O as obtained for SiO_2 in Chapter II. The $1/r^6$ terms for Si-Si, Si-Mg and Mg-Mg pairs are neglected. The potential energy surface reproduced by the pair potential is shown with a solid line in Fig.6-1: we could not attain good agreement with the cluster calculation perhaps because the value of Q_{Mg} tentatively assumed here is not so appropriate.

Using these potential parameters, we have carried out the MD simulation of two polymorphs (forsterite (olivine), γ -spinel) of Mg_2SiO_4 and three polymorphs (orthoenstatite (orthopyroxene), ilmenite, perovskite) of MgSiO_3 (see the phase diagram in Fig.6-2). The structural parameters and the bulk moduli, K_0 (see eq.(3.9)), estimated by the compression simulation at 2.5GPa and 5GPa are summarized in Table 6-1 together with the trajectories of atomic positions in each polymorph in Fig.6-3(a)-(e). Detailed crystal data (fractional coordinates) are shown in Appendix C. In spite of rather rough determination of the potential parameters, the stability and the structural properties of these polymorphs are reproduced quite well by the pairwise interatomic potentials.

Although the overall agreement with experimental result is good, some deviations are seen in K_0 and K_0' for orthoenstatite. The error may in part come from the small numbers of pressure points used for the estimation of K_0 and K_0' . For orthoenstatite, we also notice that the position (y internal coordinate) of Mg2 at 8c site deviates from that observed experimentally (see Appendix C). We expect that a more precise and simultaneous determination of the potential parameters for Si, O and Mg would result in better agreement with

experimental results, which would also be useful to predict other structural properties.

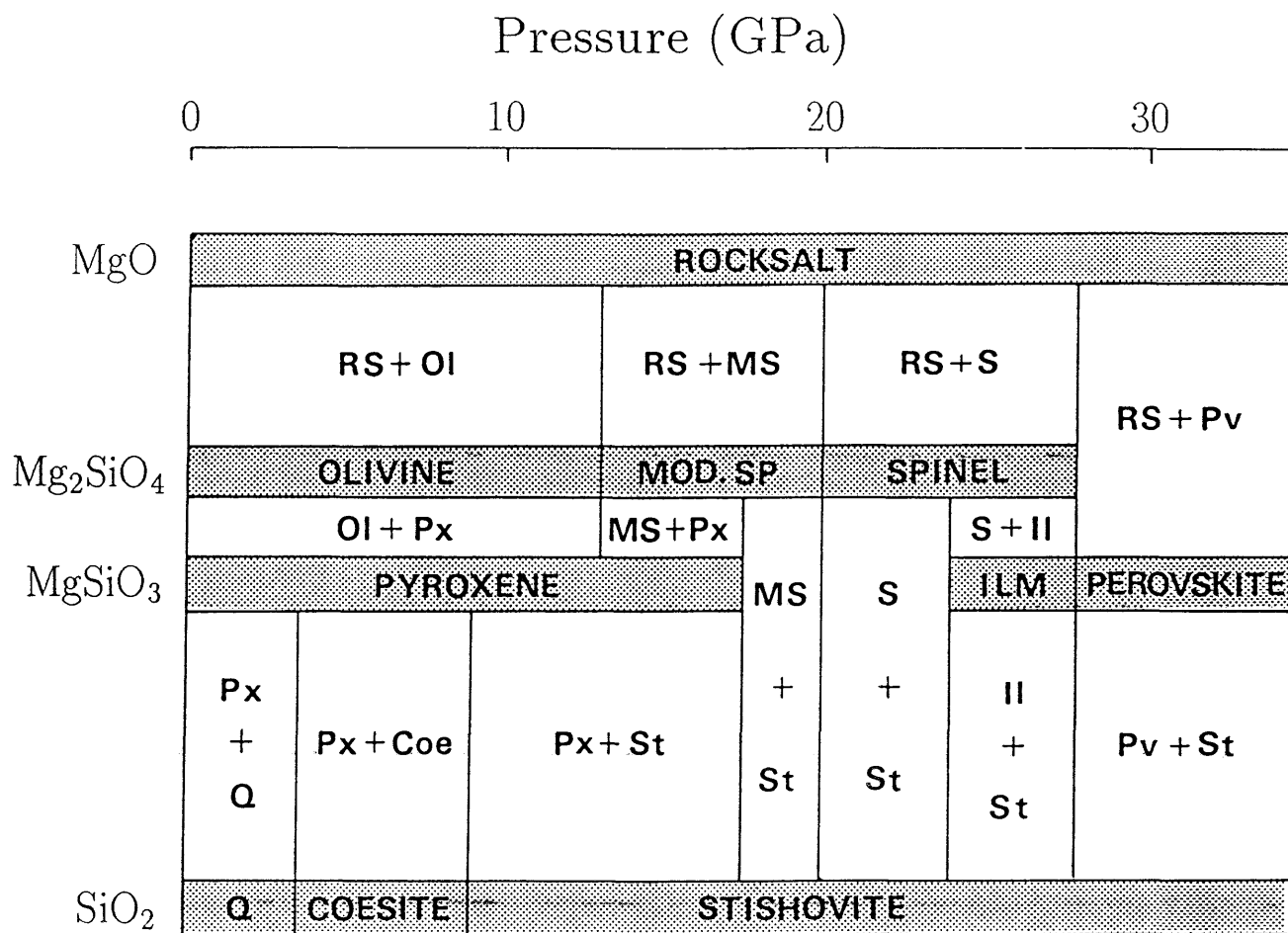


Fig.6-2 Schematic phase diagram of MgO-SiO₂ system on the pressure-composition plane. RS=ROCKSALT, Ol=OLIVINE, MS=MODIFIED SPINEL, S=SPINEL, Px=PYROXENE, Il=ILMENITE, Pv=PEROVSKITE, Q=QUARTZ, Coe=COESITE, St=STISHOVITE (after Akimoto, 1978).

Table 6-1 Structural parameters of magnesium silicates obtained by MD simulations as compared with experimental data. The space group *Pbnm* of forsterite and perovskite is represented as *Pnma* in the *International Tables for Crystallography* using a different setting of the unit cell axes.

Mg₂SiO₄

	forsterite		γ -spinel	
	Obs. ^a	This work	Obs. ^c	This work
Space Group	<i>Pbnm</i>	<i>Pbnm</i>	<i>Fd$\bar{3}m$</i>	<i>Fd$\bar{3}m$</i>
Z	4	4	8	8
a (Å)	4.75	4.753(4)	8.06	7.952(3)
b (Å)	10.19	9.797(14)	8.06	7.952(3)
c (Å)	5.98	5.779(10)	8.06	7.952(3)
Density (g/cm ³)	3.227	3.473(7)	3.563	3.718(1)
K ₀ (GPa)	127 ^b	151	184 ^d	222
K ₀ '	5.1	4.7	—	6.5
Energy (kcal/mol)		-2054.8(3)		-2074.1(1)

^aFujino et al. (1981).

^baverage of values from Graham et al.(1969) and Kumazawa et al. (1969).

^cSasaki, Prewitt et al. (1982). ^dWeidner et al. (1984).

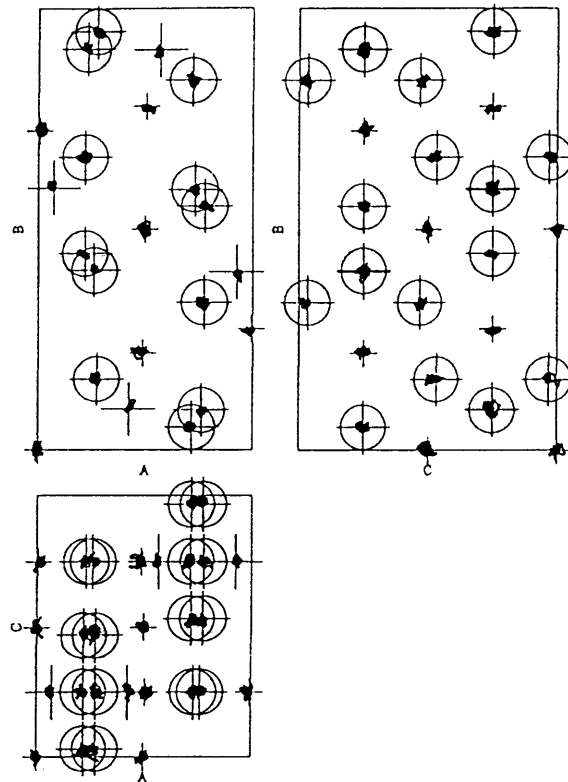
MgSiO₃

	orthoenstatite		ilmenite		perovskite	
	Obs. ^e	This work	Obs. ^g	This work	Obs. ⁱ	This work
Space Group	<i>Pbca</i>	<i>Pbca</i>	<i>R$\bar{3}$</i>	<i>R$\bar{3}$</i>	<i>Pbnm</i>	<i>Pbnm</i>
Z	16	16	6	6	4	4
a (Å)	18.230	18.27(4)	4.7284(4)	4.747(4)	4.775	4.715(4)
b (Å)	8.817	8.76(3)	4.7284(4)	4.747(4)	4.929	4.945(4)
c (Å)	5.181	5.21(3)	13.5591(1)	13.307(9)	6.897	6.973(6)
Density (g/cm ³)	3.203	3.20(2)	3.8098	3.852(5)	4.108	4.103(6)
K ₀ (GPa)	107 ^f	42	216 ^h	236.1	260(20) ^j	268
K ₀ '	5	29	—	6.26	—	5.0
Energy (kcal/mol)		-1646.94(11)		-1646.14(8)		-1649.6(1)

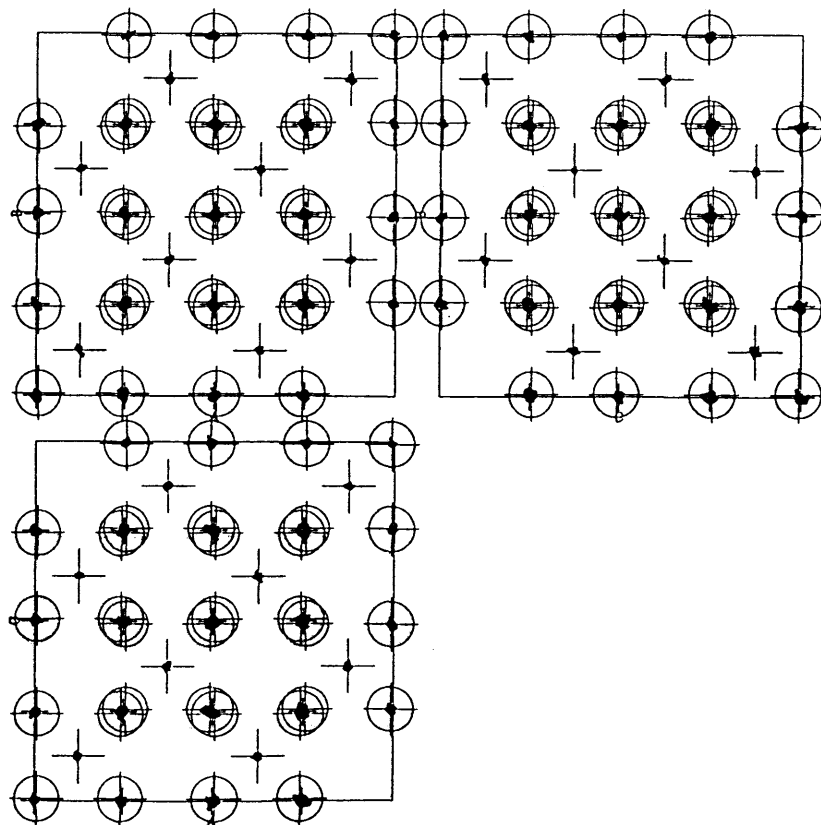
^eSasaki, Takeuchi et al. (1982). ^fWeidner et al. (1978). ^gHoriuchi et al. (1982).

^hWeidner et al. (1985). ⁱHoriuchi et al. (1986). ^jYagi et al. (1982).

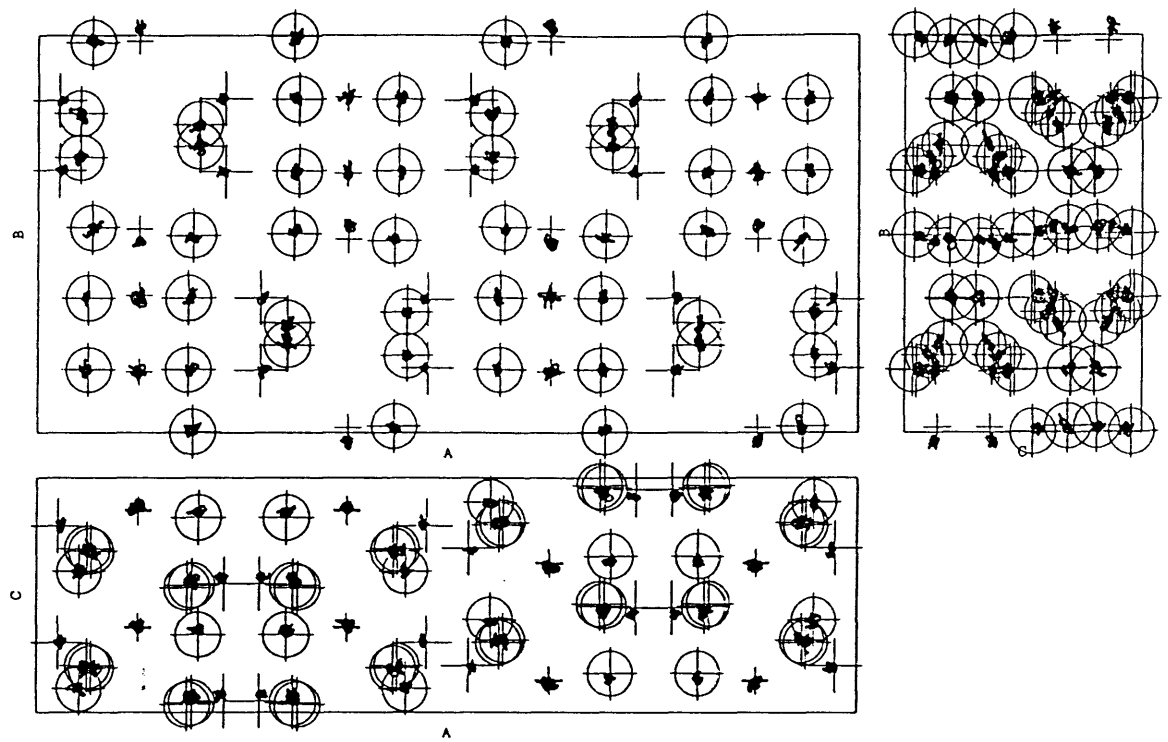
(a)



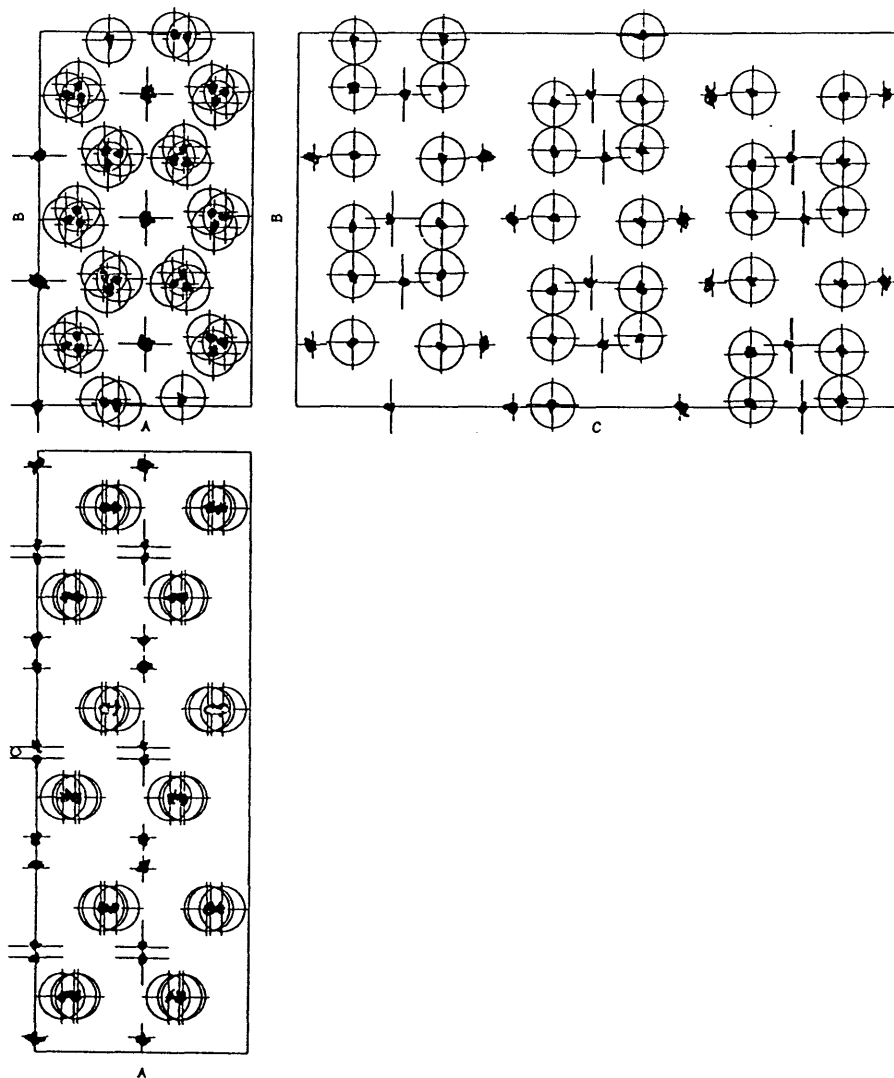
(b)



(c)



(d)



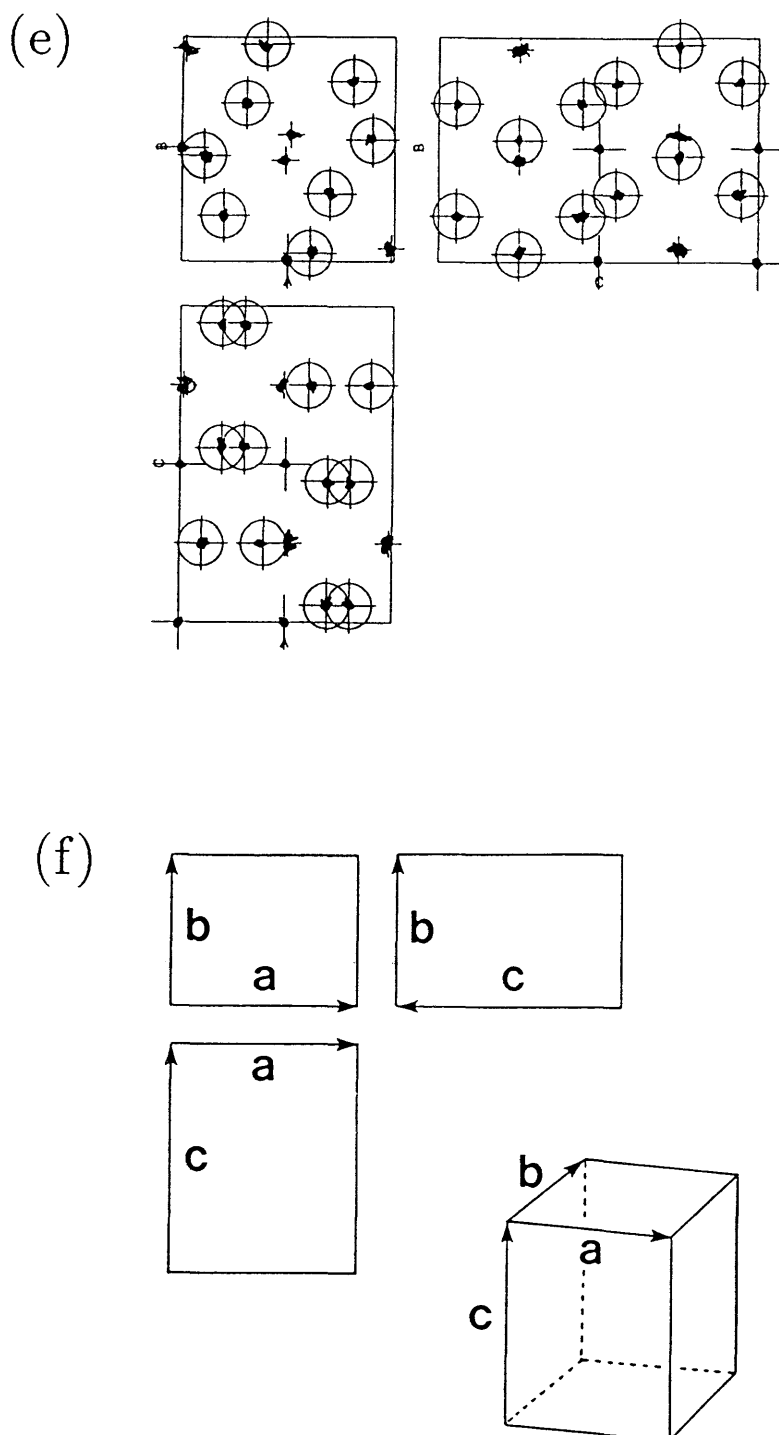


Fig.6-3 The trajectory (over 1 psec) of atomic positions in a unit cell (or a couple of unit cells in case of hexagonal system) projected to a-b, a-c and b-c planes for (a) forsterite, (b) γ -spinel, (c) orthoenstatite, (d) ilmenite and (e) perovskite. The positions of magnesium, silicon and oxygen atoms determined from experiments are shown with small crosses, large crosses, and large crosses plus circles, respectively. The projection planes are illustrated in (f).

Chapter VII. Concluding Remarks

Section 7.1. A conjecture respecting the anomalous diffusion property of silicate melt

In the discussion of Chapter V, we have briefly mentioned a relationship between the diffusionless transformation by compression and the atomic diffusion in silica melt. Before finishing the present thesis, we would like to discuss this problem in more detail and give a conjecture respecting the anomalous diffusion property of silicate melt under pressure.

First we summarize experimental results on the diffusion of silicate (aluminosilicate) melt under pressure. Since the viscosity of silicate is important as a dominant controlling factor during the passage of magma through the Earth, the pressure dependence of the viscosity or diffusion constants has been measured extensively since 1930's. More than a decade ago, it was found by Kushiro (1976) that the viscosity of $\text{NaAlSi}_2\text{O}_6$ (jadeite) decreases with increasing pressure contrary to what one might at first expect. A similar pressure dependence was also confirmed for other silicates of various compositions (Kushiro, 1980 and references therein). Judging from the fact that such pressure dependence is not observed for silicates which do not contain the framework structure of corner-linked SiO_4 tetrahedra due to insufficient amount of SiO_2 component (Kushiro, 1981), the anomalous pressure dependence can be considered as the inherent property of the SiO_2 framework. Thus we examine the diffusion property of silica melt.

As we mentioned in Chapter V, we expect that the atomic diffusion in silica melt is caused by the local fluctuation of the coordination number of silicon. Namely the rearrangement of the framework structure of corner-linked SiO_4 tetrahedra occurs by the *transient six-fold* coordination of silicon atoms, which results in the diffusion of framework-forming atoms. The dominant factor for the process is thus the activation energy needed for creating octahedrally coordinated silicon atoms. As seen from the fact that octahedrally coordinated

silicon atoms are stable in the high-pressure phase of crystalline silica and silicate, the activation energy should decrease as the pressure increases. More specifically, the atomic diffusivity is considered to increase up to the boundary pressure for which the four-fold and six-fold coordinations coexist in the equilibrium. Above that pressure, activation energy is needed for creating four-fold coordination, so that the diffusivity should decrease with pressure. Thus the diffusivity as a function of pressure is expected to have a maximum at the boundary pressure where four-fold and six-fold coordinations coexist. This is consistent with the MD results on the atomic diffusivity of $\text{NaAlSi}_2\text{O}_6$ by Angell, Cheeseman and Tamaddon (1982), where the diffusivities of oxygen and silicon atoms have maxima at the pressure when the average Si-O coordination number is five.

However, the microscopic mechanism of the pressure dependence of the diffusivity is not clear in the work by Angell et al., so that we propose a mechanism here in which the relative energy of four and six coordinations plays a crucial role, and perform an MD study of diffusion to test the picture in the following manner. As shown in Chapter V, the relative stability of four-fold and six-fold systems is sensitive to the atomic-radius ratio, $a_{\text{Si}}/a_{\text{O}}$. Thus we purposely vary this ratio to tune the relative stability to investigate the correlation of the stability (relative energy of two coordinations) and the diffusion constant of oxygen atoms. We consider three sets of potential parameters, where $a_{\text{Si}} = 0.87$, 0.86 and 0.85\AA , and the other parameters are fixed at the values used in Chapter V. The total energies of low-quartz, coesite and stishovite at room temperature and normal pressure are shown in Table 7-1 together with the energy difference of the most stable four-fold system (coesite, in this case) and the six-fold system (stishovite). To find the pressure at which the two phases coexist, we have to plot the free energy against volume for each phase to find the common tangent. To do so, we first approximate the Gibbs free energy, $E - TS + pV$, by the enthalpy, $E + pV$, neglecting the entropy differences. Here E is the total internal energy, which is tabulated in Table 7-1. The curvature of the

free energy against V around the minimum is calculated from the bulk modulus of the phase. Since the bulk modulus is rather insensitive to a_{Si} (see Chapter V), we can roughly estimate the transition (boundary) pressure of coesite and stishovite at room temperature using the common bulk moduli (about 100GPa for coesite and 300GPa for stishovite) for all the three values of a_{Si} . The transition pressure thus obtained are roughly $p_C = 6\text{GPa}$, 12GPa and $>21\text{GPa}$ for $a_{\text{Si}} = 0.87$, 0.86 and 0.85\AA , respectively.

The diffusivity of oxygen atoms, D , can be determined from the linear time-dependence of the mean square displacement of the atoms in the MD simulation using the Einstein's relation,

$$\langle r(t)^2 \rangle = 6Dt + \text{const},$$

where $\langle \rangle$ means the average over particles of the same species. The pressure dependence of D at 3000K is shown in Fig.7-1 for the three values of a_{Si} . In this result, several runs, each of which corresponds to 16psec, have been performed for each value of pressure and a_{Si} . Although the t -linearity of $\langle r^2 \rangle$ is approximately obeyed, the value of D is seen to fluctuate from one run to another. However, the overall feature is clear enough: as is expected, D increases with pressure (the viscosity decreases with pressure) in the lower pressure regime, while the diffusivity shows a maximum and then decreases above a critical pressure, which depends on the value of a_{Si} .

The critical pressure for each value of a_{Si} does indeed coincide with the boundary pressure, p_C , at which the four-coordinated and six-coordinated phases cross over as estimated above. The pressure for the maximum $D(p)$ is slightly larger than p_C estimated at room temperature, which may come from the fact that the critical pressure separating the coesite and stishovite is an increasing function of temperature (Yagi and Akimoto, 1976) as shown in Fig.1-2. Another possibility is that a four-coordinated amorphous phase may exist at high temperatures ($\sim 3000\text{K}$) between the two phases considered here, which can take

Table 7-1 Total energy of each polymorph at 300K for three types of potential parameters.

a_{Si} (Å)	Energy (kcal/mol)			Energy difference (kcal/mol) (stishovite)–(coesite)
	quartz	coesite	stishovite	
0.87	–1231.52	–1235.15	–1226.86	8.29
0.86	–1249.64	–1253.97	–1238.40	15.6
0.85	–1270.73	–1273.97	–1250.27	23.7

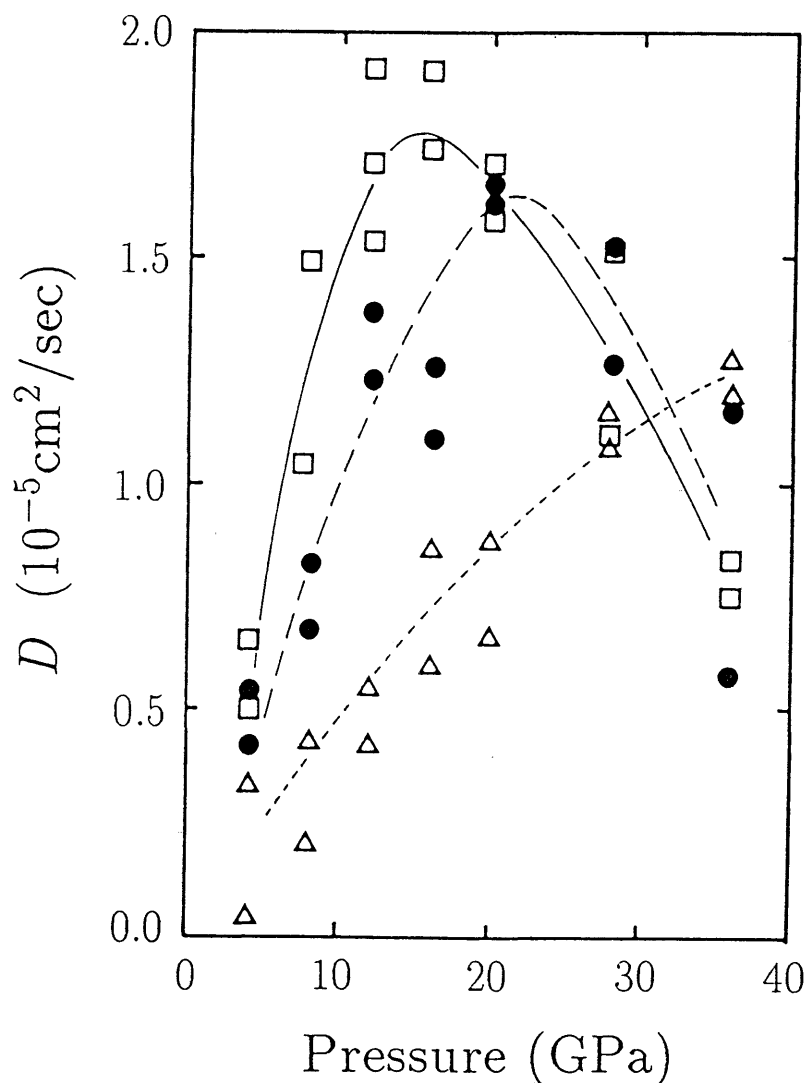


Fig.7-1 Pressure dependence of the diffusion coefficient of oxygen atoms at 3000K. Three kinds of symbols and lines correspond to three types of potential parameters: $a_{\text{Si}}=0.87$ (\square , ———), 0.86 (\bullet , - - - -), and 0.85 (\triangle , - · - · - ·) in A. The lines are guides to the eye.

part in the diffusion process. At any rate, there exists a conspicuous correlation between the pressure which gives the highest diffusivity and the critical pressure for the enthalpy crossover which separates four and six coordinations. Although the average coordination number at the pressure which maximizes D is five in agreement with the result of Angell et al. (1982), we should, according to our mechanism, regard this number as an averaged coordination number for the system with coexisting four and six coordinations.

In conclusion, we have provided and tested a conjecture respecting the diffusion process in silica and silicate melts: the atomic diffusion in these systems arises from the transient increase of the coordination number of silicon atoms which results in the rearrangement of the framework structure. The anomalous diffusion property is explained in a natural way by the model. More quantitative justification of the model is a future problem.

Section 7.2. Summary

Here we briefly summarize the results obtained in the present thesis.

We have determined the interatomic potential of silica from the first-principles cluster calculations. Despite the covalent character of the bonding in silica, potential energy surfaces for local deformations of the cluster have been fitted quite well by the sum of pairwise interatomic potentials. Only empirical factors in our approach are the configuration of the cluster and the final selection in the non-linear least-square fitting for the potential parameters with use of the information of the density and bulk modulus of low-quartz.

The pair potential is then used for the MD simulation of four polymorphs of silica. It has been shown for the first time that we can reproduce with common pair potentials virtually all the known polymorphs of silica (low-quartz, low-cristobalite, coesite and stishovite) in spite of the wide ranges of density ($2.3 - 4.2\text{g/cm}^3$) and bulk modulus ($18 - 296\text{GPa}$). This implies that the stability of

the local units (SiO_4 tetrahedra) and their space-filling are dominant factors in the stability of the whole crystalline structures even in the case of non-close-packed framework silica.

The pair potential is then applied to the simulation of thermally induced structural phase transition of quartz. The dynamical character of the high-temperature (β) phase is elucidated by the simulation: the phase transition has a peculiar dynamical character reminiscent of order-disorder type although the atomic distribution function averaged over long time mimics displacive transition. The thermal expansion is shown to be essential in this phase transition.

We have then turned to pressure-induced phase transitions of polymorphs at room temperature, where the pair potential is revised so that the energy difference between low-quartz and stishovite is reproduced. It is shown that, at room temperature, compression of crystalline silica results in the increase of the coordination number of silicon without diffusion process. We have predicted that there exist new high-pressure crystalline phases compressed from low-quartz and low-cristobalite which contain both four-fold and six-fold coordinated silicon atoms, although they cannot be quenched after decompression even at room temperature. The newly found diffusionless transitions are consistent with the mechanism suggested by Stolper and Ahrens. The increase of coordination number under pressure is shown to be related to the diffusion process with anomalous pressure dependence in silica and silicate melts .

We have also presented preliminary results on the application of our approach to magnesium silicates.

We have investigated the structural properties of silica in a first-principle approach. Although the cluster approach has inherent flaws that it does not necessarily reproduce the cohesive energy and that the determination of the long-range interaction (effective atomic charge) is subtle, the approach is very tractable, so that it should be applicable to a wide class of materials for

deriving interatomic potentials for MD simulations. In the case of silica, we have found that a pairwise functional form is sufficient to reproduce most properties of the polymorphs. Rigorously, of course, many-body potentials with three-atom, four-atom, ..., interactions should be required for the full description. And yet the promising results reported in this thesis indicate that the MD simulation supported by the cluster approach will be a powerful method to study or predict the structural properties of materials, including completely new materials, if they are carefully used, augmented by other complementary method like the bulk calculations if necessary. The present thesis constitutes, to the best of our knowledge, the first report which shows the validity of a first-principles approach starting from the cluster calculation for crystals other than molecular crystals.

Appendix A. Crystal data of polymorphs of silica

Table A-1 Detailed structural parameters obtained by MD simulations as compared with experimental results for various polymorphs of silica. Estimated standard errors in observed (Obs.) data and thermal fluctuations in MD data are given in parentheses in units of the last decimal place stated.

(a) low-quartz

coordinates of atoms

			Obs. ^a	This work
atom	position			
Si	3a	x	0.4697(1)	0.461(19)
		y	0	0.000(17)
		z	0	0.000(13)
O	6c	x	0.4135(3)	0.426(25)
		y	0.2669(2)	0.276(22)
		z	0.1191(2)	0.122(17)

interatomic distances and bond angles

			Obs. ^a	This work
Intra-tetrahedral distances (Å)				
Si-O ($\times 2$)			1.605(1)	1.627
Si-O ($\times 2$)			1.614(1)	1.640
$\langle \text{Si} - \text{O} \rangle$			1.6092(7)	1.634
O-O ($\times 2$)				
O-O ($\times 1$)			2.645(1)	2.645
O-O ($\times 1$)			2.631(2)	2.682
O-O ($\times 2$)			2.6171(7)	2.636
O-O ($\times 1$)			2.612(2)	2.754
$\langle \text{O} - \text{O} \rangle$			2.626	2.667
Inter-tetrahedral distances (Å)				
O-O			3.331(2)	3.461
O-O			3.411(1)	3.453
Intra-tetrahedral angles (deg)				
O-Si-O ($\times 2$)			110.52(6)	108.1
O-Si-O ($\times 2$)			108.81(2)	107.6
O-Si-O ($\times 1$)			108.93(9)	115.7
O-Si-O ($\times 1$)			109.24(8)	109.7
$\langle \text{O} - \text{Si} - \text{O} \rangle$			109.38	109.5
Inter-tetrahedral angles (deg)				
Si-O-Si			143.73(7)	147.3

(b) low-cristobalite

coordinates of atoms

			Obs. ^b	This work
atom	position			
Si	4a	x	0.3002(1)	0.328(15)
		y	0.3002(1)	0.328(14)
		z	0	0.000(12)
O	8b	x	0.2394(5)	0.234(22)
		y	0.1049(4)	0.136(14)
		z	0.1785(3)	0.189(15)

interatomic distances and bond angles

			Obs. ^b	This work
Intra-tetrahedral distances (Å)				
Si-O ($\times 2$)			1.605(2)	1.644
Si-O ($\times 2$)			1.613(2)	1.625
$\langle \text{Si} - \text{O} \rangle$			1.609	1.635
O-O ($\times 1$)				
O-O ($\times 2$)			2.656(4)	2.603
O-O ($\times 2$)			2.633(3)	2.689
O-O ($\times 2$)			2.600(1)	2.641
O-O ($\times 1$)			2.620(4)	2.739
$\langle \text{O} - \text{O} \rangle$			2.624	2.667
Inter-tetrahedral distances (Å)				
O-O			3.688	3.476
Intra-tetrahedral angles (deg)				
O-Si-O ($\times 1$)			111.7(2)	104.8
O-Si-O ($\times 2$)			110.0(1)	110.7
O-Si-O ($\times 2$)			108.0(1)	107.7
O-Si-O ($\times 1$)			109.1(2)	114.8
$\langle \text{O} - \text{Si} - \text{O} \rangle$			109.7	109.4
Inter-tetrahedral angles (deg)				
Si-O-Si			146.4(1)	142.7

^bPeacor (1973)

^aLevien et al. (1980)

(c) coesite

coordinates of atoms

			Obs. ^c	This work
atom	position			
Si1	8f	x	0.14033(7)	0.131(15)
		y	0.10833(3)	0.109(05)
		z	0.07227(8)	0.068(11)
Si2	8f	x	0.50682(7)	0.501(14)
		y	0.15799(4)	0.155(05)
		z	0.54077(7)	0.540(10)
O1	4a	x	0	0.000(18)
		y	0	0.000(05)
		z	0	0.000(13)
O2	4e	x	0.5	0.500(16)
		y	0.1163(1)	0.119(06)
		z	0.75	0.750(10)
O3	8f	x	0.2660(2)	0.274(17)
		y	0.1234(1)	0.125(07)
		z	0.9401(2)	0.954(14)
O4	8f	x	0.3114(2)	0.305(19)
		y	0.1038(1)	0.108(07)
		z	0.3282(2)	0.321(11)
O5	8f	x	0.0172(2)	0.013(20)
		y	0.2117(1)	0.216(05)
		z	0.4782(2)	0.478(15)

interatomic distances and bond angles

			Obs. ^c	This work
Intra-tetrahedral distances (Å)				
Si1-O1 (×1)			1.5945(4)	1.609
Si1-O3 (×1)			1.611(1)	1.645
Si1-O4 (×1)			1.612(1)	1.647
Si1-O5 (×1)			1.619(1)	1.646
⟨Si1 – O⟩			1.6092(6)	1.637
O1-O3 (×1)			2.634(1)	2.696
O1-O4 (×1)			2.616(1)	2.662
O1-O5 (×1)			2.630(1)	2.765
O3-O4 (×1)			2.646(2)	2.632
O3-O5 (×1)			2.611(2)	2.638
O4-O5 (×1)			2.628(2)	2.621
⟨O – O⟩			2.628	2.669

Si2-O4 (×1)	1.604(1)	1.626
Si2-O2 (×1)	1.6109(7)	1.626
Si2-O3 (×1)	1.614(1)	1.643
Si2-O5 (×1)	1.619(1)	1.655
⟨Si2 – O⟩	1.6118(6)	1.638
O4-O2 (×1)	2.623(1)	2.747
O4-O3 (×1)	2.617(2)	2.625
O4-O5 (×1)	2.630(2)	2.641
O2-O3 (×1)	2.637(1)	2.732
O2-O5 (×1)	2.649(2)	2.673
O3-O5 (×1)	2.637(2)	2.607
⟨O – O⟩	2.632	2.671

Inter-tetrahedral distances (Å)

O3-O4	2.982	3.177
O3-O5	3.063	3.251
O4-O5	3.102	3.193
O1-O3	3.136	3.315

Intra-tetrahedral angles (deg)

O1-Si1-O3 (×1)	110.52(6)	111.9
O1-Si1-O4 (×1)	109.32(5)	109.7
O1-Si1-O5 (×1)	109.89(5)	116.3
O3-Si1-O4 (×1)	110.32(7)	106.2
O3-Si1-O5 (×1)	107.89(7)	106.6
O4-Si1-O5 (×1)	108.87(7)	105.5
⟨O – Si1 – O⟩	109.47	109.4

O4-Si2-O2 (×1)	109.35(6)	115.3
O4-Si2-O3 (×1)	108.85(7)	106.8
O4-Si2-O5 (×1)	109.38(7)	107.2
O2-Si2-O3 (×1)	109.74(6)	113.4
O2-Si2-O5 (×1)	110.21(8)	109.1
O3-Si2-O5 (×1)	109.30(7)	104.4
⟨O – Si2 – O⟩	109.47	109.4

Inter-tetrahedral angles (deg)

Si1-O1-Si1	180.	180.0
Si2-O2-Si2	142.7(1)	147.6
Si2-O3-Si1	144.52(9)	151.9
Si1-O4-Si2	149.64(9)	155.3
Si1-O5-Si2	137.36(9)	143.9

^cLevien et al. (1981)

(d) stishovite

coordinates of atoms

				Obs. ^d	This work
atom	position				
Si	2a	x	0		0.000(11)
		y	0		0.000(11)
		z	0		0.000(13)
O	4f	x	0.30616(4)		0.305(10)
		y	0.30616(4)		0.305(10)
		z	0		0.000(15)

interatomic distances and bond angles

				Obs. ^d	This work
--	--	--	--	-------------------	-----------

Intra-octahedral distances (Å)

Si-O (×4)	1.7572(1)	1.813
Si-O (×2)	1.8087(2)	1.840
⟨Si - O⟩	1.7744	1.822

O-O (×2) 2.2903(3) 2.360

O-O (×8) 2.5217(1) 2.583

O-O (×2) 2.6655(1) 2.753

Inter-octahedral distances (Å)

O-O 3.0274 3.091

Intra-octahedral angles (deg)

O-Si-O (×2) 81.34(1) 81.2

O-Si-O (×8) 90. 90.0

O-Si-O (×2) 98.66(1) 98.8

Inter-octahedral angles (deg)

Si-O-Si (×1) 98.66(1) 98.8

Si-O-Si (×2) 130.67(1) 130.6

(e) $Pa\bar{3}$ silica

coordinates of atoms

				FLAPW ^e	This work
atom	position				
Si	4a	x	0		0.000(11)
		y	0		0.000(11)
		z	0		0.000(11)
O	8c	x	0.344		0.337(11)
		y	0.344		0.337(11)
		z	0.344		0.337(11)

interatomic distances and bond angles

				FLAPW ^e	This work
--	--	--	--	--------------------	-----------

Intra-octahedral distances (Å)

Si-O (×6) 1.827 1.863

O-O (×6) 2.388 2.415

O-O (×6) 2.765 2.838

Inter-octahedral distances (Å)

O-O 2.416 2.583

Intra-octahedral angles (deg)

O-Si-O (×6) 81.6 80.8

O-Si-O (×6) 98.4 99.2

Inter-octahedral angles (deg)

Si-O-Si (×3) 119.8 120.0

^eTheoretical result by Park et al. (1988)^dHill et al. (1983)

Table A-2 Pressure dependence of coordinates of atoms as compared with experimental results for quartz and coesite. Estimated standard errors in observed (Obs.) data and thermal fluctuations in MD data are given in parentheses in units of the last decimal place stated.

(a) low-quartz

			Obs. ^a			This work		
			1 atm	4.86 GPa	difference	1 atm	4.86 GPa	difference
atom	position							
Si	3a	x	0.4697(1)	0.4551(2)	-0.0146	0.461(19)	0.442(19)	-0.019
		y	0	0	0	0.000(17)	0.000(18)	0.000
		z	0	0	0	0.000(13)	0.000(14)	0.000
O	6c	x	0.4135(3)	0.4061(6)	-0.0129	0.426(25)	0.413(23)	-0.013
		y	0.2669(2)	0.2912(5)	0.0233	0.276(22)	0.299(21)	0.023
		z	0.1191(2)	0.1012(3)	-0.0179	0.122(17)	0.107(16)	-0.016

^aLevien et al. (1980)

(b) coesite

			Obs. ^b			This work		
			1 atm	4.60 GPa	difference	1 atm	4.60 GPa	difference
atom	position							
Si1	8f	x	0.14033(7)	0.1370(1)	-0.0033	0.131(15)	0.127(15)	-0.005
		y	0.10833(3)	0.1098(3)	0.0015	0.109(05)	0.111(04)	0.002
		z	0.07227(8)	0.0704(2)	-0.0019	0.068(11)	0.064(11)	-0.004
Si2	8f	x	0.50682(7)	0.5085(2)	0.0017	0.501(14)	0.503(14)	0.002
		y	0.15799(4)	0.1576(3)	-0.0004	0.155(05)	0.153(05)	-0.001
		z	0.54077(7)	0.5441(2)	0.0033	0.540(10)	0.544(09)	0.004
O1	4a	x	0	0	0	0.000(18)	0.000(19)	0.000
		y	0	0	0	0.000(05)	0.000(04)	0.000
		z	0	0	0	0.000(13)	0.000(13)	0.000
O2	4e	x	0.5	0.5	0	0.500(16)	0.500(16)	0.000
		y	0.1163(1)	0.1091(8)	-0.0072	0.119(06)	0.113(05)	-0.007
		z	0.75	0.75	0	0.750(10)	0.750(10)	0.000
O3	8f	x	0.2660(2)	0.2543(4)	-0.0117	0.274(17)	0.262(15)	-0.012
		y	0.1234(1)	0.1291(5)	0.0057	0.125(07)	0.130(07)	0.005
		z	0.9401(2)	0.9284(4)	-0.0031	0.954(14)	0.941(10)	-0.012
O4	8f	x	0.3114(2)	0.3179(4)	0.0065	0.305(19)	0.310(18)	0.005
		y	0.1038(1)	0.1006(6)	-0.0032	0.108(07)	0.106(07)	-0.002
		z	0.3282(2)	0.3251(4)	-0.0031	0.321(11)	0.319(10)	-0.002
O5	8f	x	0.0172(2)	0.0264(5)	0.0092	0.013(20)	0.022(19)	0.009
		y	0.2117(1)	0.2129(6)	0.0012	0.216(05)	0.217(05)	0.001
		z	0.4782(2)	0.4719(5)	-0.0063	0.478(15)	0.474(15)	-0.004

^bLevien et al. (1981)

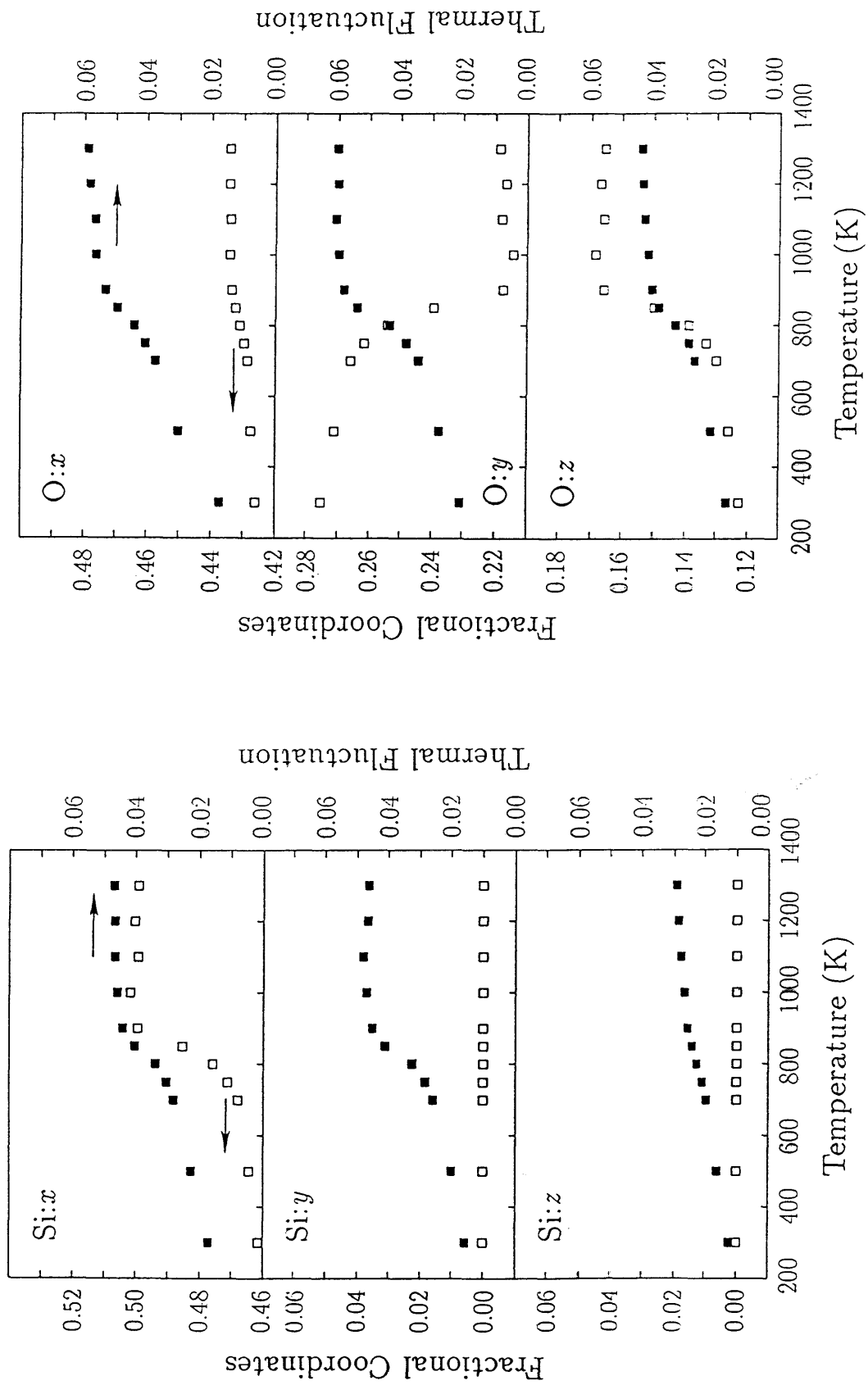


Fig.A-1 Temperature dependences of the fractional coordinates of atoms (open squares) (see Chapter IV) and their thermal fluctuations (full squares) in quartz obtained by the MD simulations using 432 particles. Si:x (u parameter in Chapter IV) and O:y and z coordinates clearly show a phase transition around $T_c = 850-900$ K.

Appendix B. Pressure-induced structural transformations

Here we show the time-sequence of the pressure-induced structural transformations of silica discussed in Chapter V. The transformation of low-cristobalite into the *Cmcm* phase is shown in Fig.B-1. When the *Cmcm* phase is decompressed, it becomes unstable resulting in an amorphous phase as shown in Fig.B-2. The second transformation observed in the compression experiment of low-cristobalite, *i.e.*, the transformation from the *Cmcm* phase into stishovite is shown in Fig.B-3.

The transformation of low-quartz into the α -PbO₂ structure is shown in Fig.B-4. When decompressed, the α -PbO₂ structure including some defects transforms into an amorphous phase in which almost all the silicon atoms are tetrahedrally coordinated as shown in Fig.B-5.

In the figures, full circles represent silicon atoms and small points dressed with large, shaded circles represent oxygen atoms. The bonds between silicon and oxygen are connected when the interatomic distance is less than 2.16Å. The instantaneous pressure, temperature and density of the system are shown at the next to the bottom line of each panel. Because of fluctuations, these values do not necessarily agree with the external pressure and temperature specified. The number in the bottom line is the MD step, where one MD step corresponds to 2 fsec.

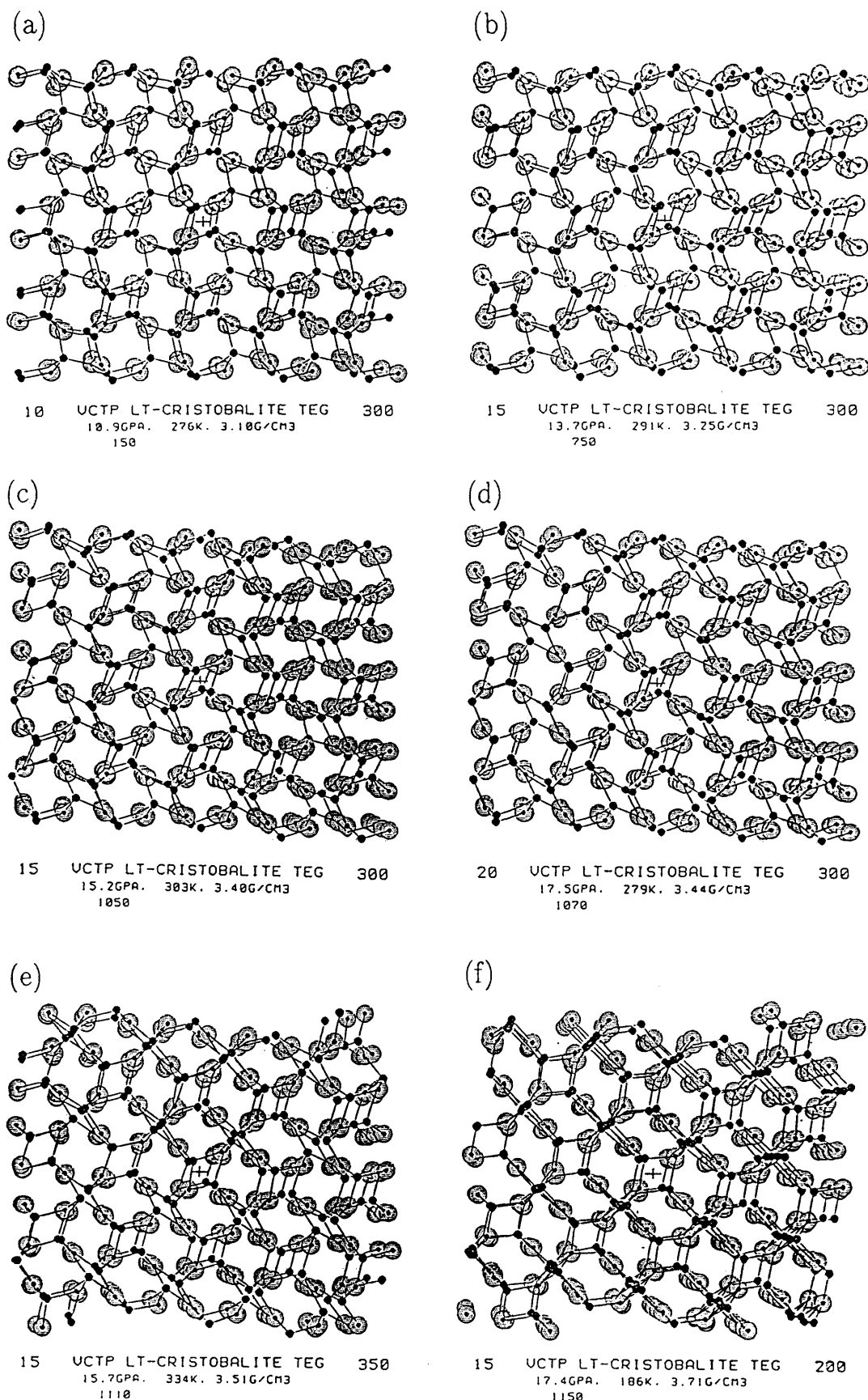


Fig.B-1 Compression of low-cristobalite: (a) Low-cristobalite at 10GPa and (b)-(f) the structural transformation of low-cristobalite into the *Cmcm* structure at around 17GPa.

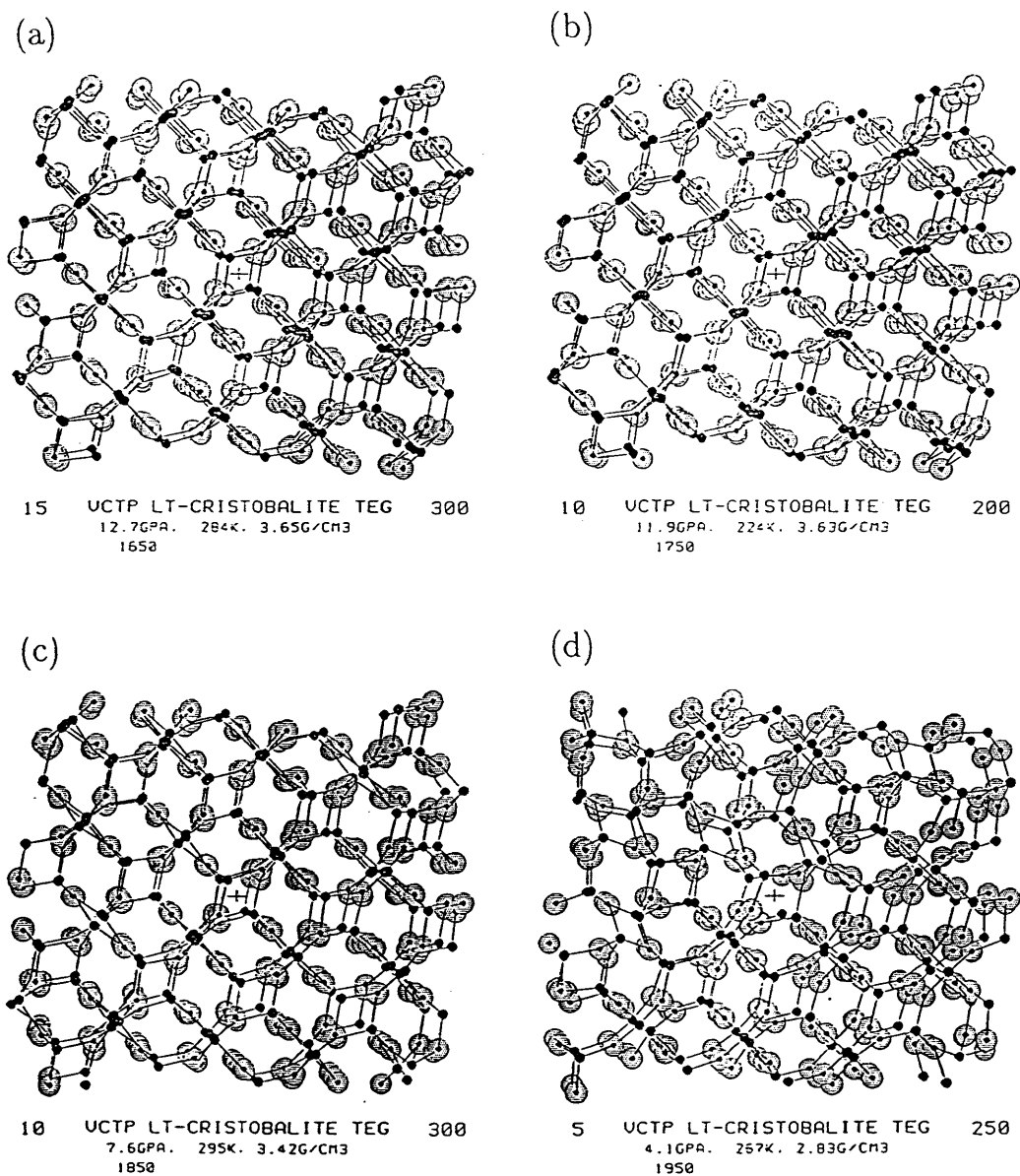


Fig.B-2 Decompression of the *Cmcm* phase (a)-(d). The system has not reached an equilibrium state even in the last panel (d), where the top-left side is in the low-cristobalite phase and some part is still in the *Cmcm* phase. The final structure is an amorphous phase in which the connectivity of the SiO_4 network has somewhat changed from the original low-cristobalite (see Fig.5-5(b)).

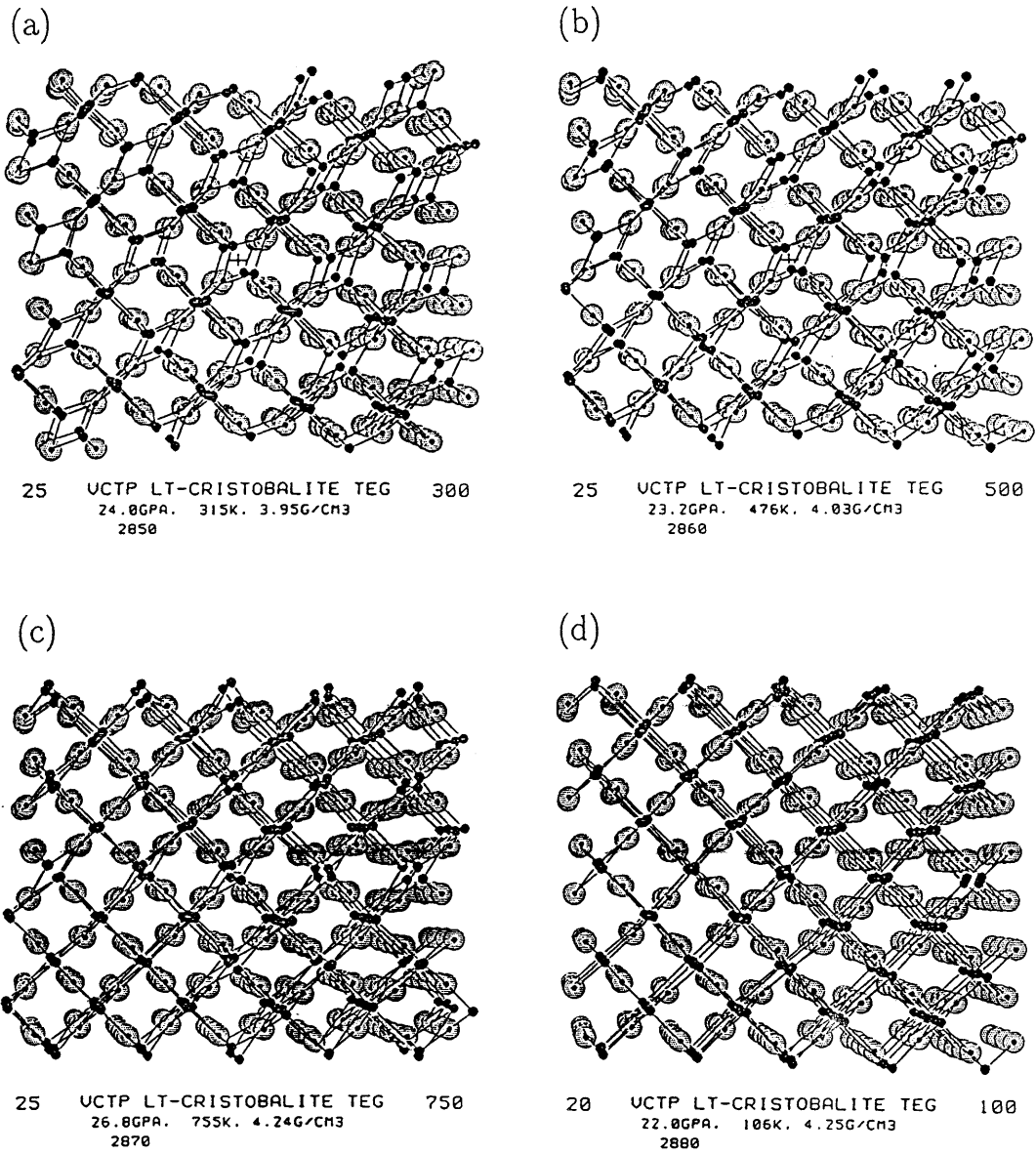


Fig.B-3 Compression of the *Cmcm* phase (a)-(d). The final structure (d) is exactly stishovite including no defects. The transformation occurs within a very short period of time.

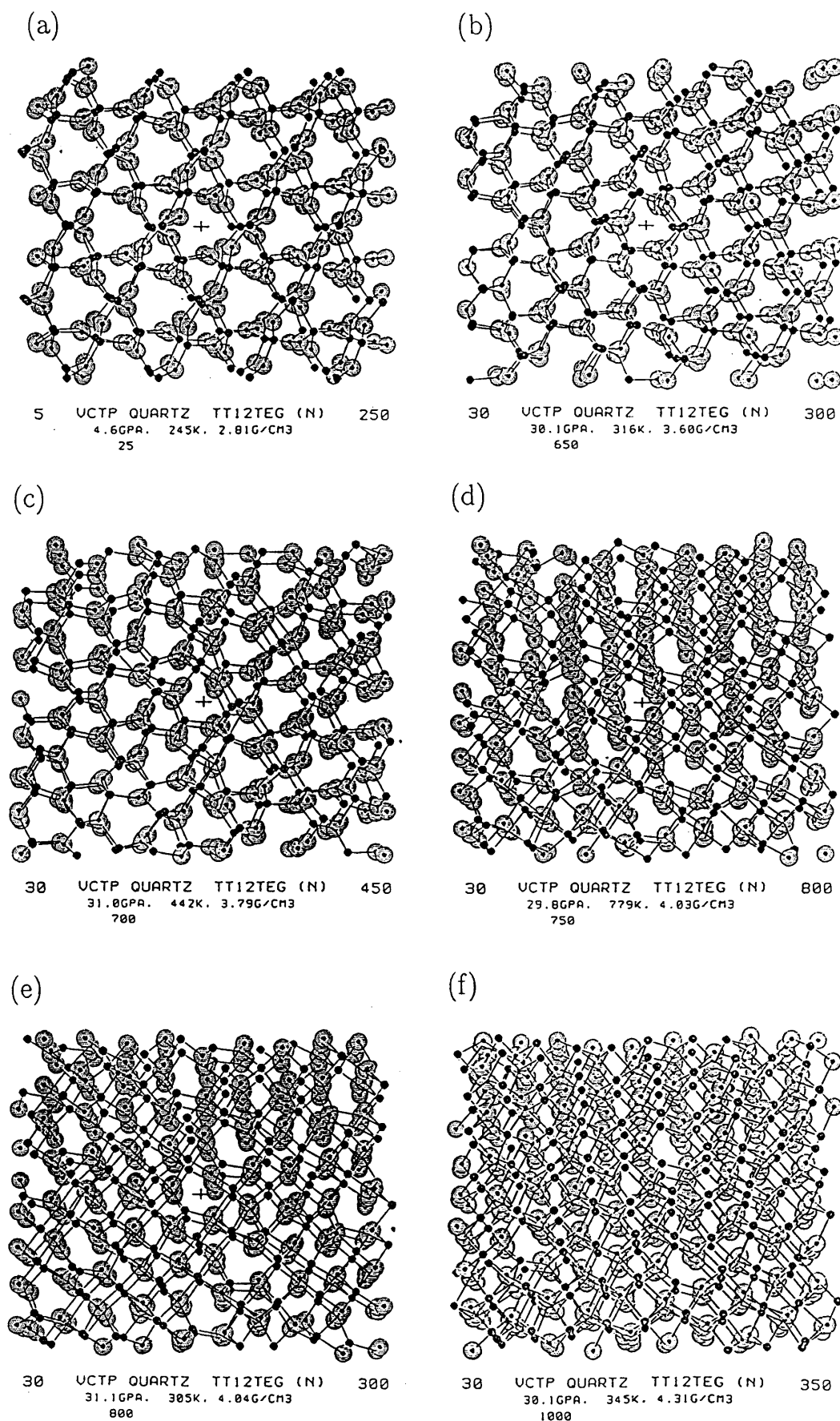


Fig.B-4 Compression of low-quartz: (a) Low-quartz at 5GPa and (b)-(f) the structural transformation of low-quartz into the α -PbO₂ structure with some defects.

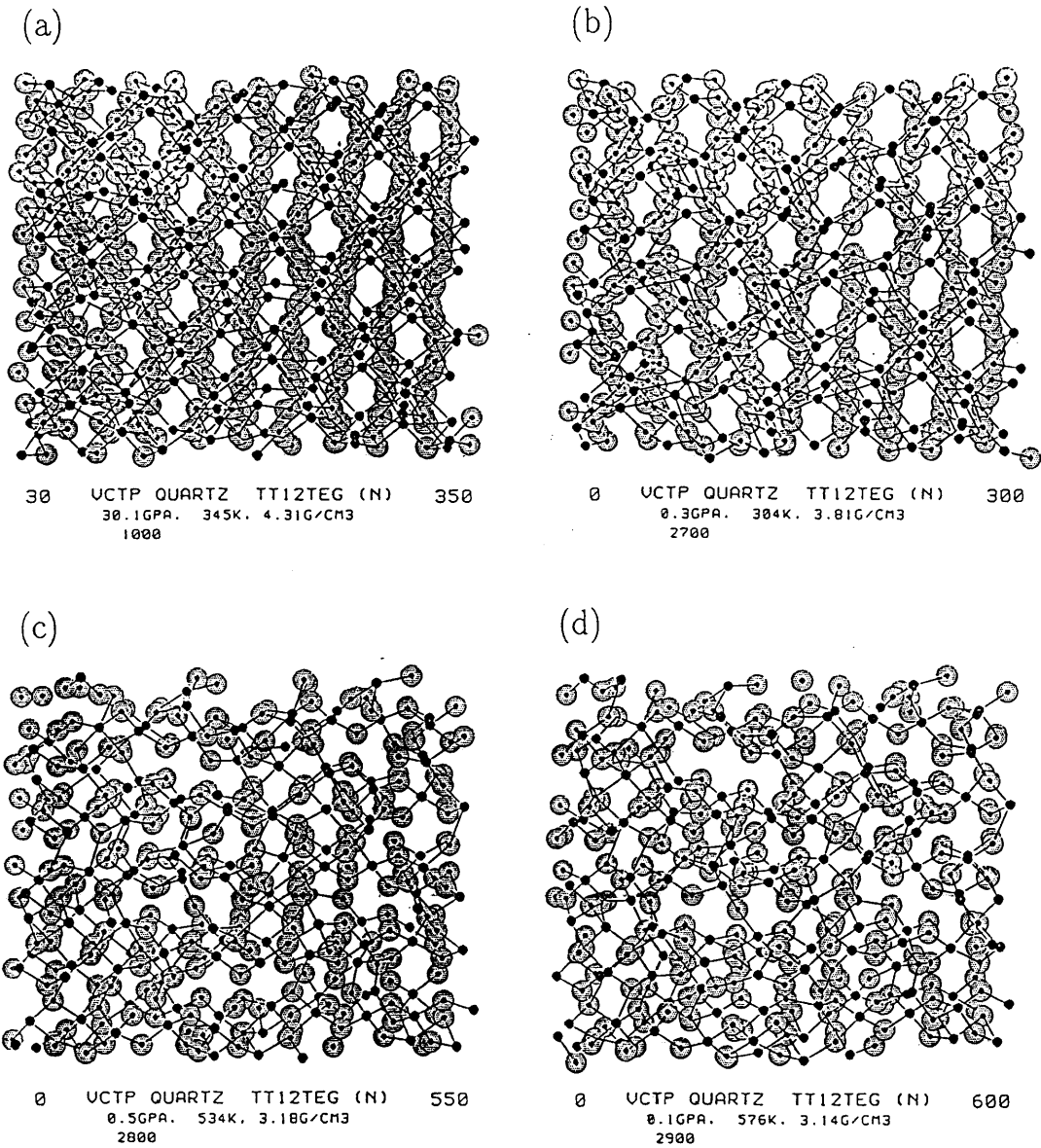


Fig.B-5 Decompression of the α -PbO₂ phase with defects: (a) the same structure as Fig.B-4(f) seen from a different direction and (b)-(d) the transformation of the α -PbO₂ structure into an amorphous phase where almost all the silicon atoms are tetrahedrally coordinated. In this simulation, partly because the simulation time for annealing was too short, the α -PbO₂ structure persisted until the external pressure was decreased to normal pressure. Thus the transformation (b)-(d) occurred at normal pressure.

Appendix C. Crystal data of polymorphs of magnesium silicate

Table C-1 Fractional coordinates of atoms in polymorphs of magnesium silicate obtained by MD simulations as compared with experimental results.

(a) forsterite

			Obs. ^a	This work
atom	position			
Mg1	4a	x	0	0.000(6)
		y	0	0.000(4)
		z	0	0.000(9)
Mg2	4c	x	0.9917	0.982(8)
		y	0.2774	0.273(5)
		z	0.25	0.250(6)
Si	4c	x	0.4265	0.434(5)
		y	0.0940	0.100(3)
		z	0.25	0.250(8)
O1	4c	x	0.7659	0.770(5)
		y	0.0916	0.088(3)
		z	0.25	0.250(5)
O2	4c	x	0.2216	0.215(6)
		y	0.4471	0.445(3)
		z	0.25	0.250(6)
O3	8d	x	0.2775	0.273(5)
		y	0.1631	0.164(3)
		z	0.0330	0.025(2)

^aFujino et al. (1981)

(b) γ -spinel

			Obs. ^b	This work
atom	position			
Mg	16d	x	0.5	0.500(1)
		y	0.5	0.500(1)
		z	0.5	0.500(2)
Si	8a	x	0.125	0.125(2)
		y	0.125	0.125(2)
		z	0.125	0.125(2)
O	32e	x	0.2434	0.245(1)
		y	0.2434	0.245(1)
		z	0.2434	0.245(1)

^bSasaki et al. (1982)

(c) orthoenstatite

			Obs. ^c	This work
atom	position			
Mg1	8c	x	0.3758	0.376(2)
		y	0.6538	0.655(4)
		z	0.8660	0.876(6)
Mg2	8c	x	0.3768	0.377(2)
		y	0.4870	0.522(4)
		z	0.3590	0.373(6)
Si1	8c	x	0.2717	0.275(2)
		y	0.3416	0.342(2)
		z	0.0504	0.078(4)
Si2	8c	x	0.4736	0.470(1)
		y	0.3373	0.338(2)
		z	0.7983	0.806(7)
O1A	8c	x	0.1834	0.187(2)
		y	0.3400	0.342(3)
		z	0.0346	0.059(5)
O2A	8c	x	0.3109	0.312(2)
		y	0.5023	0.509(2)
		z	0.0433	0.066(6)
O3A	8c	x	0.3031	0.304(2)
		y	0.2226	0.227(4)
		z	0.8319	0.854(5)
O1B	8c	x	0.5624	0.560(1)
		y	0.3404	0.341(3)
		z	0.8000	0.806(5)
O2B	8c	x	0.4328	0.431(1)
		y	0.4831	0.487(3)
		z	0.6898	0.686(6)
O3B	8c	x	0.4476	0.448(2)
		y	0.1950	0.487(3)
		z	0.6036	0.686(6)

^cSasaki et al. (1982)

(d) ilmenite

			Obs. ^d	This work
atom	position			
Mg	6c	x	0	0.000(3)
		y	0	0.000(3)
		z	0.3597	0.356(1)
Si	6c	x	0	0.000(2)
		y	0	0.000(1)
		z	0.1577	0.155(1)
O	18f	x	0.3214	0.306(1)
		y	0.0361	0.019(2)
		z	0.2408	0.241(1)

^dHoriuchi et al. (1982)

(e) perovskite

			Obs. ^e	This work
atom	position			
Mg	4c	x	0.5141	0.520(6)
		y	0.5560	0.555(8)
		z	0.25	0.250(6)
Si	4b	x	0.5	0.500(4)
		y	0	0.000(5)
		z	0	0.000(3)
O1	4c	x	0.1028	0.114(6)
		y	0.4660	0.460(5)
		z	0.25	0.250(3)
O2	8d	x	0.1961	0.197(4)
		y	0.2014	0.201(4)
		z	0.5531	0.558(2)

^eHoriuchi et al. (1986)

References

- Akimoto, S., in *Material Science of the Earth I – The World of High Pressure and High Temperature* –, Chapter 3 (eds. S. Akimoto and H. Mizutani), Iwanami: Earth Science 2 (Iwanami, Japan, 1978), in Japanese.
- Allan, D.C. & Teter, M.P., *Phys. Rev. Lett.* **59**, 1136(1987).
- Anders, E. & Ebihara, M., *Geochim. Cosmochim. Acta* **46**, 2363(1982).
- Angell, C.A., Cheeseman, P.A. & Tamaddon, S., *Science*, **218**, 885(1982).
- Axe, J.D. & Shirane, G., *Phys. Rev.* **B1**, 342(1983).
- Barron, T.H.K., Huang, C.c. & Pasternak, A., *J. Phys. C: Solid St. Phys.* **9**, 3925(1976).
- Baur, W.H., *Acta Crystallogr.* **B33**, 2615(1977).
- Bell, R.J. & Dean, P., *Phil. Mag.* **25**, 1381(1972).
- Billesbach, D.P., Edwardson, P.J. & Hardy, J.R., *Phys. Rev.* **B37**, 236(1988).
- Biswas, R. & Hamman, D.R., *Phys. Rev.* **B36**, 6434(1987).
- Bukowinski, M.S.T. & Wolf, G.H., *J. Geophys. Res.* **91**, 4704(1986).
- Busing, W.R., WMIN, Oak Ridge National Laboratory, Report No. ORNL-5747, Oak Ridge (1981).
- Busing, W.R. & Matsui, M., *Acta Crystallogr. Sect.A* **40**, 532(1984).
- Car, R. & Parrinello, M., *Phys. Rev. Lett.* **55**, 2471(1985).
- Carlsson, A.E., Ashcroft, N.W. & Williams, A.R., *Geophys. Res. Lett.* **11**, 617(1984).
- Carravetta, V. & Clementi, E., *J. Chem. Phys.* **81**, 2646(1984).
- Catlow, C.R.A., Dixon, M. & Mackrodt, W.C., in *Computer Simulations of Solids* (ed. Catlow, C.R.A. & Mackrodt, W.C.) *Lecture Notes in Physics* vol.166 (Berlin, Springer, 1982) p.130.
- Catlow, C.R.A., Freeman, C.M. & Royle, R.L., *Physica* **131B**, 1(1985).
- Catlow, C.R.A. & Norgett, M.J., UKAEA Report AERE M2936(1976).
- Catlow, C.R.A., Thomas, J.M., Parker, S.C. & Jefferson, D.A., *Nature* **295**, 658(1982).

- Clark Jr., S.P. ed. *Handbook of Physical Constants (revised ed.)*, The Geophysical Society of America, Memoir **97**(1966), p.91.
- Cochran, W., *Advan. Phys.* **10**, 401(1961).
- Cohen, M.L., commentary in *Nature* **338**, 291(1989).
- Dolino, G., in *Structural and Magnetic Phase Transitions in Minerals* (ed. Ghose, S., Coey, J.M.D. & Salje, E.) *Advances in Physical Geochemistry* vol.7 (Springer-Verlag, New York, 1988) p.17.
- Dorner, B., Grimm, H. & Rzany, H., *J. Phys. C: Solid St. Phys.* **13**, 6607(1980).
- Dunning Jr., T.T. & Hay, P.J., in *Methods of Electronic Structure Theory* (ed. Schaefer III, H.F.), *Modern Theoretical Chemistry* vol.3 (Plenum, New York, 1977) p.1.
- Erikson, R.L. & Hostetler, C.J., *Geochim. Cosmochim. Acta* **51**, 1209(1987).
- Evans, D.J., *J. Chem. Phys.* **78**, 3297(1983).
- Fujino, K., Sasaki, S., Takeuchi, Y. & Sadanaga, R., *Acta Crystallogr.* **B37**, 513(1981).
- Gaskell, P.H. & Tarrant, I.D., *Phil. Mag.* **B42**, 265(1980).
- Gibbs, G.V., *American Mineralogist*, **67**, 421(1982).
- Gilbert, T.J., *J. Chem. Phys.* **49**, 2640(1968).
- Gordon, R.G. & Kim, Y.S., *J. Chem. Phys.* **56**, 3122(1972).
- Gouhara, K., Li, Y.H. & Kato, N., *J. Phys. Soc. Japan* **52**, 3821(1983).
- Graham, E.K. & Barsch, G.R., *J. Geophys. Res.* **74**, 5949(1969).
- Grimm, H. & Dorner, B., *J. Phys. Chem. Solids* **36**, 407(1975).
- Hemley, R.J., in *High Pressure Research in Mineral Physics* (eds. Manghnani, M.H. & Shyno, Y.), *Geophysical Monograph* vol.39 (American Geophysical Union, Washington D.C., 1987) p.347.
- Hemley, R.J., Dickson, M.D. & Gordon, R.G., *Phys. Chem. Minerals* **14**, 2(1987).
- Hemley, R.J., Jephcoat, A.D., Mao, H.K., Ming, L.C. & Manghnani, M.H., *Nature* **334**, 52(1988).
- Holm, J.L., Kleppa, D.J. & Westrum, E.f., Jr., *Geochim. Cosmochim. Acta*, **31**, 2289(1967).

- Holmquist, S.B., J. Am. Ceram. Soc. **44**(2), 85(1961).
- Hoover, W.G., Phys. Rev. **A31**, 1695(1985).
- Hoover, W.G., Ladd, A.J.C. & Moran, B., Phys. Rev. Lett. **48**, 1818(1982).
- Horiuchi, H., Hirano, M., Ito, E. and Matsui, Y., Am. Mineral. **67**, 788(1982).
- Horiuchi, H., Ito, E. & Weidner, D.J., Am. Mineral. **72**, 357(1986).
- Huzinaga, S., Andzelm, J., Ktobukowski, M., Radzio-Andzelm, E., Sakai, Y. & Tatewaki, H., in *Gaussian Basis Sets for Molecular Calculation* (eds. Huzinaga et al.), Physical Science Data vol.16 (Elsevier, Amsterdam, 1984).
- Ida, Y., Phys. Earth. Planet. Inter. **13**, 97(1976).
- Ida, Y. and Mizutani, H. , in *Material Science of the Earth I – The World of High Pressure and High Temperature –*, Chapter 1 (eds. S. Akimoto and H. Mizutani), Iwanami: Earth Science 2 (Iwanami, Japan, 1978), in Japanese.
- Jackson. M.D., Ph.D. dissertation, 258pp., Harvard University, 1986.
- Kato, K. & Nukui, A., Acta Crystallogr. **B32**, 2486(1976).
- Kerr, W.C. & Bishop, A.R., Phys. Rev. **B34**, 6295(1986).
- Kumazawa, M. & Anderson, O.L., J. Geophys. Res. **74**, 5961(1969).
- Kushiro, I., J. Geophys. Res. **81**, 6347(1976).
- Kushiro, I., in *Physics of Magmatic Processes* (ed. Hargraves, R.B.) (Princeton Univ. Press, 1980) p.93.
- Kushiro, I., Carnegie Inst. Washington, Year Book **80**.
- Ladd, A.J.C. & Hoover, W.G., Phys. Rev. **B28**, 1756(1983).
- Lasaga, A.C. & Gibbs, G.V., Phys. Chem. Minerals **14**, 107(1987).
- Levien, L., Prewitt, C.T. & Weidner, D.J., Am. Mineral. **65**, 920(1980).
- Matsui, M., Akaogi, M. & Matsumoto, T., Phys. Chem. Minerals **14**, 101(1987).
- Matsui, M. & Bussing, W.R., Phys. Chem. Minerals **11**, 55(1984).
- Matsui, Y., in *Material Science of the Earth III – Geochemistry of Rocks and Minerals –*, Chapter 1 (eds. Y. Matsui and S. Banno), Iwanami: Earth Science 4 (Iwanami, Japan, 1979), in Japanese.

- Matsui, Y. & Kawamura, K., *Nature* **285**, 648(1980).
- Matsui, Y. & Kawamura, K., in *Materials Science of the Earth's Interior* (ed. I. Suganawa) (Terra Scientific Publication Company, Tokyo, 1984), p.3.
- Matsui, Y. & Kawamura, K., in *High Pressure Research in Mineral Physics* (eds. Manghnani, M.H. & Shyno, Y.), Geophysical Monograph vol.39 (American Geophysical Union, Washington D.C., 1987) p.305.
- Matsui, Y., Kawamura, K. & Syono, Y., in *High pressure Research in Geophysics* (eds. S. Akimoto & M.H. Manghnani) (Center for academic publications Japan/Reidel, Tokyo/Dordrecht, 1982), p.511.
- Matsui, Y. & Matsui, M., in *Structural and Magnetic Phase Transitions in Minerals* (eds. Ghose, S., Coey, J.M.D. & Salje, E.) Advances in Physical Geochemistry vol.7 (Springer-Verlag, New York, 1988) p.129.
- McLean, A.D. & Chandler, G.S., *J. Chem. Phys.* **72**, 5639(1980).
- Mishima, O., Calvert, L.D. & Whalley, E., *Nature* **310**, 393(1984)
- Miyamoto, M. & Takeda, H., *Geochem. J.* **14**, 243(1980).
- Nakanishi, K., Ikari, K., Okazaki, S. & Touhara, H., *J. Chem. Phys.* **83**, 1223(1985).
- Newton, M.D. & Gibbs, G.V., *Phys. Chem. Minerals* **6**, 221(1980).
- Nosé, S., *J. Chem. Phys.* **81**, 511(1984).
- Nosé, S. & Klein, M.L., *J. Chem. Phys.* **90**, 5005(1989).
- Park, K.T., Terakura, K. & Matsui, Y., *Nature* **336**, 670(1988).
- Parker, S.C., UKAEA Report AERE TP968(1982).
- Parker, S.C., *Solid State Ionics* **8**, 179(1983).
- Parrinello, M. & Rahman, A., *J. Appl. Phys.* **52**, 7182(1980).
- Pauling, L., *J. Am. Chem. Soc.* **51**, 1010(1929).
- Pauling, L., *The Nature of the Chemical Bond*, 3rd ed. (Cornell Univ. Press, Ithaca, New York, 1960).
- Price, G.D. & Parker, S.C., *Phys. Chem. Minerals* **10**, 209(1984).
- Rahman, A., *Phys. Rev.* **A136**, 305(1964).
- Sasaki, S., Prewitt, C.T., Sato, Y. & Ito, E., *J. Geophys. Res.* **87**, 7829(1982).

- Sasaki, S., Takeuchi, Y., Fujino, K. & Akimoto, S., Z. Kristallogr. **158**, 279(1982).
- Schneider, T. & Stoll, T., Phys. Rev. Lett. **31**, 1254(1973).
- Schneider, T. & Stoll, T., Phys. Rev. **B10**, 2004(1974).
- Schneider, T. & Stoll, T., Phys. Rev. **B13**, 1216(1976).
- Schneider, T. & Stoll, T., Phys. Rev. **B17**, 1302(1978).
- Soules, T., J. Noncrystal. Solid **49**, 29(1982).
- Soules, T. & Busbey, R., J. Chem. Phys. **75**, 969(1981).
- Stillinger, F.H. & Weber, T.A., Phys. Rev. **B31**, 5262(1985).
- Stixrude, L. & Bukowinski, M.S.T., Phys. Chem. Minerals **16**, 199(1988).
- Stolper, E.M. & Ahrens, T.J., Geophys. Res. Lett. **14**, 1231(1987).
- Tendeloo, G. van, Landuyt, J. van & Amelinckx, S., Phys. Status Solidi **A33**, 723(1976).
- Tosi, M.P., Solid State Physics **16**, 1(1964).
- Tosi, M.P. & Cohen, M.L., Phys. Rev. Lett. **45**, 1004(1980).
- Tsuchida, Y. & Yagi, T., Tech. Rep. of ISSP, University of Tokyo, Ser.A No. 2099(1989).
- Tsuchida, Y. & Yagi, T., Nature **340**, 217(1989).
- Tsuneyuki, S., Matsui, Y., Aoki, H., & Tsukada, M., Nature **339**, 209(1989).
- Tsuneyuki, S., Tsukada, M., Aoki, H. and Matsui, Y., Phys. Rev. Lett. **61**, 869(1988).
- Tsuneyuki, S., Tsukada, M., Aoki, H. and Matsui, Y., in *Dynamical Processes of Material Transport and Transformation in the Earth's Interior* (F. Marumo ed.) (Terra Scientific Publishing Co., Tokyo) in press.
- Verlet, I., Phys. Rev. **159**, 98(1967).
- Wall, A. & Price, G.D., Am. Mineral. **73**, 224(1988).
- Weidner, D.J. & Ito, E., Phys. Earth. Planet. Inter. **40**, 65(1985).
- Weidner, D.J., Sawamoto, H., Sasaki, S. & Kumazawa, M., J. Geophys. Res. **B89**, 7852(1984).
- Williams, Q. & Jeanloz, R., Science **239**, 902(1988).
- Wise, S.S., Margrave, J.L., Feder, H.M. & Hubbard, W.N., Phys. Chem. **66**,

381(1962).

- Wolf, G.H. and Bukowinski, M.S.T., in *High Pressure research in Mineral Physics* (eds. Manghnani, M.H. & Shyno, Y.), Geophysical Monograph vol.39 (American Geophysical Union, Washington D.C., 1987) p.313.
- Woodcock, L.V., Angell, C.A. & Cheeseman, P., J. Chem. Phys. **65**, 1565(1976).
- Wright, A.F. & Lehmann, M.S., J. Sol. Stat. Chem. **36**, 371(1981).
- Yagi, T. & Akimoto, S., Tectonophysics **35**, 259(1976).
- Yagi, T., Mao, H.K. & Bell, P.M., in *Saxena (ed): Advances in Physical Geochemistry vol.2* (Springer-Verlag, New York, 1982) p.317.
- Yin, M.T. & Cohen, M.L., Phys. Rev. Lett. **45**, 1004(1980).
- Yoon, B.J., Morokuma, K. & Davidson, E.R., J. Chem. Phys. **83**, 1223(1985).
- Young, R.A., U.S. Air Force Report No. AFOSR-2569(1962).